



# **Heavy Warm Rolling as a New Processing Concept for Ultra Fine Grained Hot Strip Steels**

**Lydia Storojeva, Dirk Ponge, Dierk Raabe**

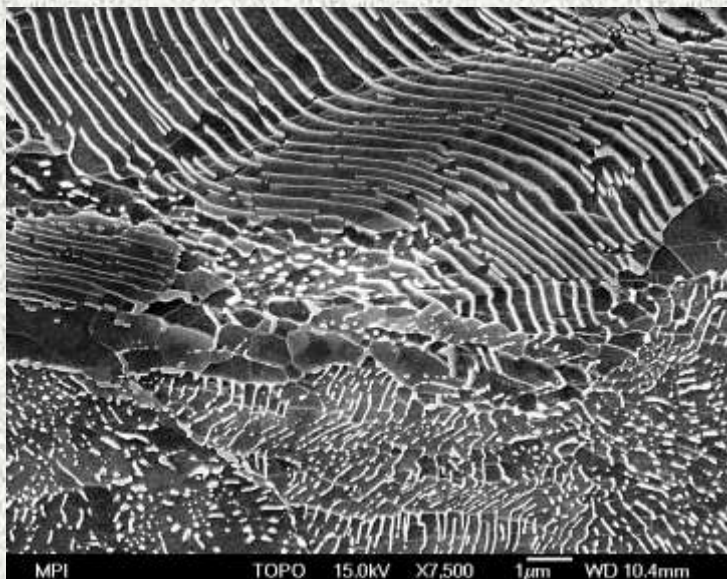


- ✓ **The Main Objectives**
- ✓ **PonyMill Concept**
- ✓ **Material and Experimental Technique**
- ✓ **Austenite Deformation**
- ✓ **Heavy Warm Deformation**
- ✓ **Microstructure Formation**
- ✓ **Summary**



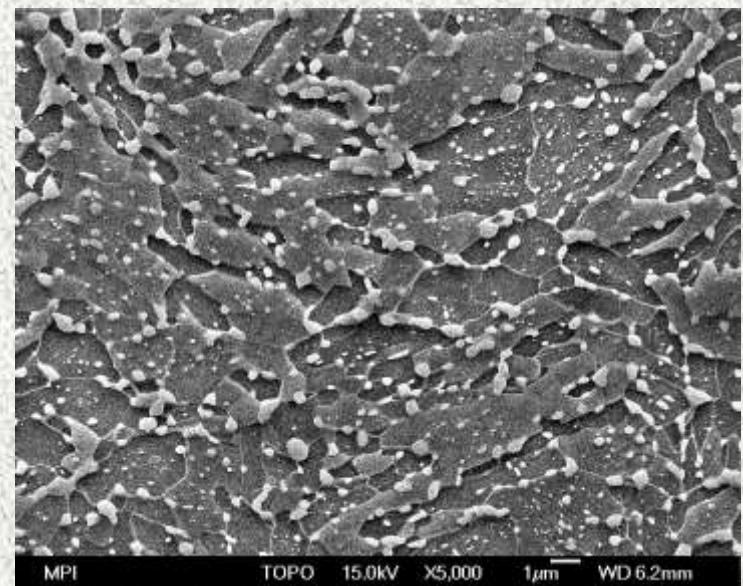
**Processing parameters for the production of thin hot strip of low, medium and high carbon steels (0.15, 0.35 and 0.70% C) with spheroidised cementite by heavy warm rolling**

Lamellar Pearlite



**Low toughness,  
poor cold formability and  
machinability**

Spheroidised Cementite

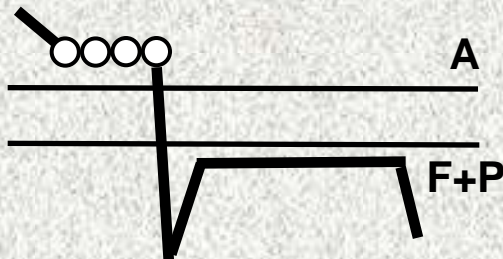


**High toughness,  
good cold formability and  
machinability**

# Spheroidisation Treatments

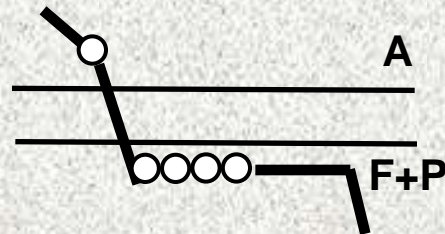


## Quenching & Tempering

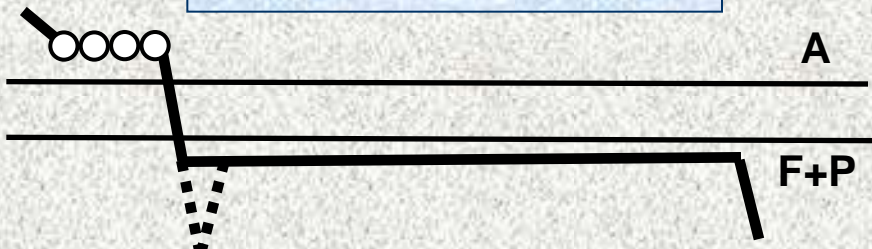


Thin strip can not be produced

## Heavy Warm Rolling



## Annealing Treatment



Throughput up to 2 days

### Advantageous:

The accelerated rate of process (by  $10^4$ )

### Disadvantageous:

The decrease of productivity on conventional hot strip mill

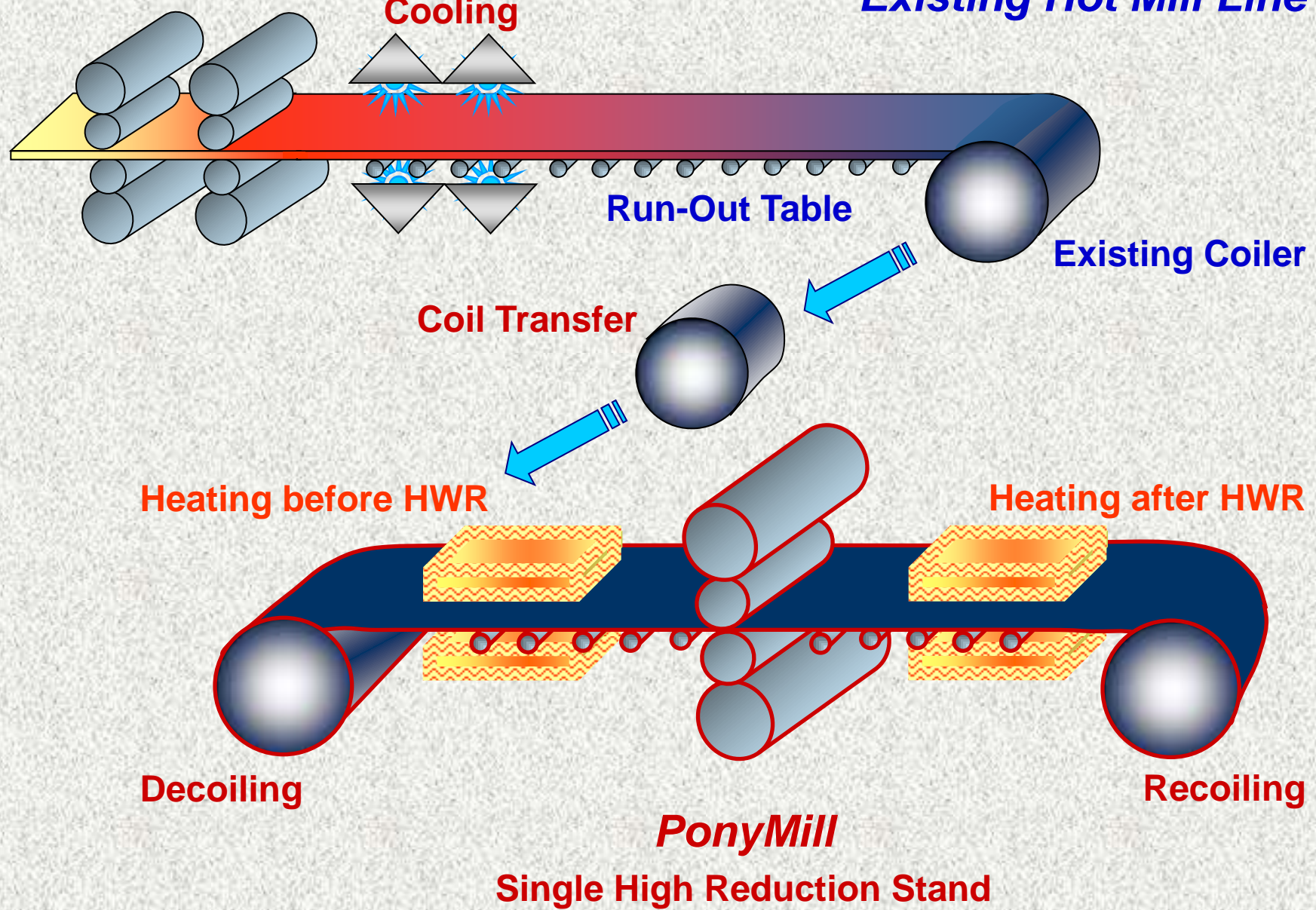


- ✓ The Main Objectives
- ✓ **PonyMill Concept**
- ✓ Material and Experimental Technique
- ✓ Austenite Deformation
- ✓ Heavy Warm Deformation
- ✓ Microstructure Formation
- ✓ Summary

# PonyMill Concept



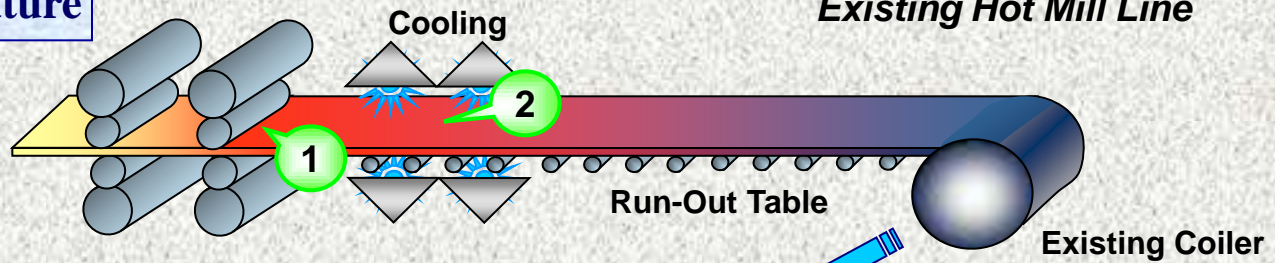
*Existing Hot Mill Line*



# Processing Parameters for Study



1. Austenitic rolling temperature



2. Cooling rate

3. Heating device location

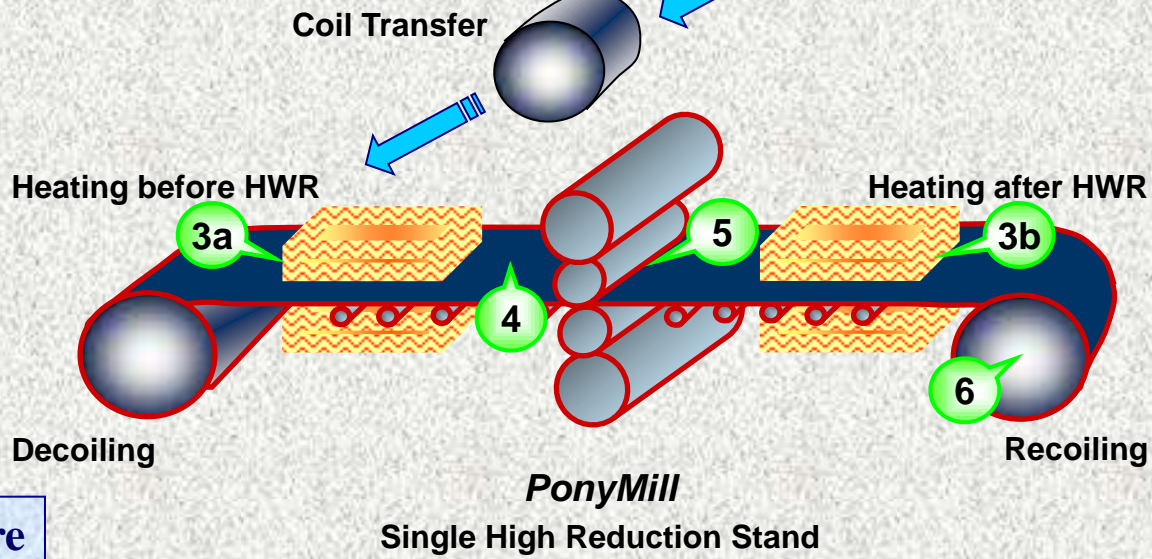
3a. Before HWR

3b. After HWR

4. Heavy Warm Rolling temperature

5. Flow stresses during Heavy Warm Rolling

6. Coiling temperature





- ✓ The Main Objectives
- ✓ PonyMill Concept
- ✓ Material and Experimental Technique
- ✓ Austenite Deformation
- ✓ Heavy Warm Deformation
- ✓ Microstructure Formation
- ✓ Summary



## Chemical Composition, ppm

<i>Steel</i>	<i>C</i>	<i>Si</i>	<i>Mn</i>	<i>P</i>	<i>S</i>	<i>Al</i>	<i>N</i>	<i>Cu</i>	<i>Cr</i>	<i>Ni</i>	<i>Sn</i>	<i>Ti</i>	<i>Nb</i>	<i>V</i>	<i>Mo</i>	<i>B</i>
C15	1440	100	3800	140	60	300	27	130	260	210	111	10	20	10	20	3
C35	3600	2200	5300	110	20	80	67	400	2100	400	50	20	-	-	100	2
C67	6600	2100	7200	#	#	380	47	#	#	#	#	<50	-	<50	-	-

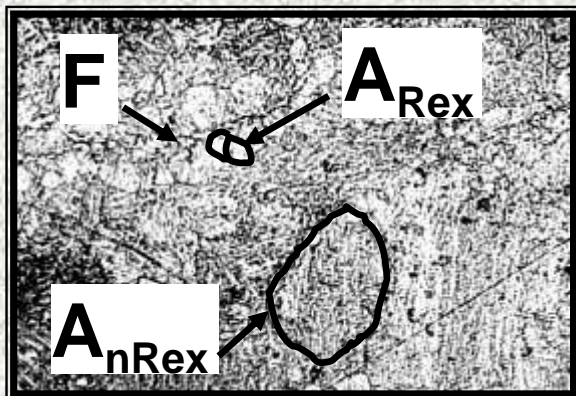
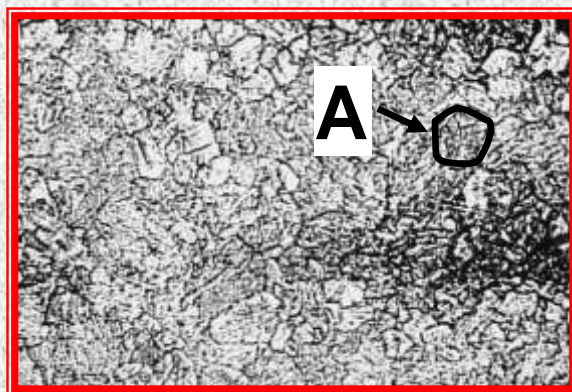
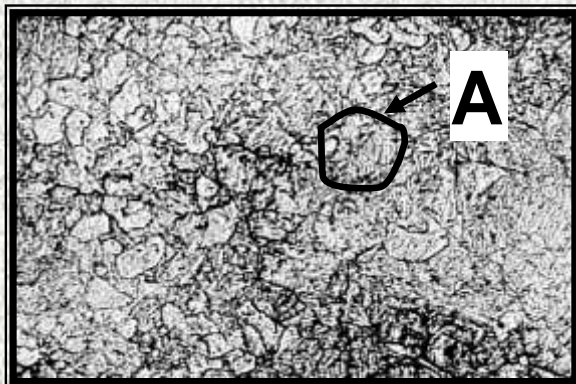
## Experimental Technique

1. WUMSI (the compression of cubic samples  $h_0 \sim 30$  mm,  $h \sim 5$  mm).
2. Dilatometer (CCT diagrams).
3. Light Microscopy (microstructure and microhardness).
4. Scanning Microscopy (pearlite condition – spheroidisation, distribution).
5. EBSD (ferrite condition – softening, grain size, texture, grain boundaries).

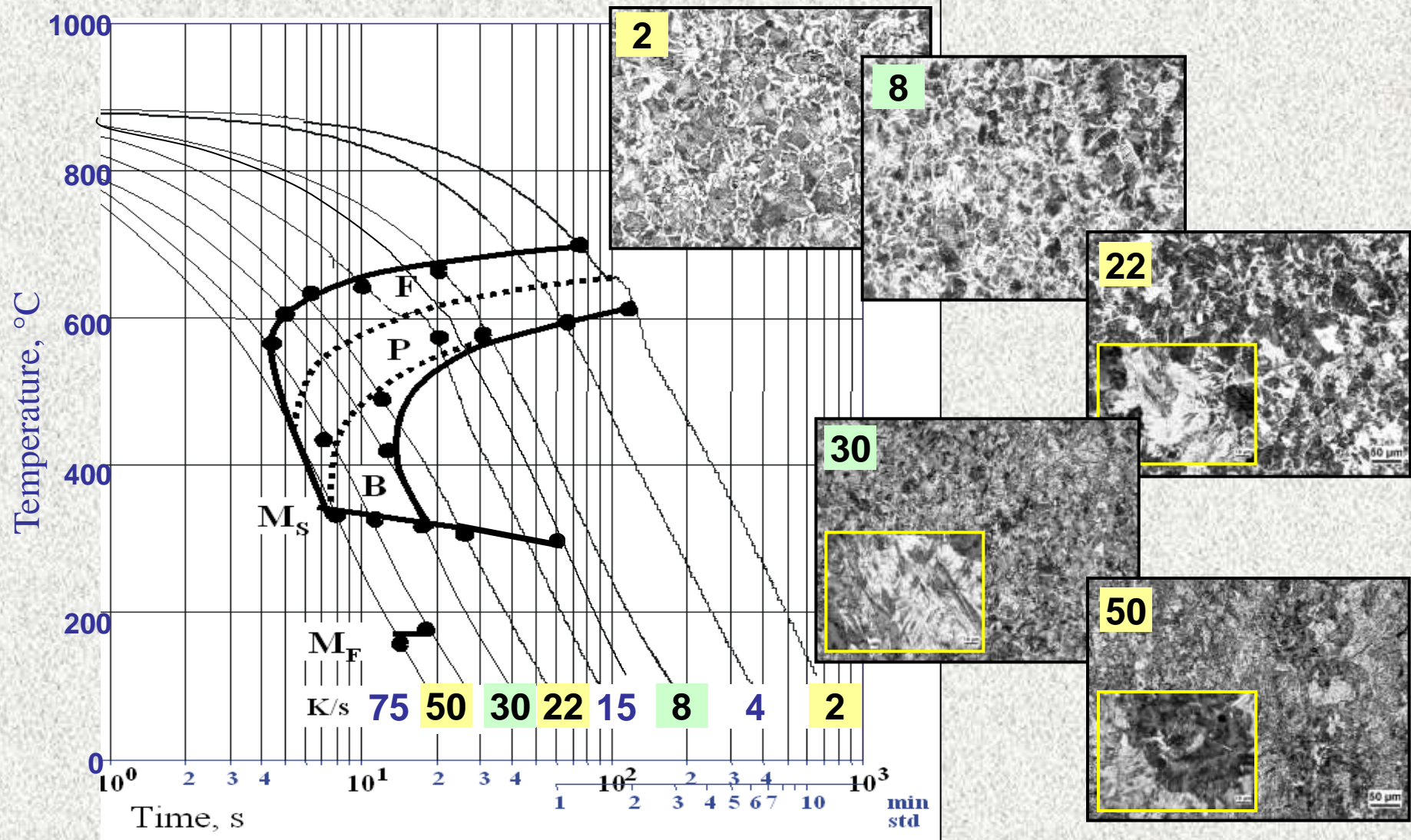


- ✓ The Main Objectives
- ✓ PonyMill Concept
- ✓ Material and Experimental Technique
- ✓ Austenite Deformation
- ✓ Heavy Warm Deformation
- ✓ Microstructure Formation
- ✓ Summary

# Deformation Temperature in Austenite



# CCT Diagram after Deformation in Austenite at 900°C



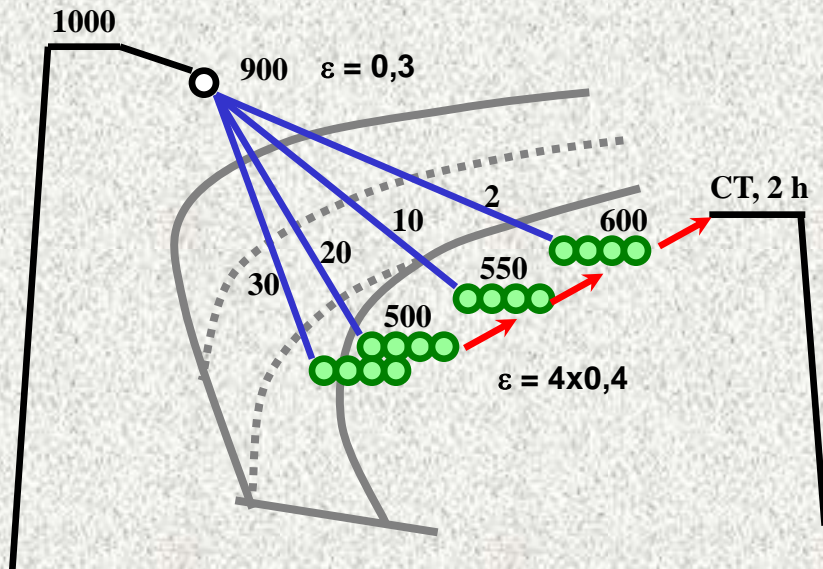


- ✓ The Main Objectives
- ✓ PonyMill Concept
- ✓ Material and Experimental Technique
- ✓ Austenite Deformation
- ✓ Heavy Warm Deformation
- ✓ Microstructure Formation
- ✓ Summary

# Processing Routes

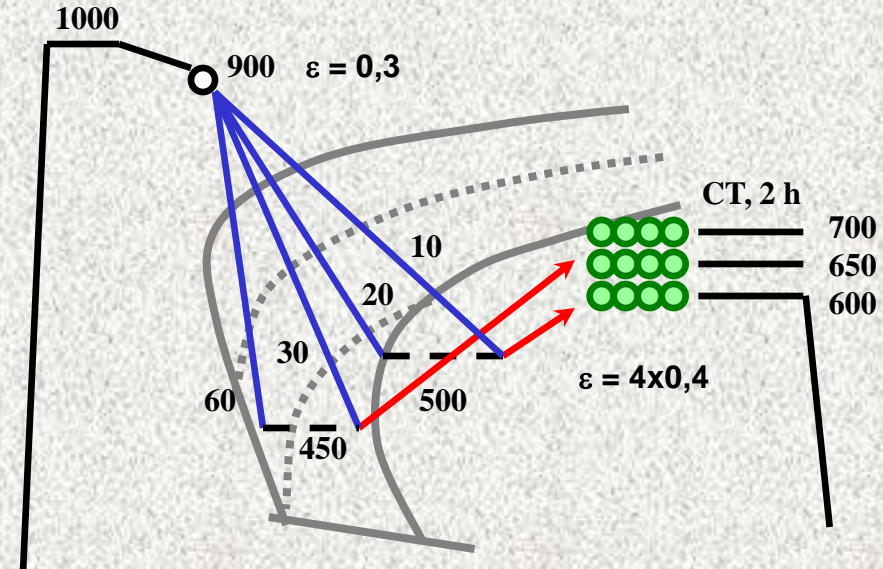


**Route 1**



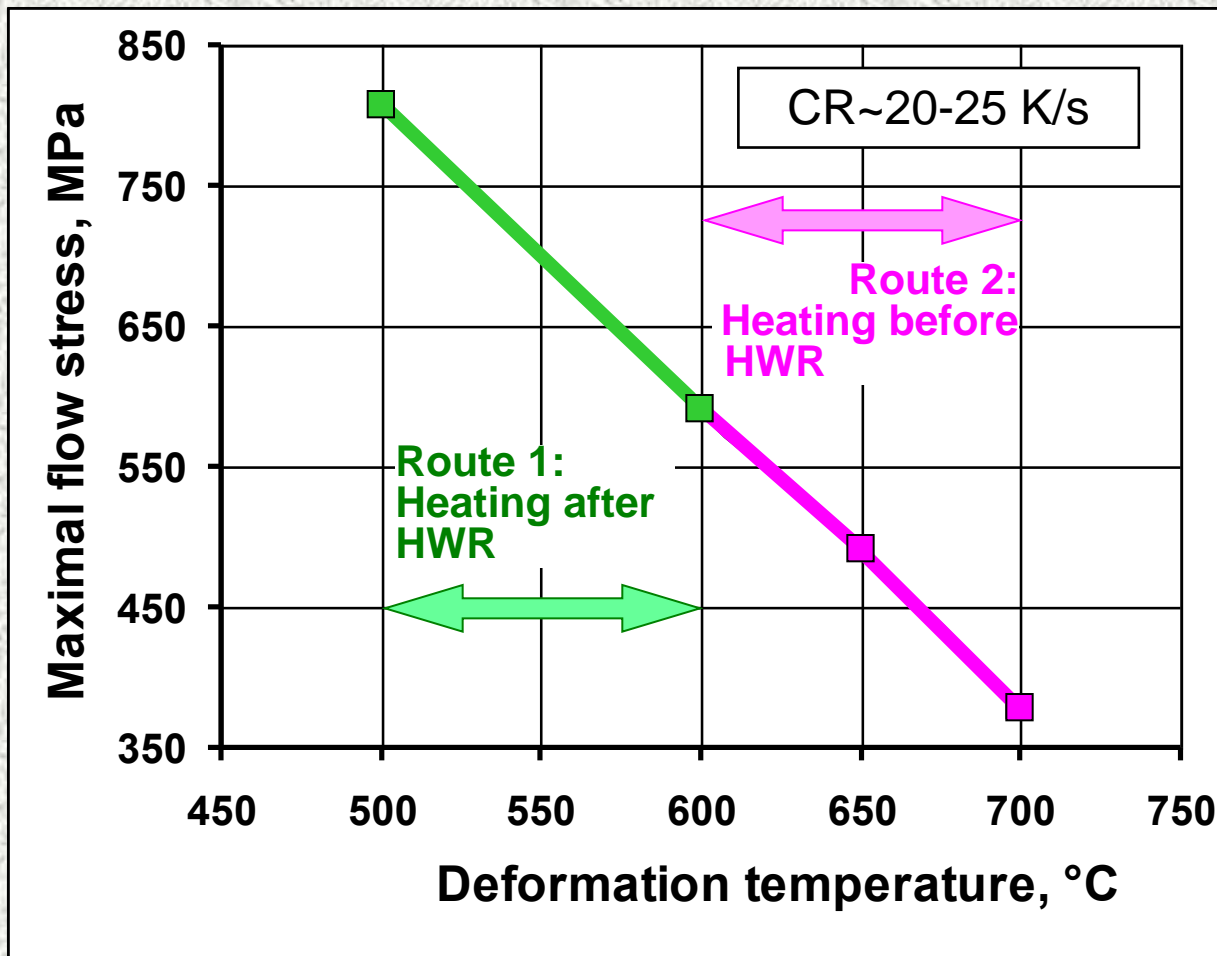
Heating after HWR

**Route 2**



Heating before HWR

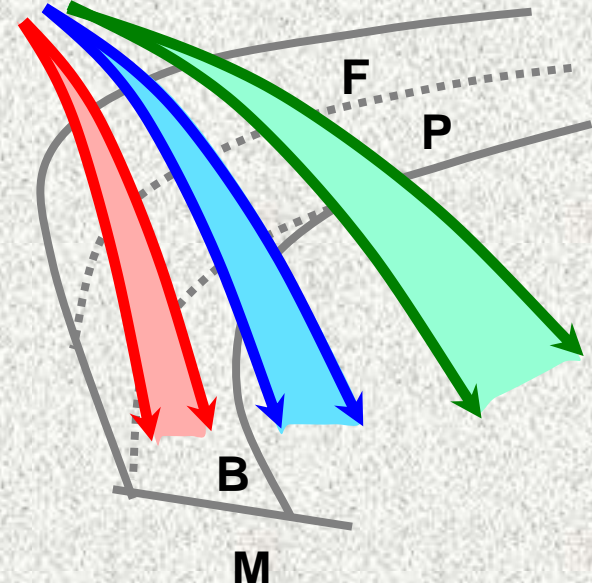
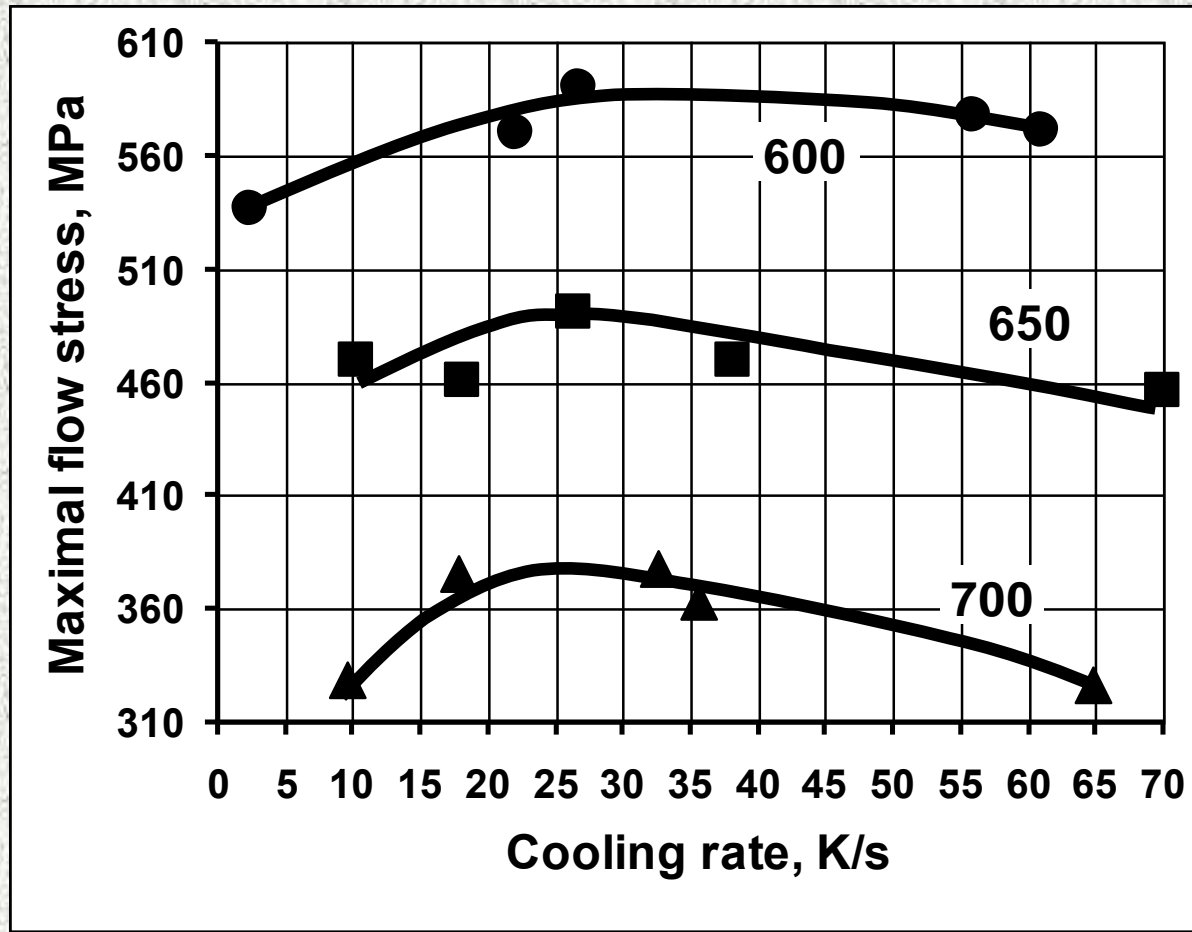
# Flow Stresses during Heavy Warm Deformation



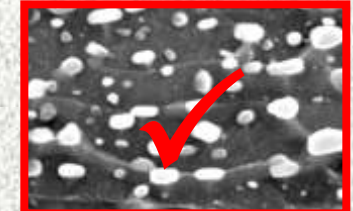
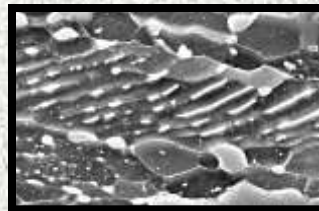
# Flow Stresses during Heavy Warm Deformation



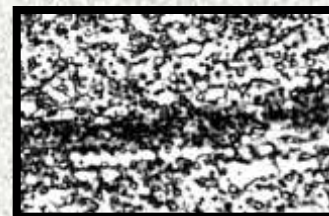
**F+P**      **P+B**      **P+B+A**



**Spheroidisation of Pearlite**



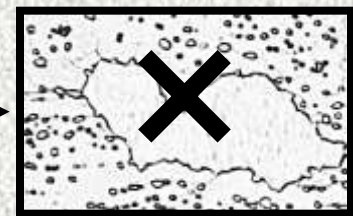
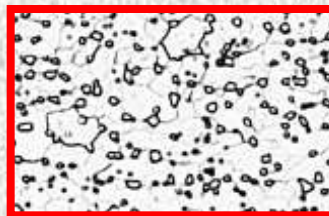
**Distribution of Cementite**



**Softening of Ferrite**



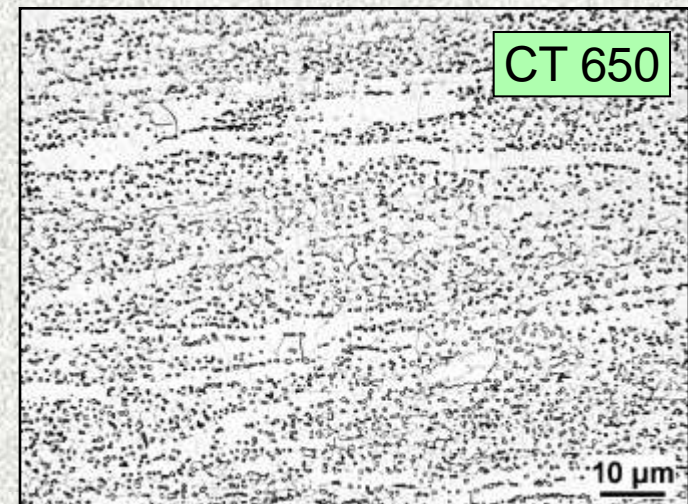
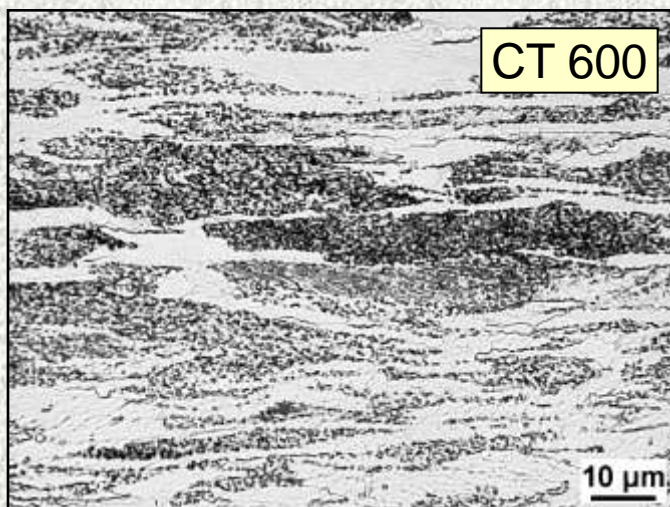
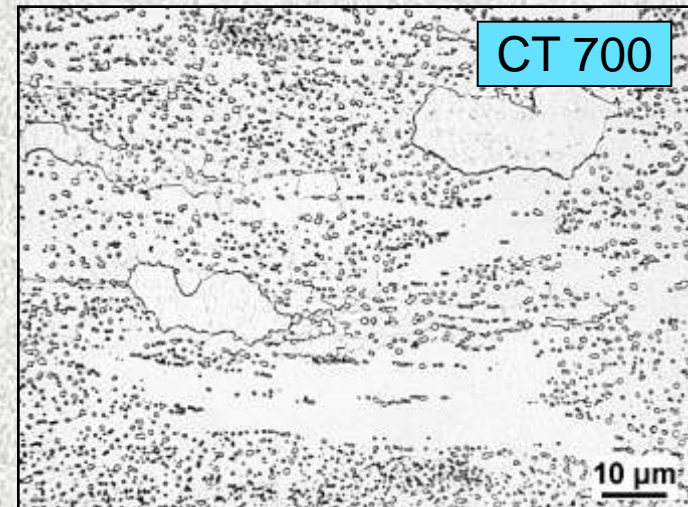
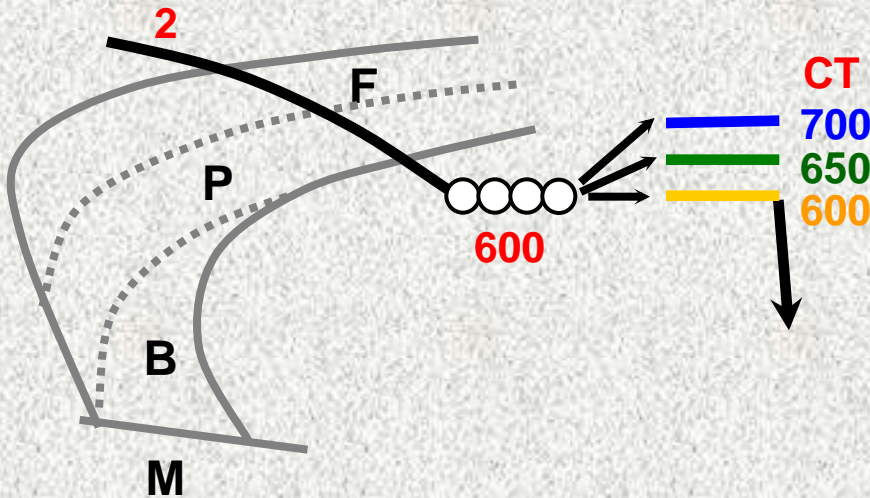
**Coarsening of Ferrite**



# Route 1: Heating after Heavy Warm Rolling



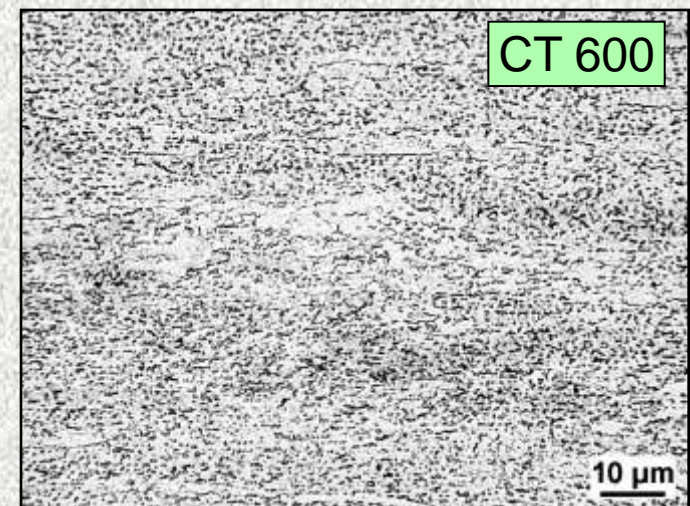
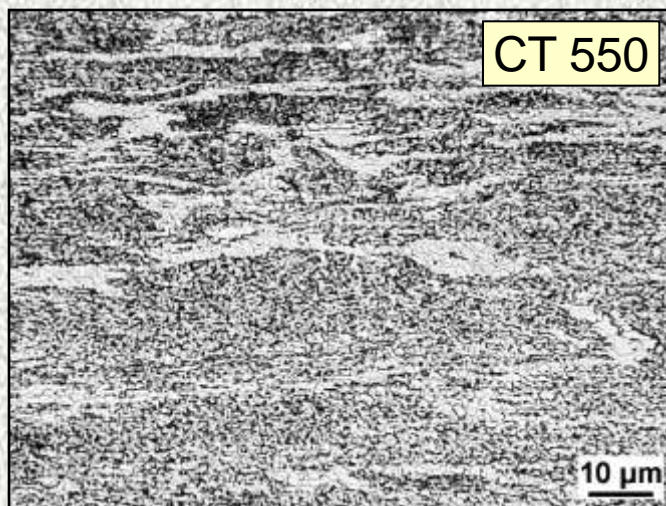
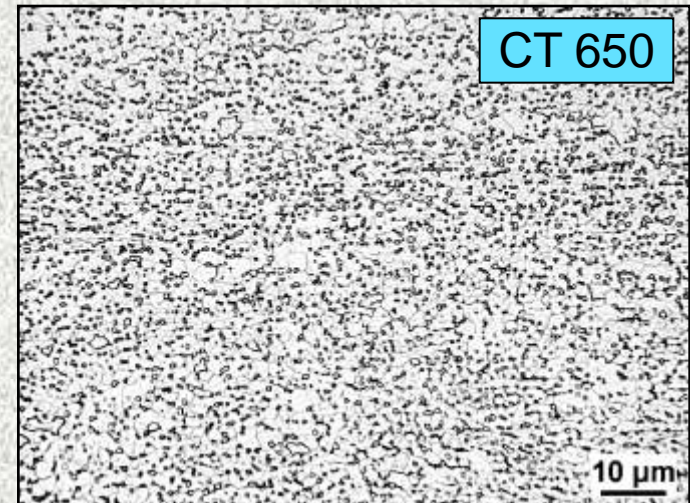
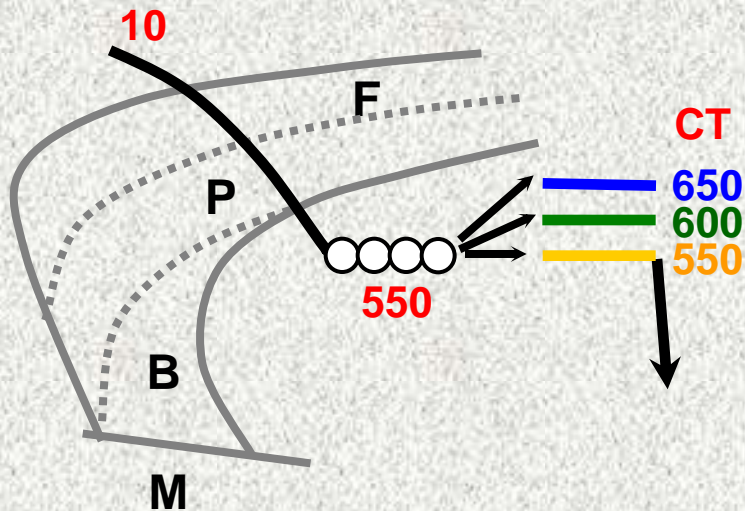
Effect of CT on the Microstructure after CR~2 K/s, TD~600°C



# Route 1: Heating after Heavy Warm Rolling



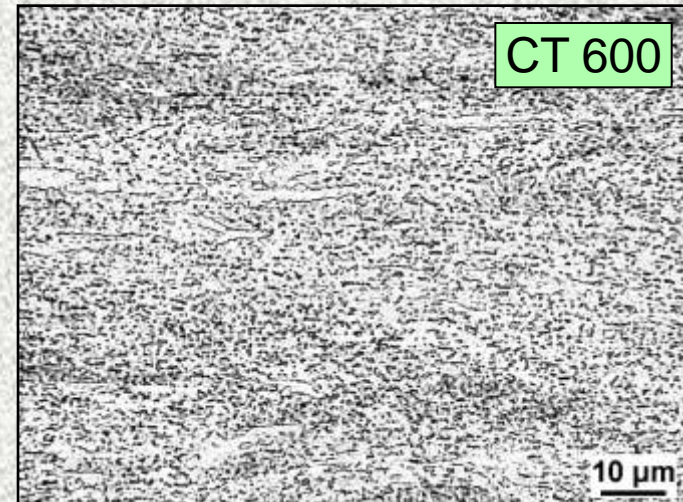
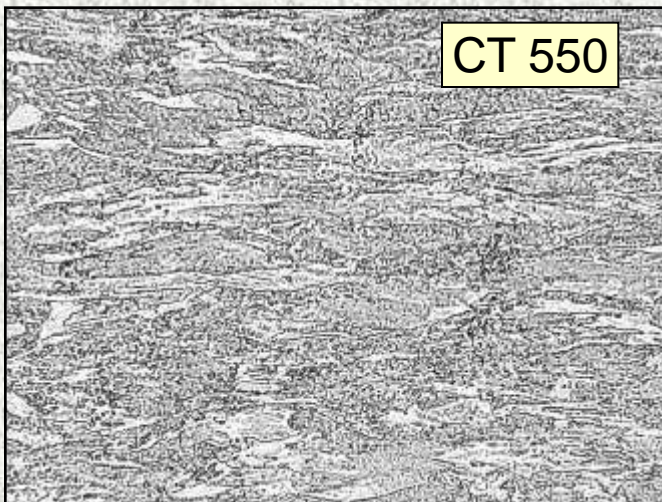
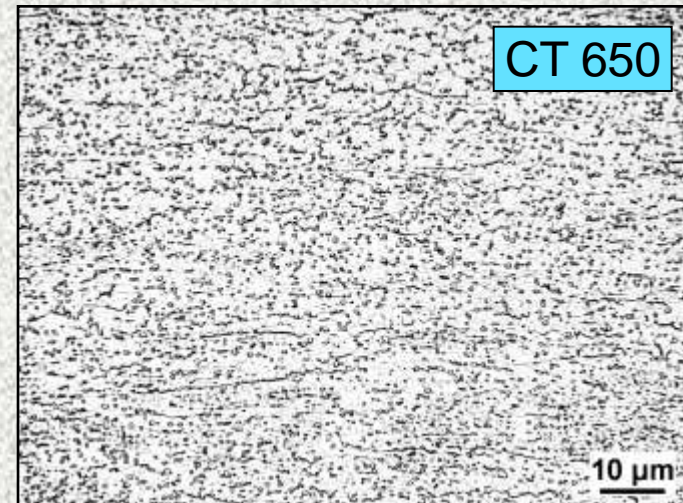
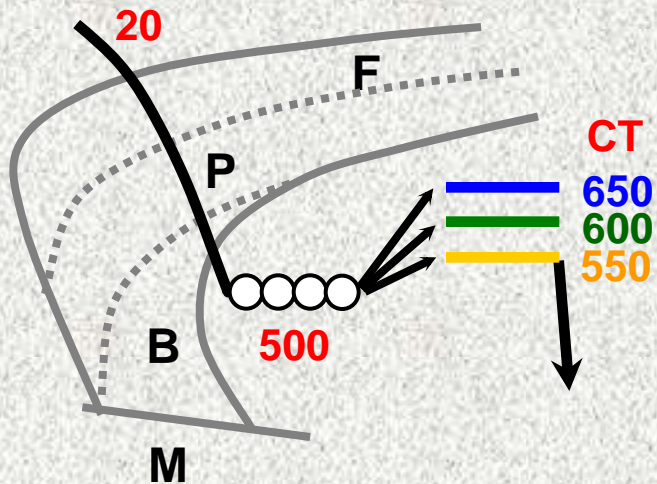
Effect of CT on the Microstructure after CR~10 K/s, TD~550°C



# Route 1: Heating after Heavy Warm Rolling



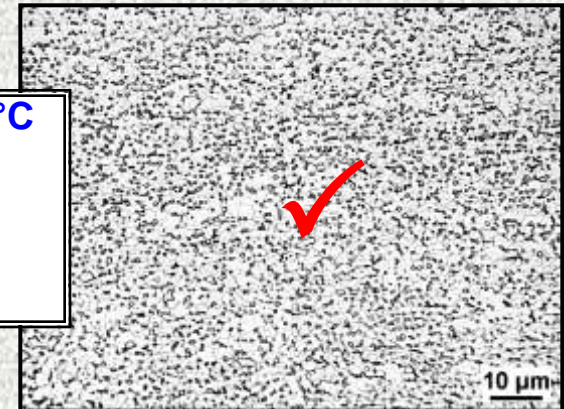
Effect of **CT** on the Microstructure after **CR~20 K/s, TD~500°C**



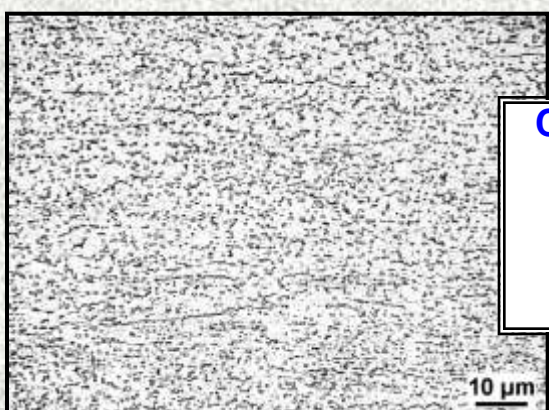
# Treatment Optimisation for Route 1



**CR~2 K/s, TD~600°C, CT~650°C**  
**Spheroidisation – OK**  
**Distribution – inhomogeneous**  
**Softening – OK**  
**Coarsening - no**

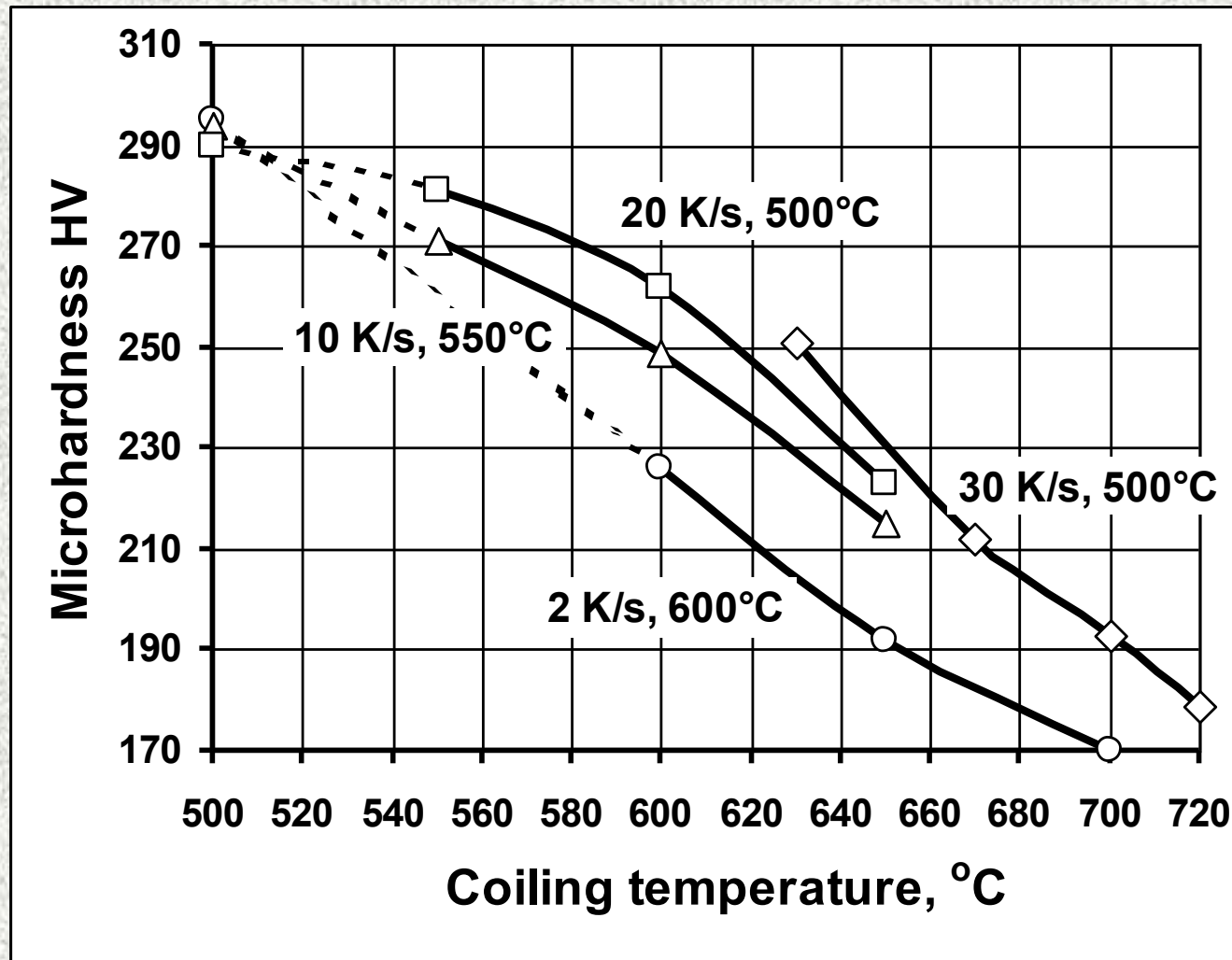


**CR~10 K/s, TD~550°C, CT~650°C**  
**Spheroidisation – OK**  
**Distribution – OK**  
**Softening – OK**  
**Coarsening - no**



**CR~20 K/s, TD~500°C, CT~650°C**  
**Spheroidisation – OK**  
**Distribution – OK**  
**Softening – insufficient**  
**Coarsening - no**

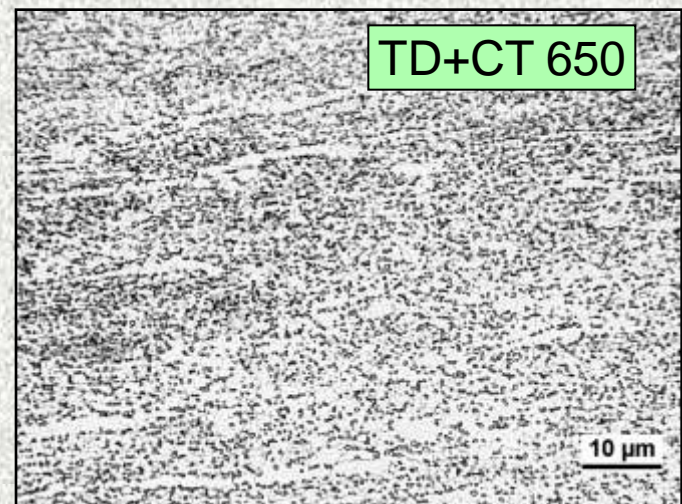
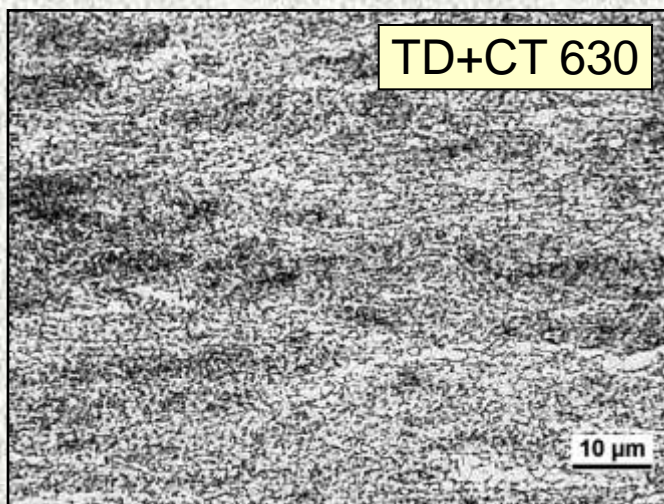
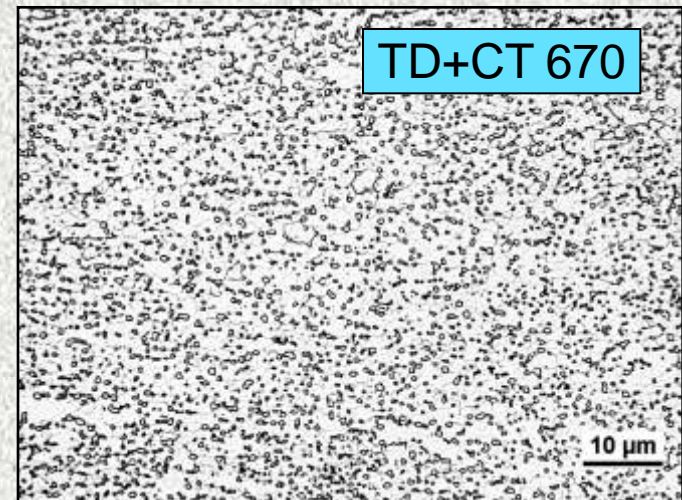
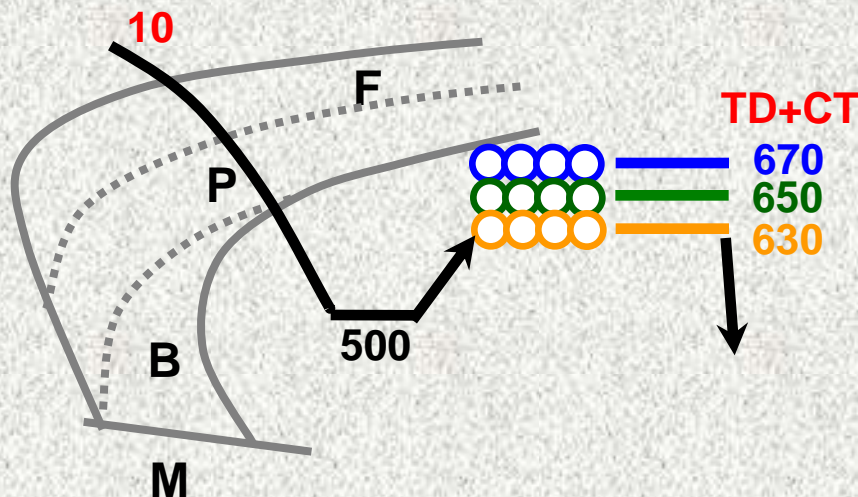
# Microhardness after Route 1



# Route 2: Heating before Heavy Warm Rolling



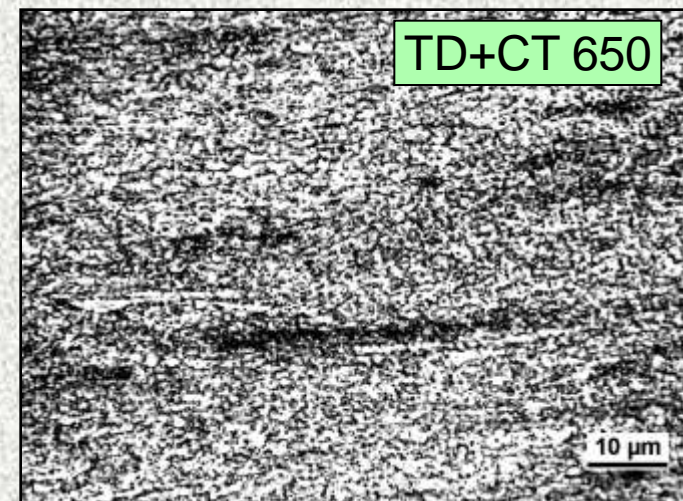
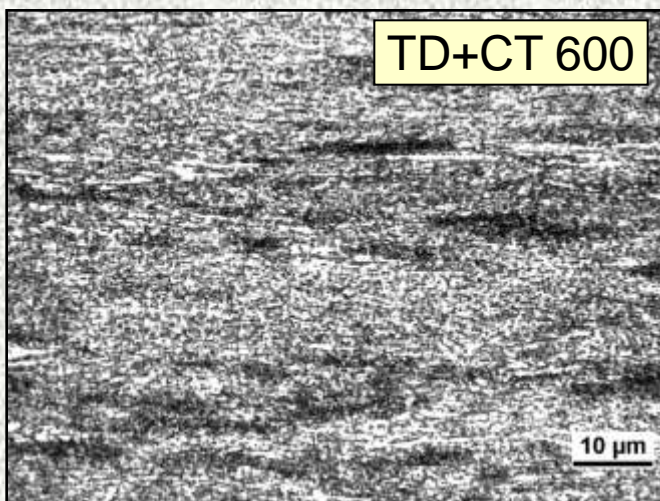
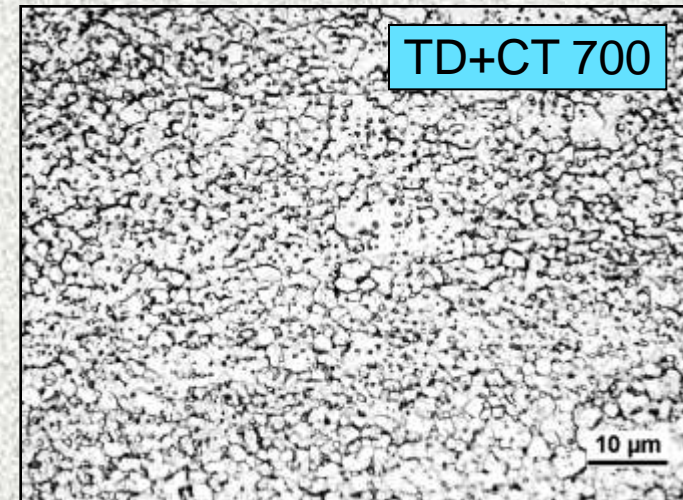
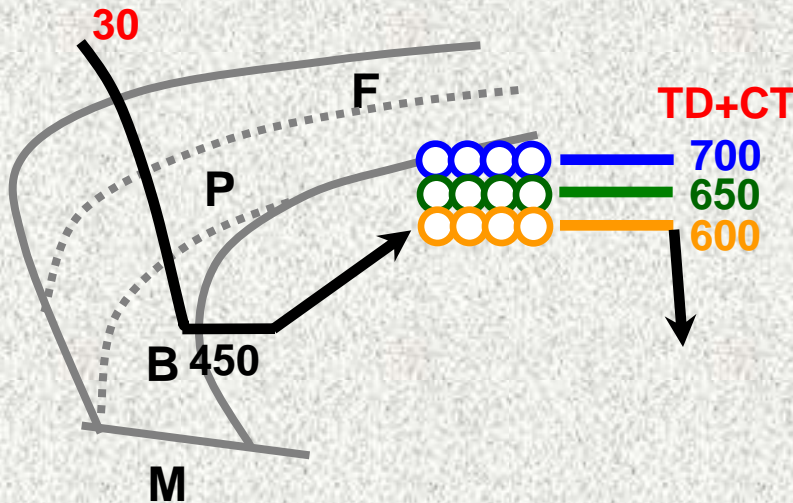
Effect of TD+CT on the Microstructure after CR~10 K/s



# Route 2: Heating before Heavy Warm Rolling



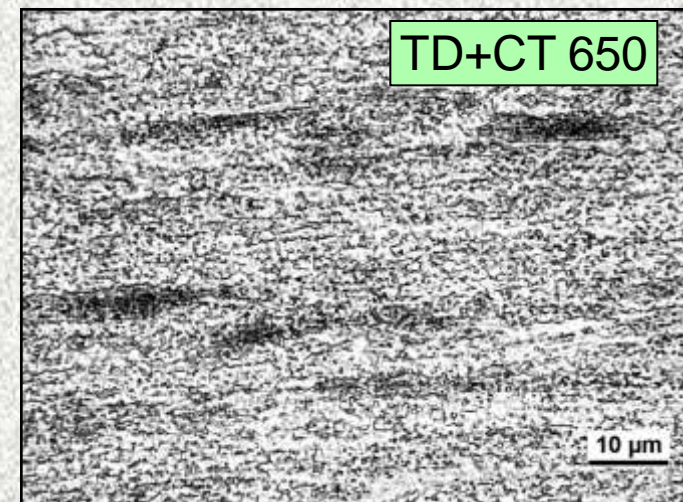
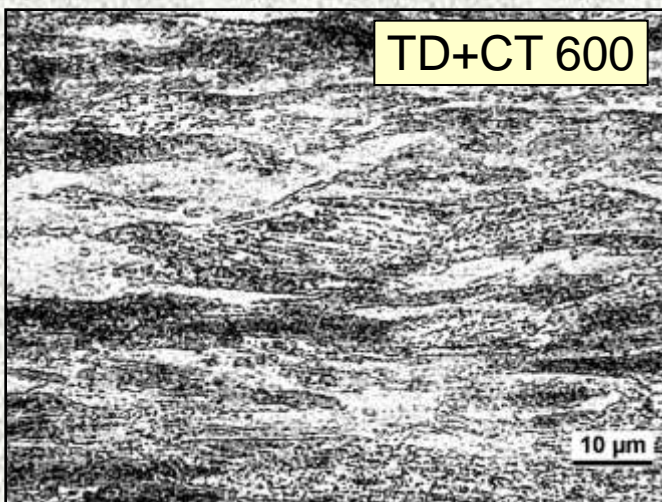
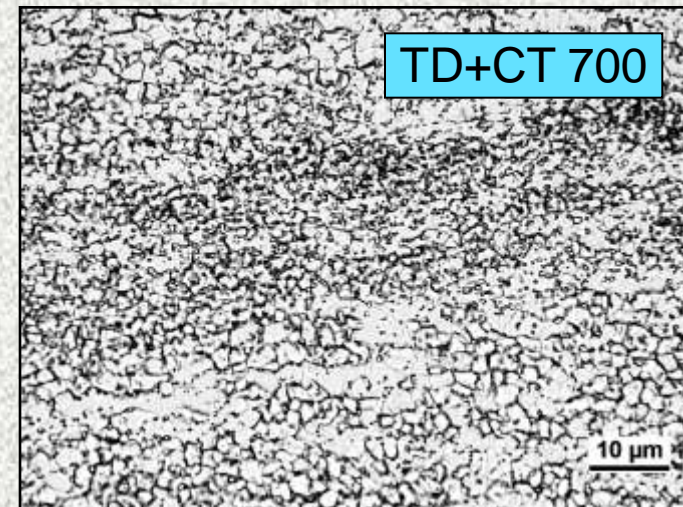
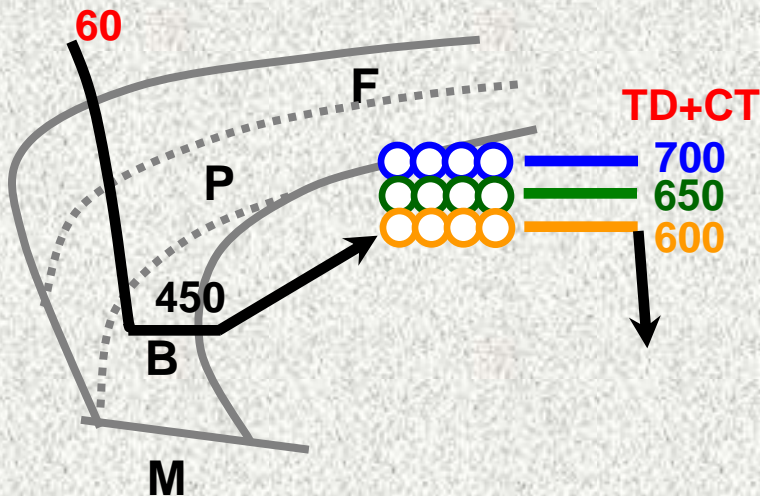
Effect of TD+CT on the Microstructure after CR~30 K/s



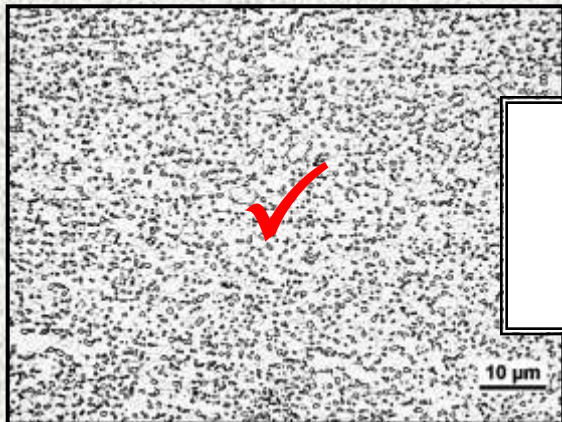
# Route 2: Heating before Heavy Warm Rolling



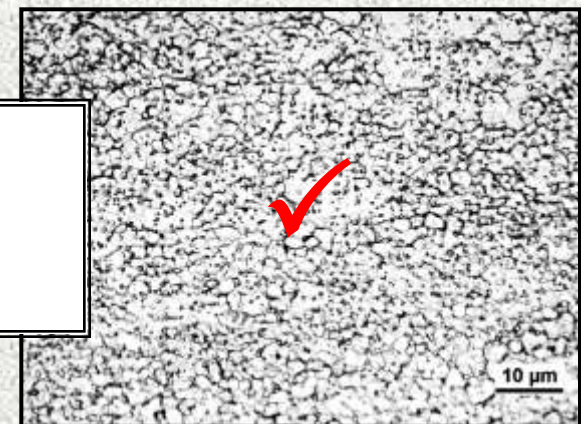
Effect of TD+CT on the Microstructure after CR~60 K/s



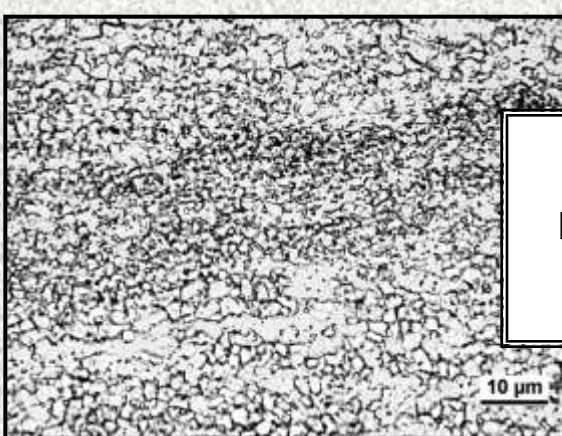
# Treatment Optimisation for Route 2



**CR~10 K/s, TD+CT~670°C**  
Spheroidisation – OK  
Distribution – OK  
Softening – OK  
Coarsening - no

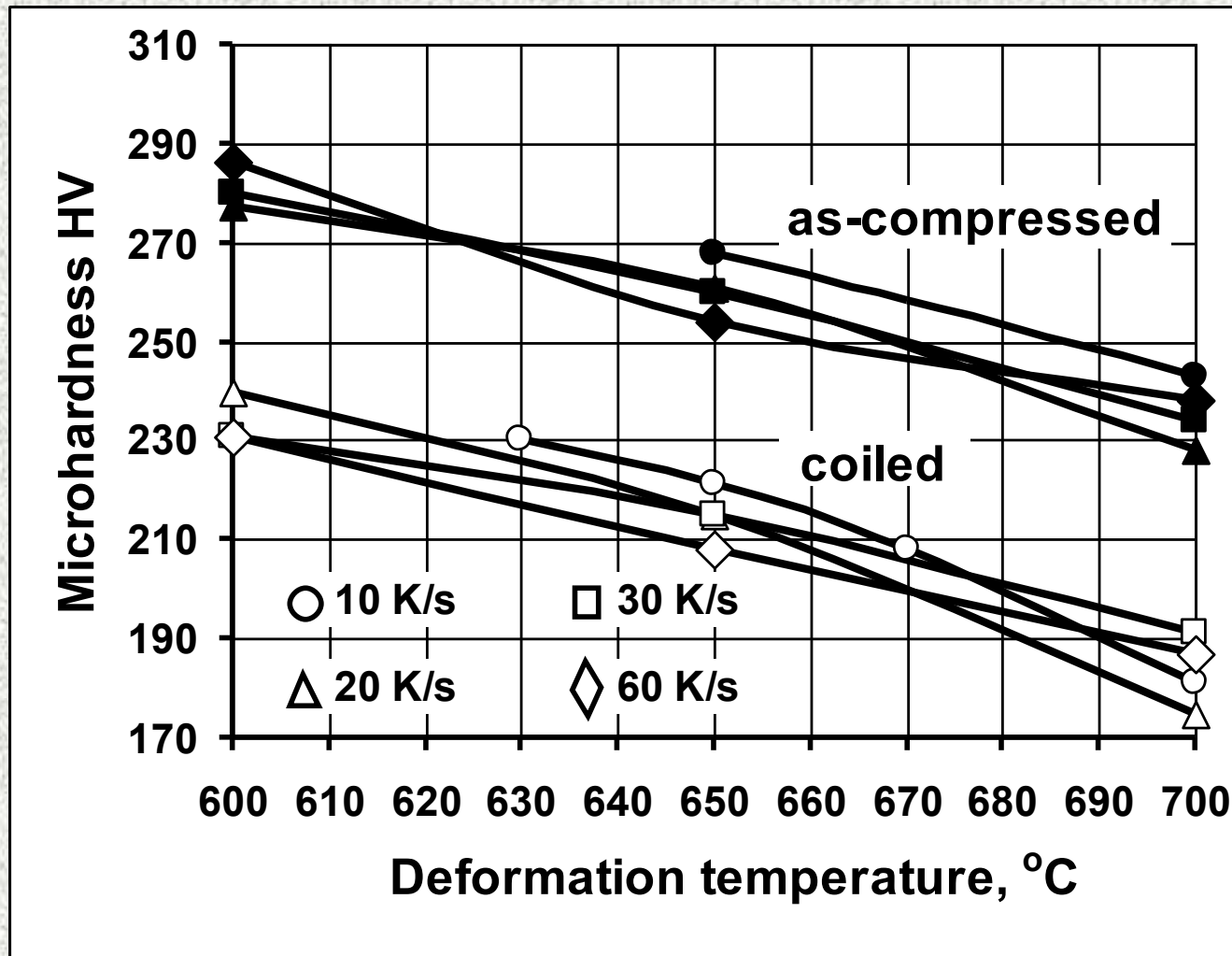


**CR~30 K/s, TD+CT~700°C**  
Spheroidisation – OK  
Distribution – OK  
Softening – OK  
Coarsening - no



**CR~60 K/s, TD+CT~700°C**  
Spheroidisation – OK  
Distribution – inhomogeneous  
Softening – insufficient  
Coarsening - no

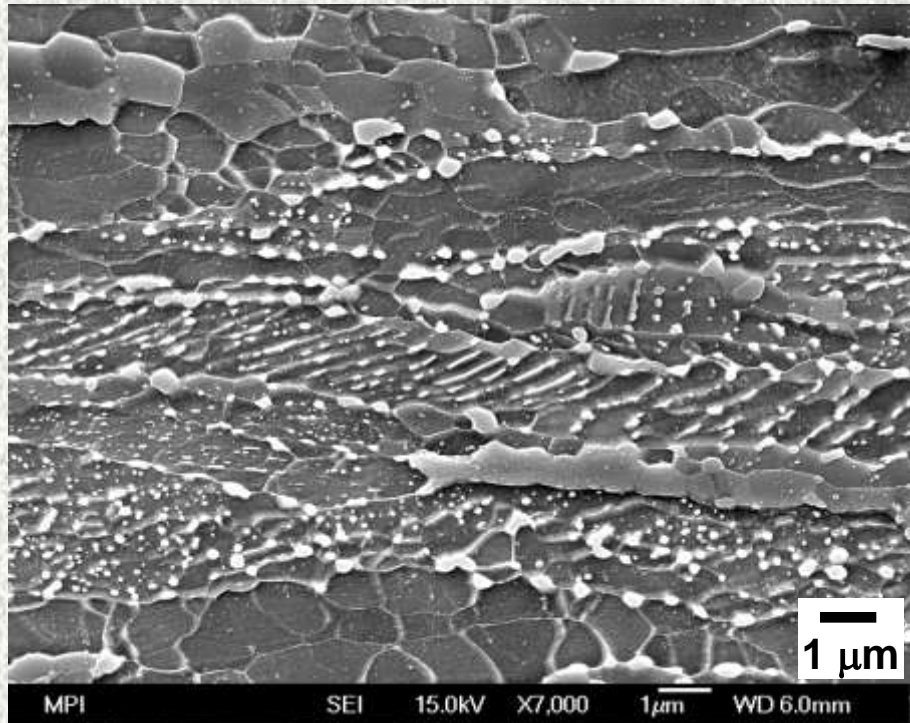
# Microhardness after Route 2



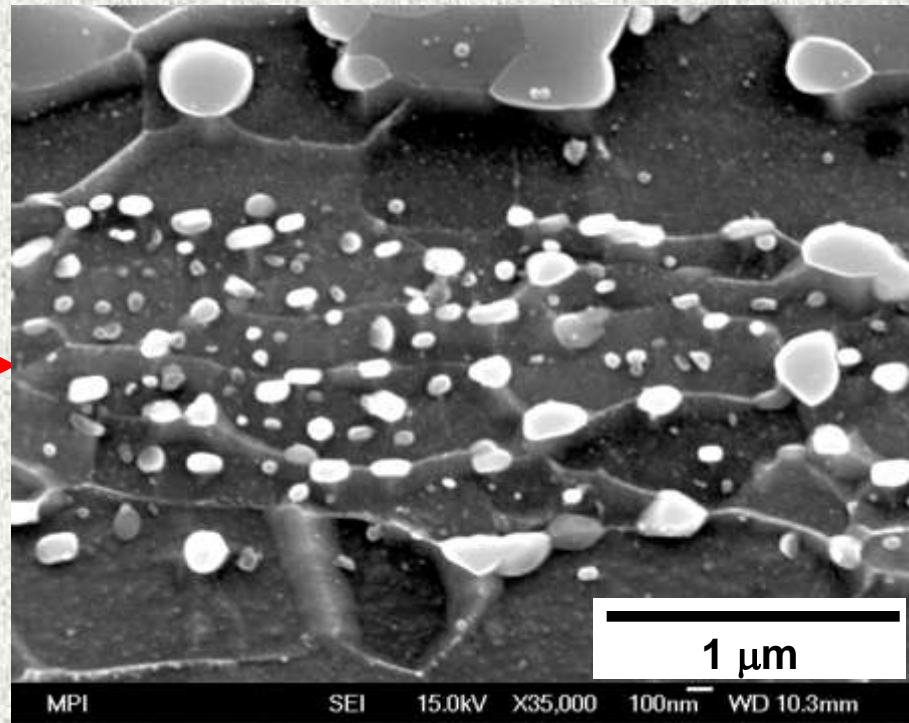


- ✓ The Main Objectives
- ✓ PonyMill Concept
- ✓ Material and Experimental Technique
- ✓ Austenite Deformation
- ✓ Heavy Warm Deformation
- ✓ Microstructure Formation
- ✓ Summary

# Spheroidisation of Pearlite

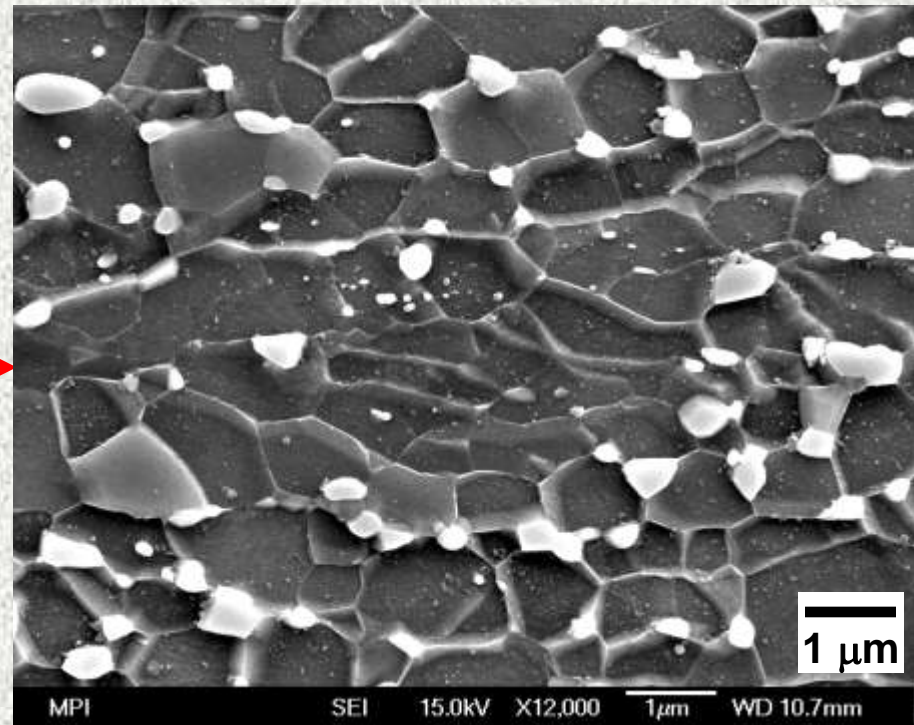
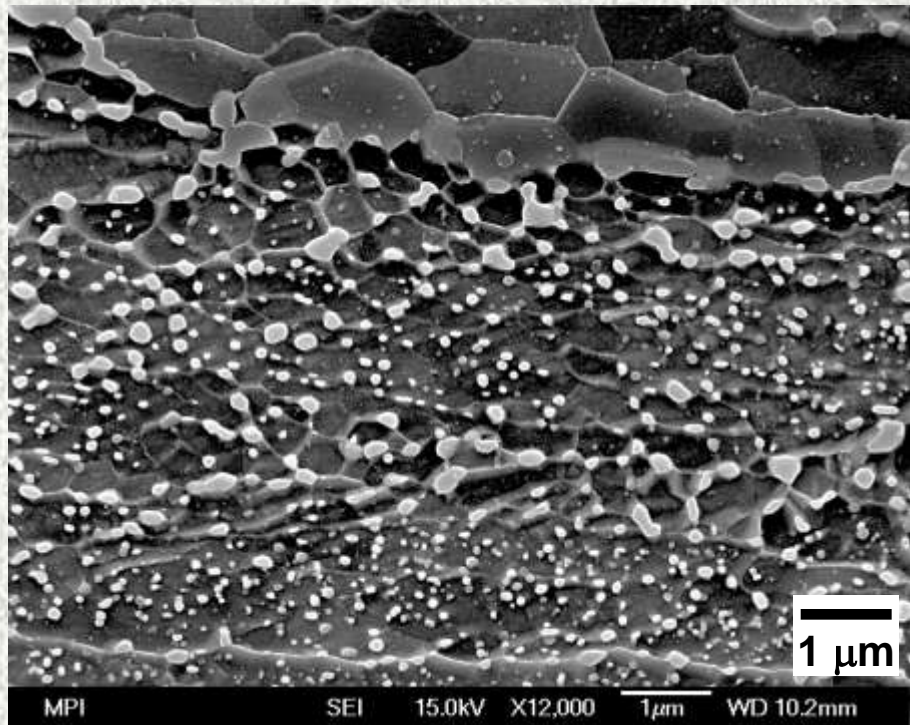


**Begin**  
**CR 2 K/s, TD 600°C, CT 600°C**



**End**  
**CR 2 K/s, TD 600°C, CT 650°C**

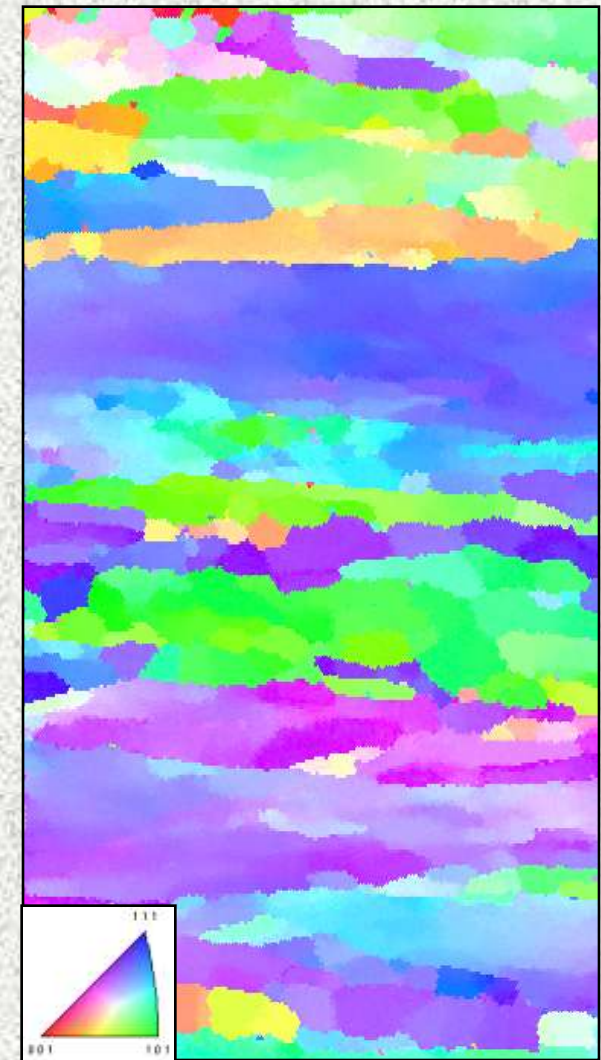
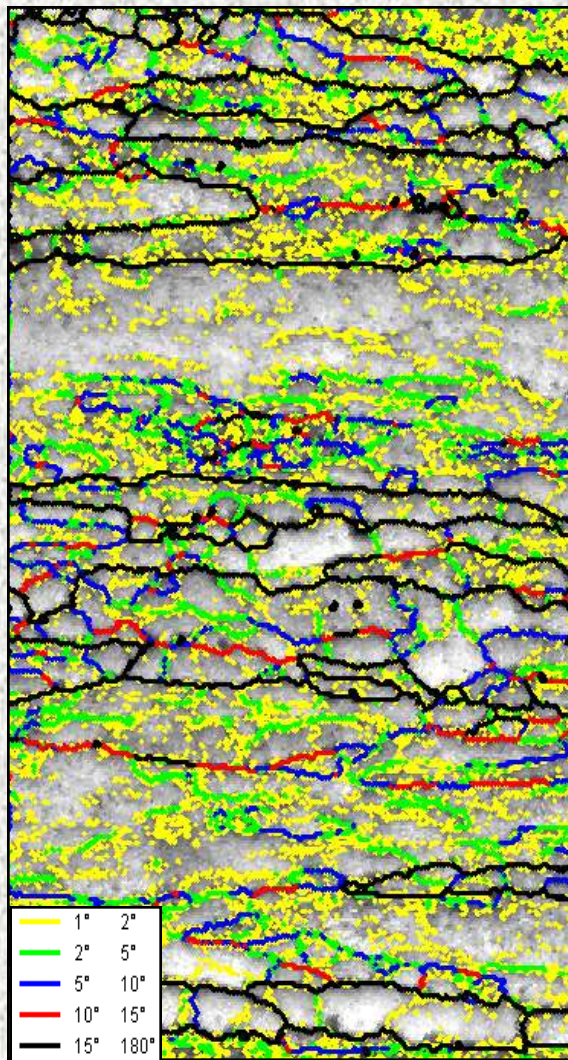
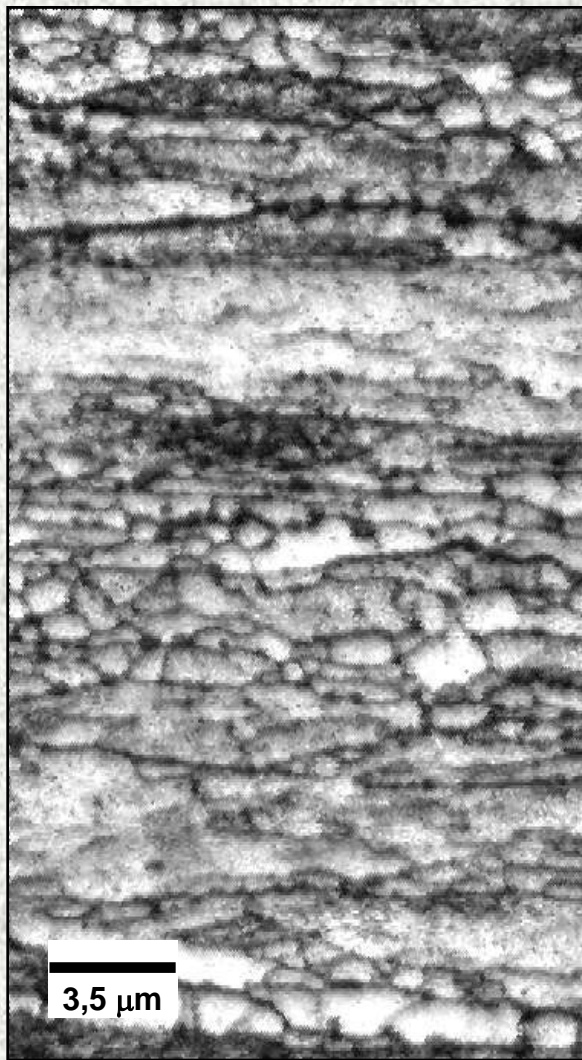
# Distribution of Cementite



**Begin**  
**CR 10 K/s, TD 550°C, CT 600°C**

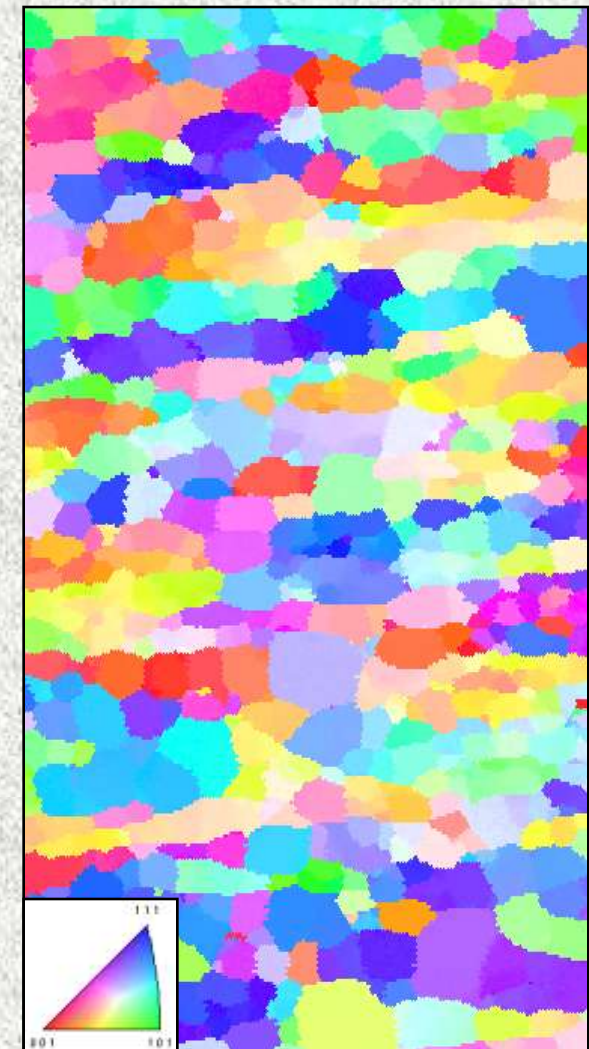
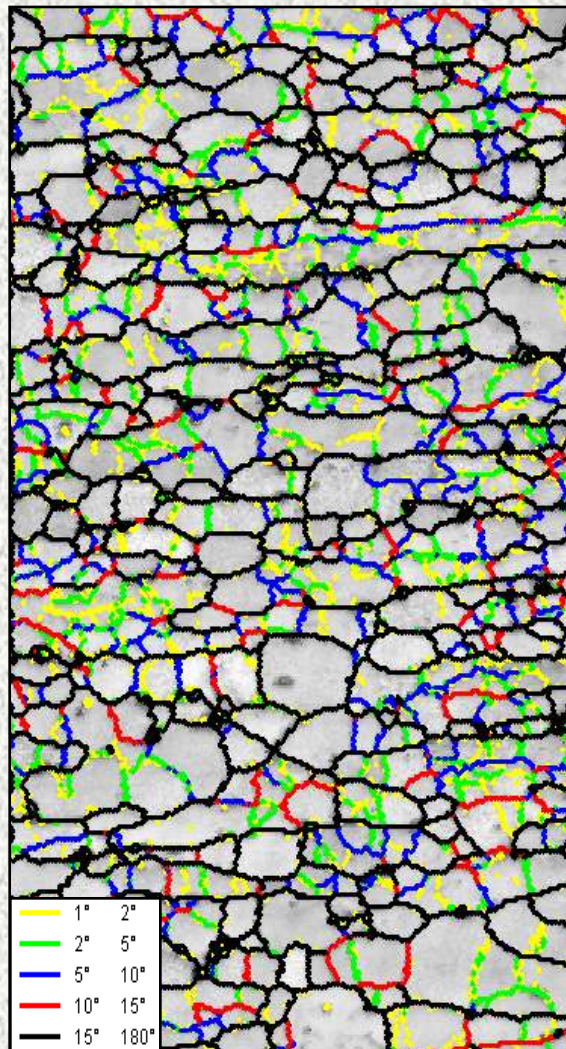
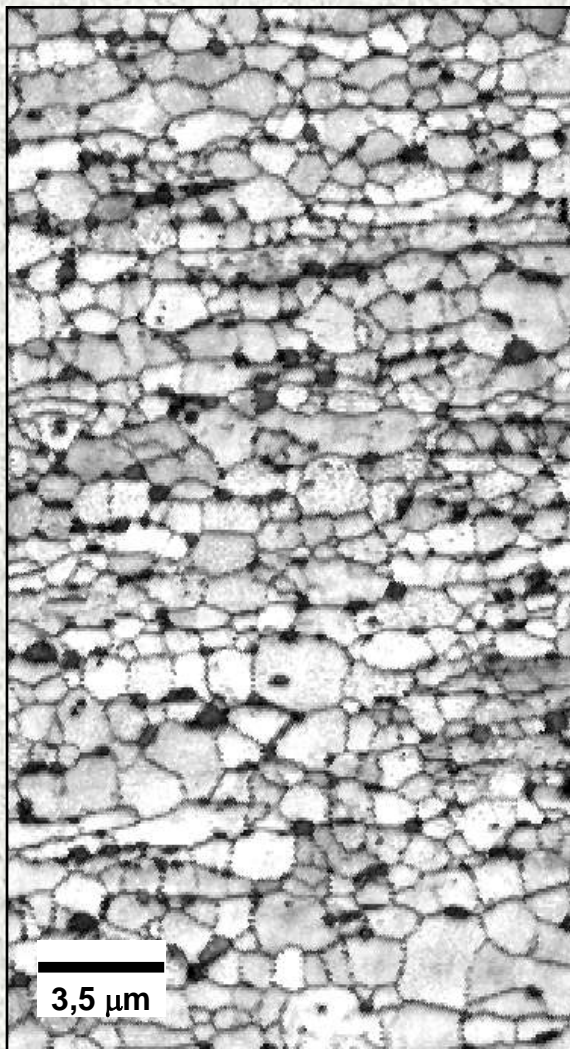
**End**  
**CR 10 K/s, TD 550°C, CT 650°C**

# Softening of Ferrite



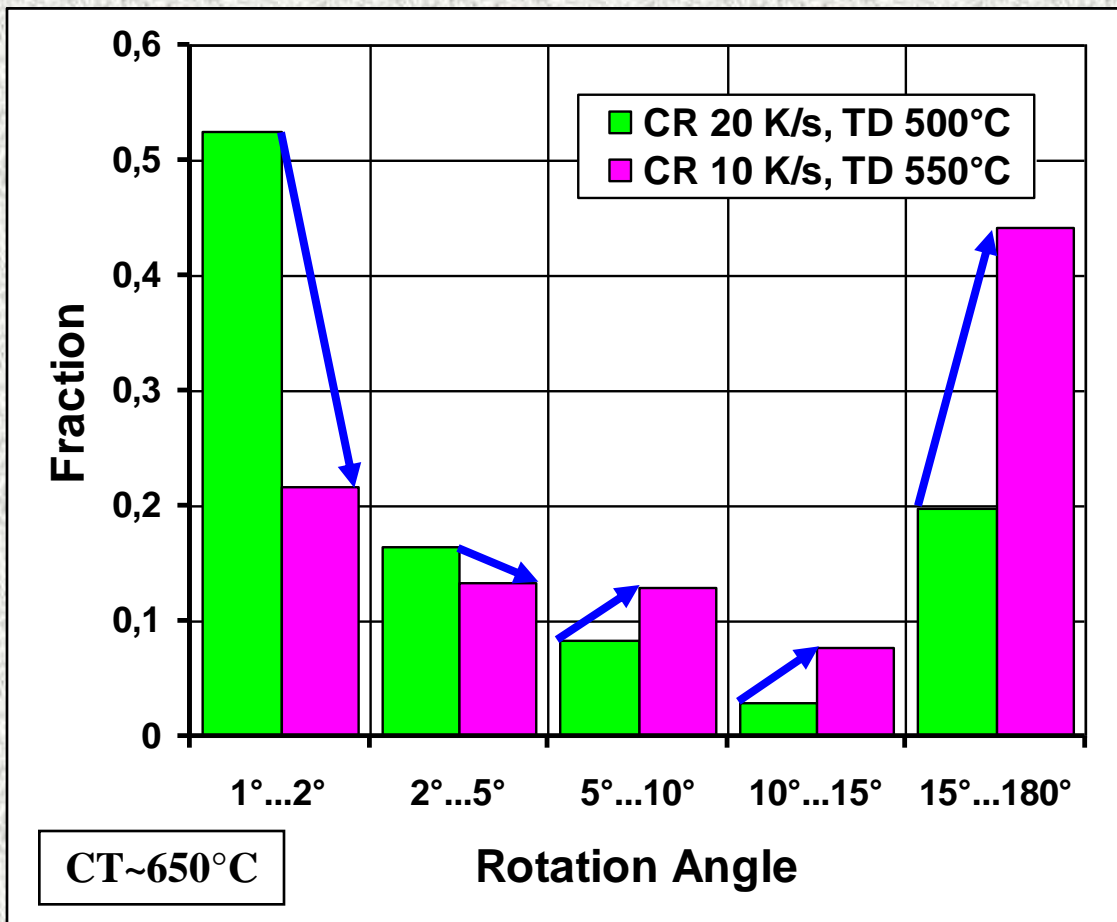
CR~20 K/s; TD~500°C; CT~650°C

# Softening of Ferrite

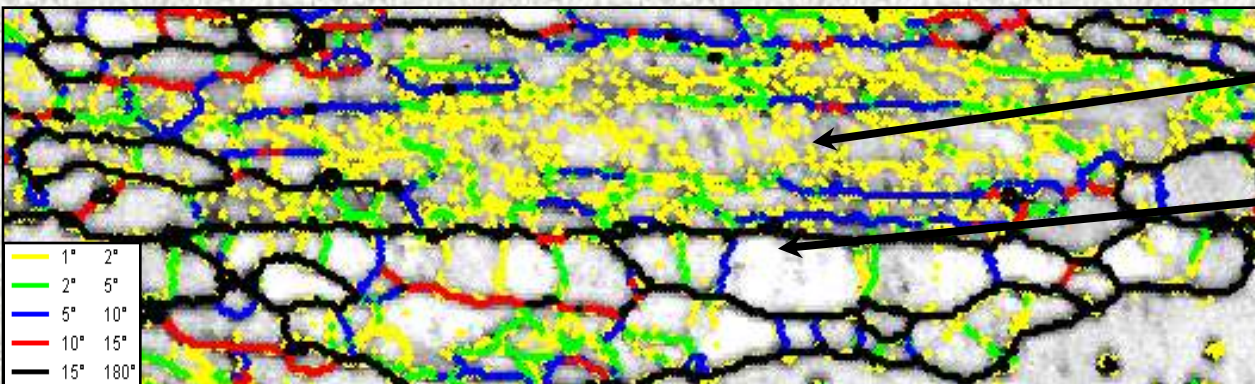
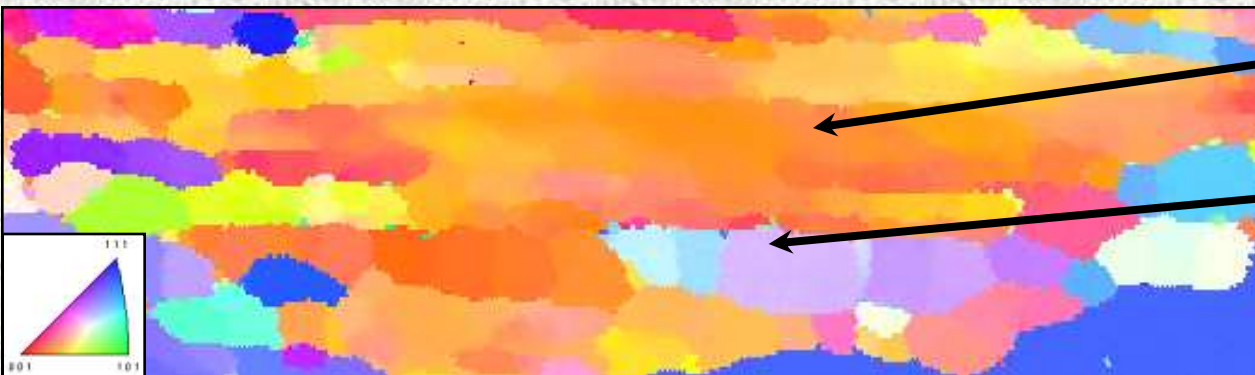
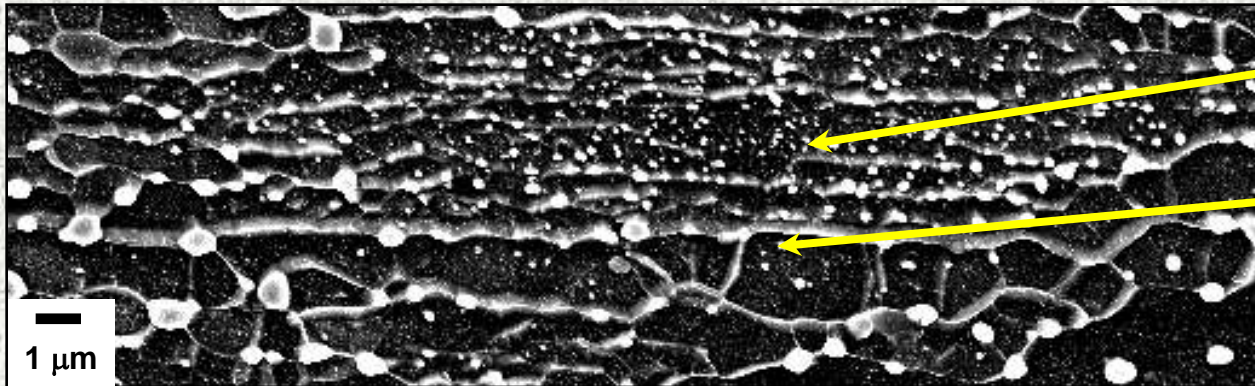


CR~10 K/s; TD~550°C; CT~650°C

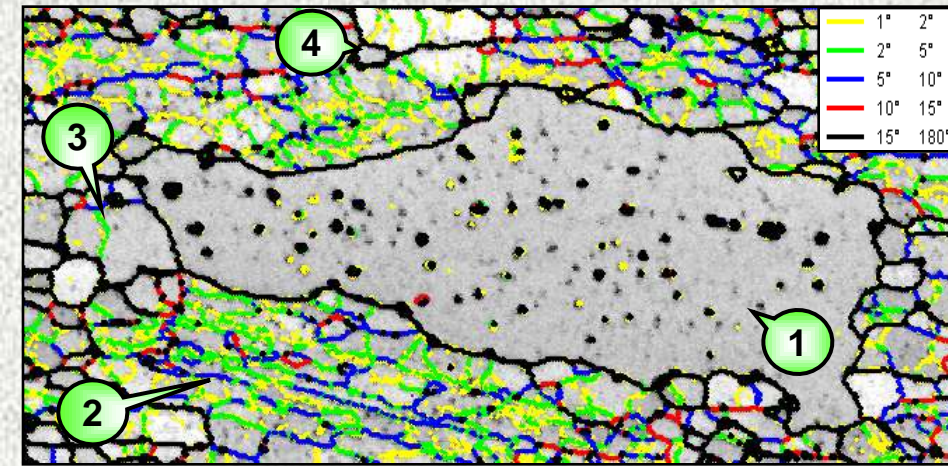
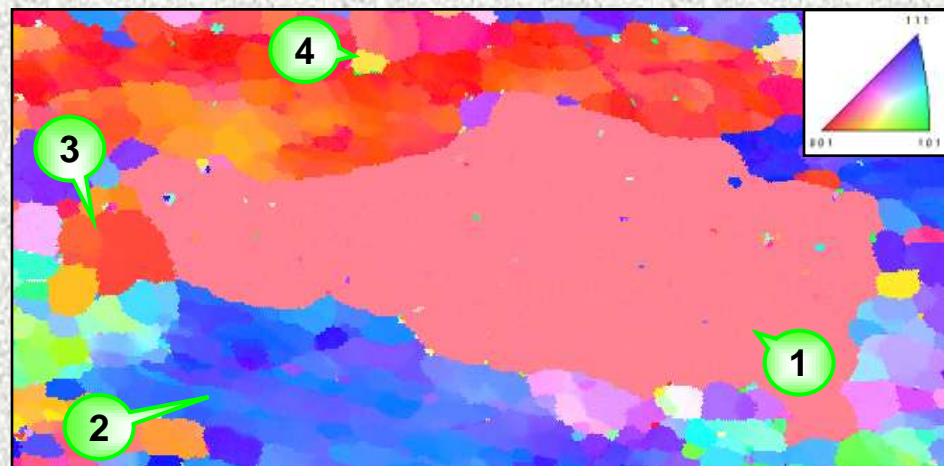
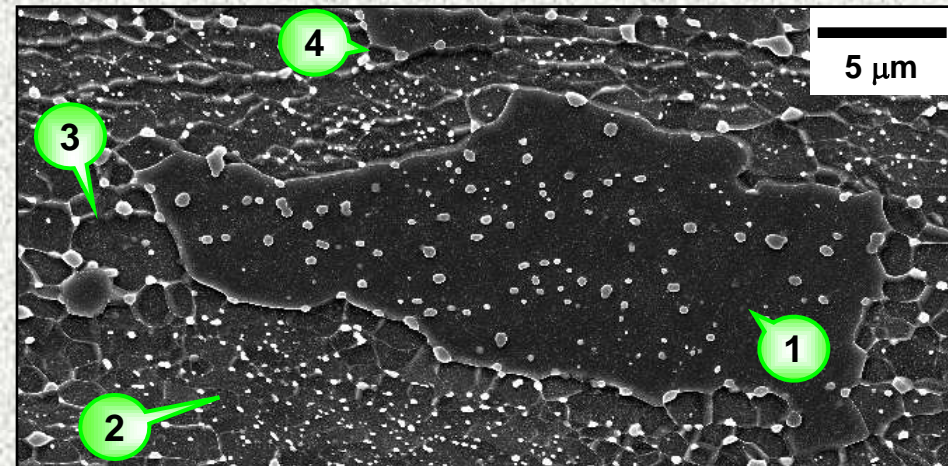
# Softening of Ferrite



# Effect of Cementite Distribution on Ferrite Softening



# Coarsening of Ferrite



**1. Coarse ferrite**

**2. Areas with fine cementite – recovery is not complete**

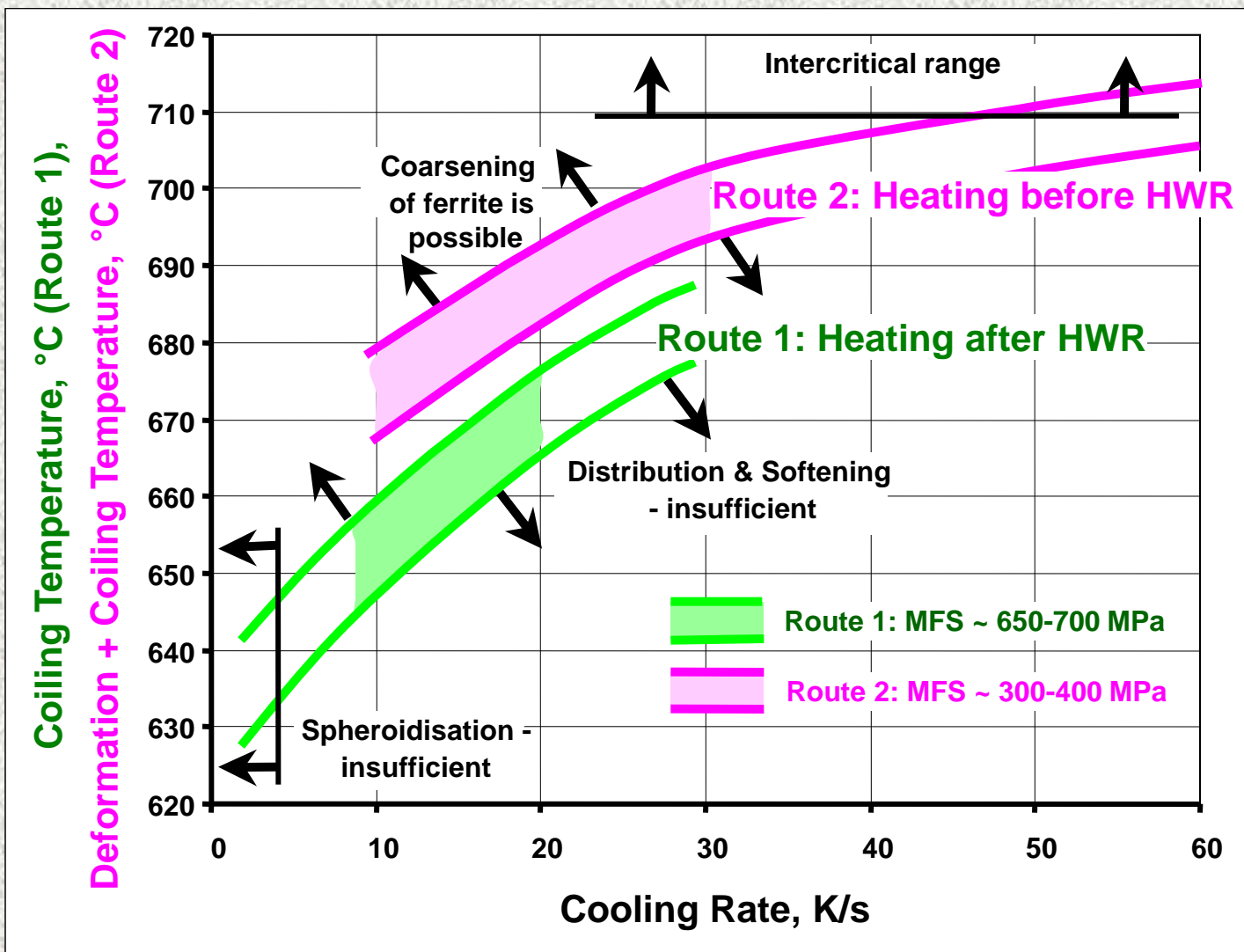
**3. Begin of coarsening – Coalescence of sub-grains?**

**4. Begin of coarsening – Perfect grain?**



- ✓ The Main Objectives
- ✓ PonyMill Concept
- ✓ Material and Experimental Technique
- ✓ Austenite Deformation
- ✓ Heavy Warm Deformation
- ✓ Microstructure Formation
- ✓ Summary

# Summary



# Development of microstructure and texture of medium carbon steel during heavy warm deformation

L. Storojeva <sup>\*</sup>, D. Ponge, R. Kaspar, D. Raabe

Max-Planck-Institut für Eisenforschung, Max-Planck-Str.1, Düsseldorf D-40237, Germany

Received 2 December 2003; received in revised form 12 January 2004; accepted 13 January 2004

## Abstract

The microstructure and texture development of a medium-carbon steel (0.36% C) during heavy warm deformation (HWD) was studied using scanning electron microscopy and electron back scattering diffraction. The spheroidization of pearlite is accelerated due to the HWD, which leads to the formation of completely spheroidized cementite already after the deformation and coiling at 873 K (600 °C). The homogeneity of the cementite distribution depends on the cooling rate and the coiling temperature. The cooling rate of about 10 K/s (ferrite–pearlite prior to HWD) and deformation/coiling at 943–973 K (670–700 °C) lead to a homogeneous cementite distribution with a cementite particle size of less than 1 μm. The ferrite softening can be attributed to continuous recrystallization. Even up to fairly high deformation/coiling temperatures of 983 K (710 °C) the texture consists of typical deformation components. During the continuous recrystallization the amount of high angle grain boundaries can increase up to 70% with a ferrite grain size of 1–3 μm. An increase of the cooling rate up to 20 K/s (ferrite–pearlite–bainite prior to HWD) deteriorates the homogeneity of the cementite distribution and the softening of ferrite in the final microstructure.

© 2004 Acta Materialia Inc. Published by Elsevier Ltd. All rights reserved.

**Keywords:** Heavy warm deformation; Ferritic–pearlitic steel; Continuous recrystallization; Texture; EBSD

## 1. Introduction

After conventional hot rolling of medium carbon steel, a lamellar pearlite is formed during  $\gamma$ – $\alpha$  transformation. The lamellar morphology of pearlite leads to mechanical properties unsuitable for a further cold treatment or for application in highly demanding components. The globular morphology of cementite provides some benefits such as high toughness, good cold formability and machinability. For such purposes the cold strip must either undergo a long annealing treatment to obtain higher cold formability or it must be quenched with a subsequent tempering for a good combination of strength and toughness.

The use of a heavy warm deformation (HWD), performed below the  $\gamma$ – $\alpha$  transformation-temperature accelerates essentially the spheroidization of pearlite.

The rate of this process is accelerated by a factor of  $10^4$  compared to annealing without deformation [1,2]. But the spheroidized cementite itself cannot provide good mechanical properties. Other microstructural features like a homogeneous cementite distribution or ferrite condition, as well as the size of the cementite particles or the ferrite grains, influence the final mechanical properties. Therefore, a better understanding of the microstructure evolution during HWD is important for a successful introduction of such processing into the industrial production.

## 2. Material and experimental technique

A ferritic–pearlitic steel with a following composition in mass % was studied: 0.36% C, 0.53% Mn, 0.22% Si, 0.011% P and 0.002% S. The axially symmetric compression of samples with initial size  $18 \times 18 \times 30$  mm<sup>3</sup> and plane strain compression of samples with an initial thickness of 60 mm, width of 50 mm and length of 45

<sup>\*</sup> Corresponding author. Tel.: +49-211-679-2260; fax: +49-211-679-2333.

E-mail address: [storojeva@mpie.de](mailto:storojeva@mpie.de) (L. Storojeva).

mm, cut from an industrial slab, were carried out on the hot deformation simulator of the Max-Planck-Institute [3] with a strain rate of  $10\text{ s}^{-1}$ . This servohydraulic press is capable of conducting large-scale thermomechanical processes by performing multi-step hot compression tests as a realistic approximation of industry-scale hot forming operations.

After the austenite deformation (true strain of 0.3) at 1173 K (900 °C), the samples were cooled with various cooling rates between 2 and 20 K/s to obtain the  $\gamma$ - $\alpha$  transformation. The HWD was carried out at 873–983 K (600–710 °C) using a multi-pass mode (4 passes  $\times$  0.4 strain, interpass time around 0.5 s) with a subsequent cooling simulation at 873–983 K (600–710 °C) for 2 h.

The deformation-dilatometry technique was used for the establishment of CCT diagrams after the deformation in austenite. The microstructure investigation was carried out using scanning electron microscopy. The condition of the ferrite was additionally studied by the electron back scattering diffraction (EBSD).

### 3. Results and discussion

#### 3.1. CCT diagram

The continuous cooling transformation diagram (Fig. 1) was established after an austenite deformation at 1173 K (900 °C). This temperature was determined by pre-tests to provide fine recrystallized austenite grains as an initial microstructure before the transformation.

The main differences between the microstructures produced with different cooling rates (initial microstructures for the subsequent HWD) were the amount of proeutectoid ferrite, the presence of bainite and the

thickness of pearlite lamellae. After slow cooling (2 K/s) the microstructure contains coarse lamellar pearlite with a thick network of proeutectoid ferrite. After cooling with a faster cooling rate of 8 K/s, the ferrite network is thinner and the lamellae are finer. After higher cooling rates (30 K/s), the microstructure contains fine lamellar pearlite, bainite and martensite with only a small amount of ferrite.

#### 3.2. Spheroidization of pearlite

Pearlite colonies with a different orientation after HWD with subsequent cooling at a low rate, 2 K/s, and deformation/cooling temperatures of 873 K (600 °C) are shown in Fig. 2(a) and (b). The formation of spheroidized cementite particles along the former pearlite lamellae can be seen. According to Chattopadhyay and Sellars [4], an excess of vacancies, which formed during the deformation, promotes carbon diffusion, especially near lamellae kinks, which are characteristic of severely deformed pearlite [2,5]. An important factor for the acceleration of the spheroidization process can be a local difference between the equilibrium carbon concentrations in ferrite near the surface of a deformed lamella with different curvature radii, according to the Gibbs-Thompson equation. As reported in [6,7], the equilibrium carbon concentration in ferrite in the vicinity of the lamella with a small curvature radius is higher compared to that of larger one. After a heavy deformation of pearlite the numerous kinks of the lamellae occur with small radii and so with the equilibrium carbon concentration in ferrite near kinks essential higher as compared to that close to the flat parts of lamellae. Together with the high defect density the carbon diffusion leads to a rapid dissolution of lamellae kinks and a simultaneous deposition of carbon in the flat cementite lamella.

The fracture of lamellae (cf. Fig. 2(b), single arrow) in the pearlite colonies with lamellae oriented perpendicular to the rolling direction can also accelerate the spheroidization. Fragments of the former lamellae located at a prior austenite grain boundary (cf. Fig. 2(b), double arrow) can easily be formed because of an accelerated diffusion along the boundary, which leads to a faster coarsening of these cementite fragments.

For the case of a heavy deformation the substructure of the pearlite lamellae can also exhibit an essential effect on the spheroidization process. As reported in [7], the interface adjacent to the subboundary in the cementite lamella with a large local curvature and the surrounding ferrite provokes a quick carbon dissolution that leads to a local lamella division (double arrow in Fig. 2(c)).

The start of the spheroidization of the cementite lamellae in the vicinity of ferrite subboundaries, as reported in [8], was also observed (cf. Fig. 2(c), single arrow). In this case the subboundary facilitates the deposition of carbon in contact place with the lamella. But

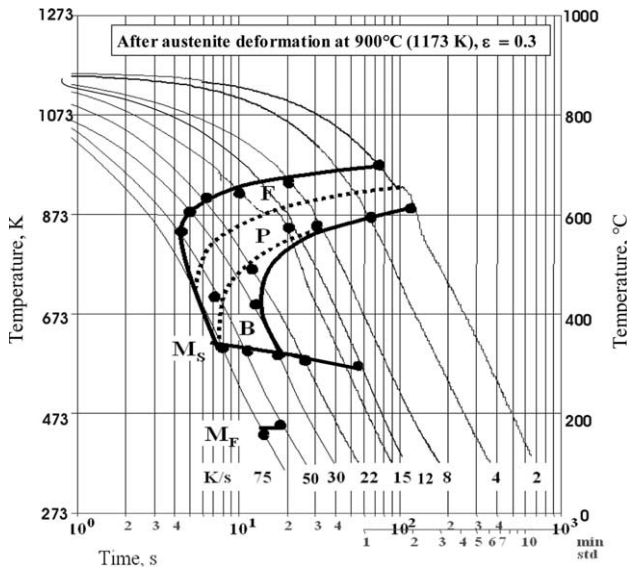


Fig. 1. CCT diagram after austenite deformation.

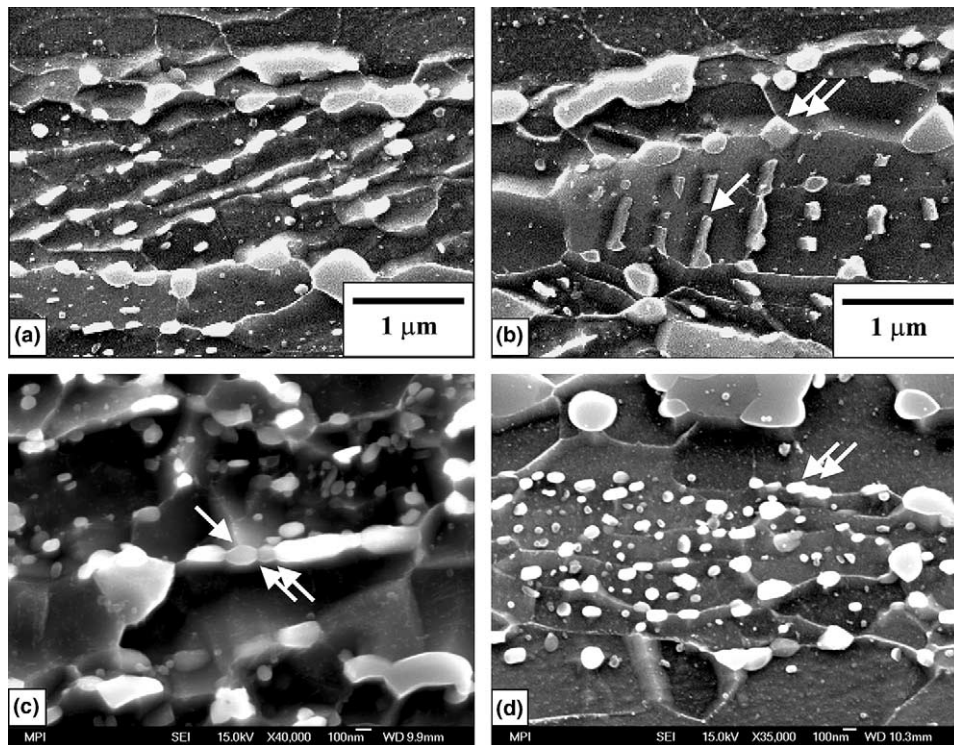


Fig. 2. Spheroidization of pearlite: (a) cementite particles along the former lamellae; (b) fracture of lamellae (single arrow) and the lamella fragments at a prior austenite grain boundary (double arrow); (c) enhancing effect of ferrite boundary (single arrow) and cementite subboundaries (double arrow) on start of spheroidization and (d) former pearlite colony (double arrow shows the spheroidization of kinked lamella).

this mechanism does not seem to have a first-order effect for a heavily warm deformed steel. The present EBSD study has shown that the processes of spheroidization and redistribution of cementite take place already in a deformed ferrite, when subboundaries do not yet exist.

The appearance of a typical former pearlite colony at the end of the spheroidization process is shown in Fig. 2(d). Along the former lamellae the ferrite boundaries with the cementite chains can be seen. The ferrite between the chains is elongated and seems to be deformed. Some cementite particles have a prolonged form. The spheroidization of the last kinked lamella can be also observed (cf. Fig. 2(d), double arrow).

### 3.3. Distribution of cementite

Apart from the processes of spheroidization and coarsening of cementite, which are typical for eutectoid steels [1], the process of a homogeneous distribution of cementite after the spheroidization in the present ferritic–pearlitic steel have been observed. This means that after HWD with a subsequent coiling even within the former proeutectoid ferrite regions cementite particles can also be found. The various stages of the cementite redistribution after a cooling rate of 10 K/s and deformation/coiling temperatures 873–943 K (600–670 °C) are shown in Fig. 3. At an early stage of the redistribution process, accomplished here by using a rather low

deformation/coiling temperature of 873 K (600 °C) (cf. Fig. 3(a)), the microstructure contains proeutectoid ferrite without cementite particles and fine spheroidized cementite particles (with a size of about 0.1 μm) that are located at the areas of former pearlite colonies. So, after a complete spheroidization the distribution of cementite is not homogeneous. However, during the deformation/coiling at higher temperatures, the fine cementite particles may dissolve and some carbon atoms are assumed to diffuse from the areas of the former pearlite colonies to the cementite free areas of the former proeutectoid ferrite followed by a subsequent reprecipitation and coarsening (cf. Fig. 3(b) and (c)). As a result (cf. Fig. 3(d)) the cementite particles with a size of about 1 μm are distributed rather homogeneously in the ferritic matrix.

As reported in [9,10], the phenomenon of pearlite-colony dissolution during the annealing of a low carbon titanium microalloyed steel after cold rolling [9] and low carbon vanadium microalloyed steel after severe plastic deformation [10] was observed. In these cases the microalloying elements cause an increase in the recrystallization temperature. The main condition for the redistribution of cementite, as shown in [10], seems to be a high dislocation density in the heavily deformed former pearlite colonies that was estimated to be of the order of  $10^{16} \text{ m}^{-2}$ . In case of plain low carbon steel [9,10] with low recrystallization temperature, these

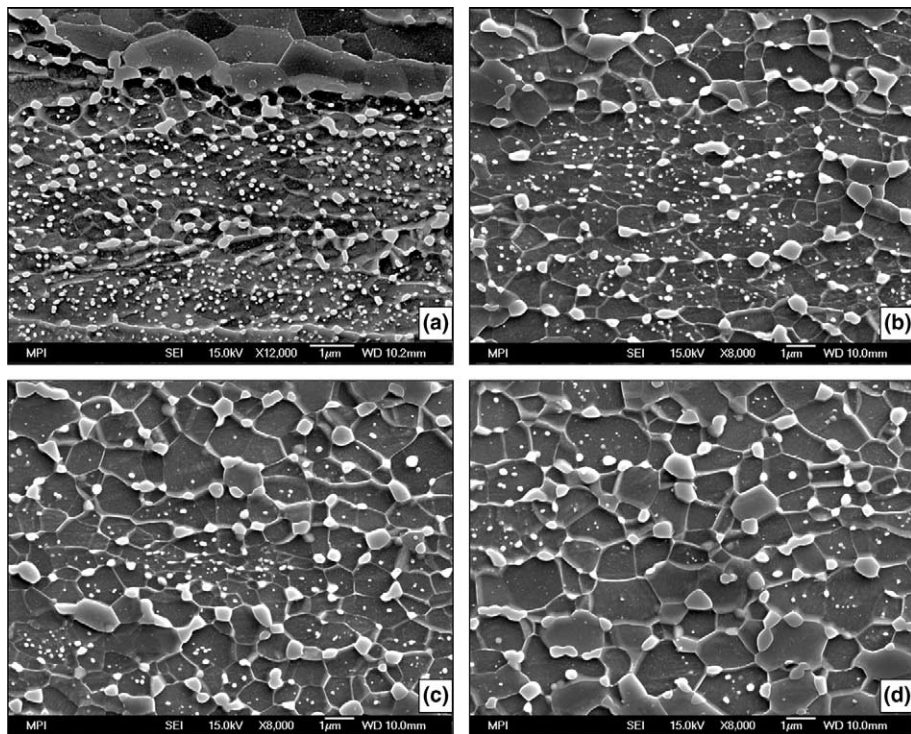


Fig. 3. Effect of deformation/coiling temperature on cementite distribution after cooling rate 10 K/s: (a) 873 K (600 °C); (b) 923 K (650 °C) and (c,d) 943 K (670 °C).

treatments did not lead to the disappearance of pearlite colonies. In this steel a recrystallization would slow down or even stop this process by significantly reducing the dislocation density. This means that a higher recrystallization temperature offers the possibility that even at fairly high temperatures, when the cementite dissolution already starts, only recovery takes place. In this situation the dislocation density will not be reduced very much, so that the redistribution of cementite can take place rapidly assisted by a fast dislocation pipe diffusion. On the other hand, in the case of a low recrystallization temperature the recrystallization begins before the start of cementite dissolution, the dislocation density decreases drastically and a decomposition of colonies does not take place.

A driving force for the redistribution can be a gradient of the solute carbon. Inside the former colony around the fine cementite particles the carbon concentration is essentially higher compared to the proeutectoid ferrite. The high density of dislocations and vacancies during or after HWD facilitates the solute carbon diffusion to areas of lower carbon concentration, i.e., proeutectoid ferrite, with subsequent reprecipitation in the most energetically favorable places such as triple joints of ferrite grain boundaries (cf. Fig. 3(d)). Additionally, due to the faster grain boundary diffusion, the particles located on grain boundaries and triple junctions will have a size advantage in the later Ostwald-ripening process.

### 3.4. Softening of ferrite

The various stages of ferrite softening after a cooling rate of 10 K/s and deformation/coiling temperatures in the range of 903–983 K (630–710 °C) are shown in Fig. 4(a). After deformation at 903 K (630 °C) and coiling at the same temperature, the formation of numerous subgrains with low angle boundaries can be observed. These subgrains remain inside the original deformed grains without growth into neighboring grains. Considering only the high angle grain boundaries, it is obvious that the grains are highly elongated in the rolling direction. The amount of high angle grain boundaries (with misorientation angle >15°) is about 50%. After the increase of the deformation/coiling temperature up to 983 K (710 °C), the fraction of high angle grain boundaries increases up to 65–70%, and the microstructure contains fine equiaxed ferrite grains. However, it seems that most of these grains keep the original orientations of the former deformed grains. For example, the areas with the orientation near {111} (cf. Fig. 4(a), single arrow) or near {001} (cf. Fig. 4(a), double arrow) consist of fine subgrains with low angle boundaries, which are characteristic for the microstructure up to the highest studied subcritical temperature 983 K (710 °C).

The ODF sections in Fig. 4(b) show that the texture of the steel essentially does not change after the various deformation/coiling temperatures, containing mainly  $\gamma$

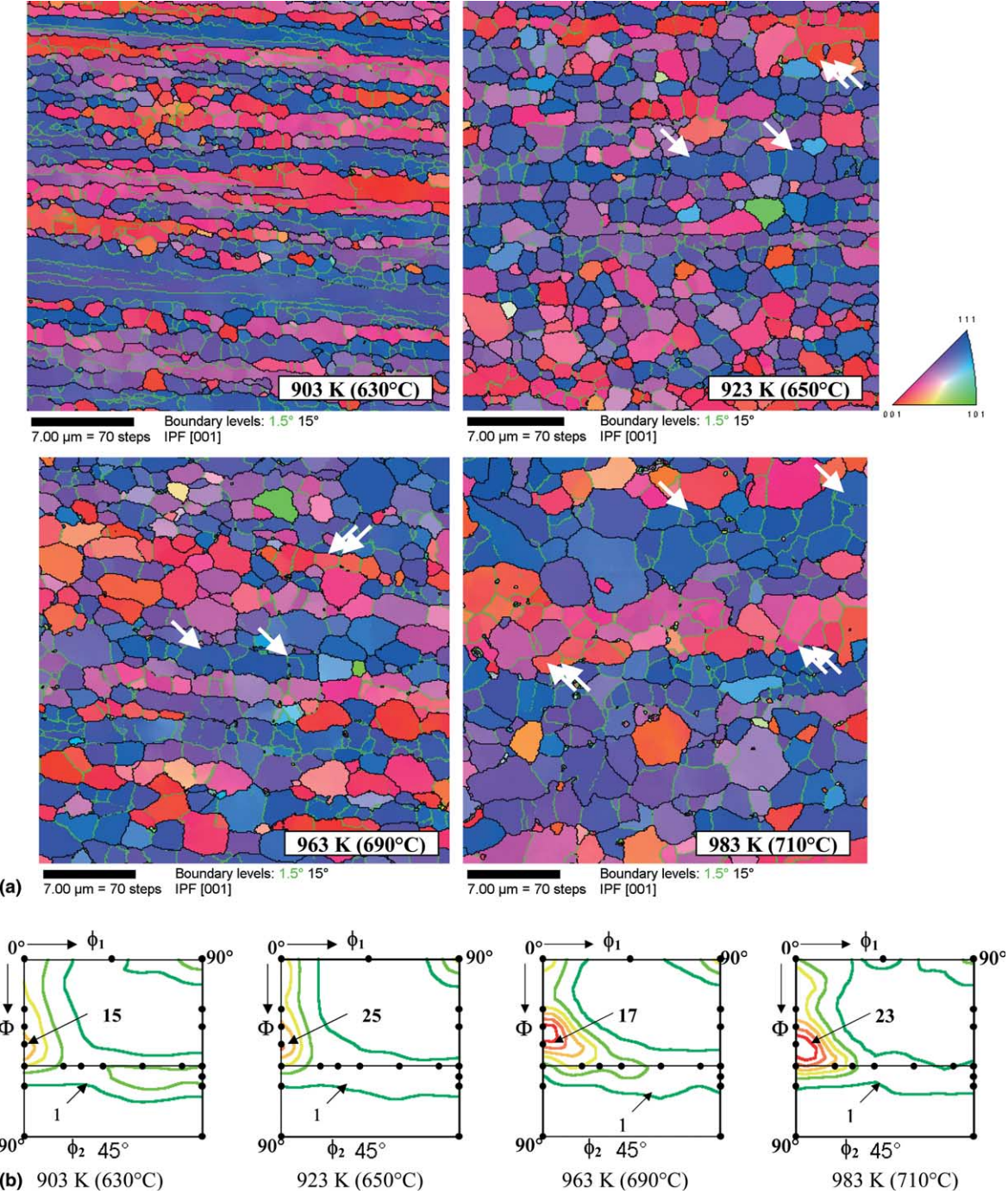


Fig. 4. EBSD images (a) and ODF section  $\phi_2 = 45^\circ$  (b) after the various deformation/coiling temperatures.

and  $\alpha$ -fibers with a maximum near  $\{1\bar{1}2\}\langle1\bar{1}0\rangle$ , which is typical for rolling texture [11,12].

The distribution of grain/subgrain boundaries misorientations (Fig. 5) for the deformation/coiling temperatures 903 K (630 °C) and 983 K (710 °C) are very similar. They both show a high fraction of low angle grain boundaries with small misorientation angles. The increase of the temperature by 80 K leads only to a continual decrease of the low angle fraction ( $<15^\circ$ ) with

a simultaneous increase of the fraction of high angle boundaries. (Because of the orientation noise in the EBSD measurements misorientations less than  $1.5^\circ$  have been omitted).

The distribution of the ferrite grain size (Fig. 6) shows also a continuous change of the microstructure with increasing HWD temperature. After the temperature 630 °C (903 K), the absolute maximum of the area fraction corresponds to the grain size of around 2  $\mu\text{m}$ . A

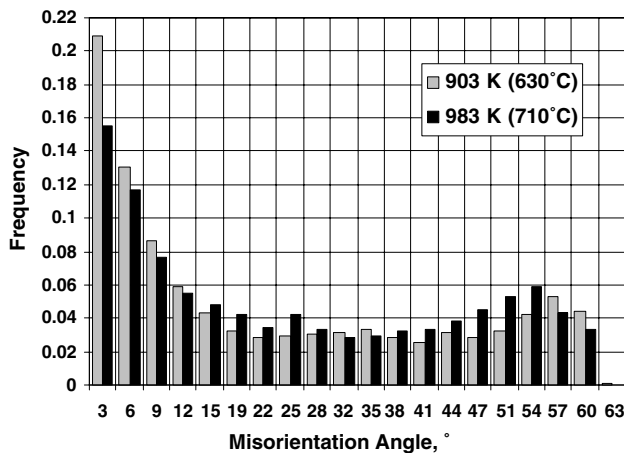


Fig. 5. Distribution of grain/subgrain boundaries misorientations.

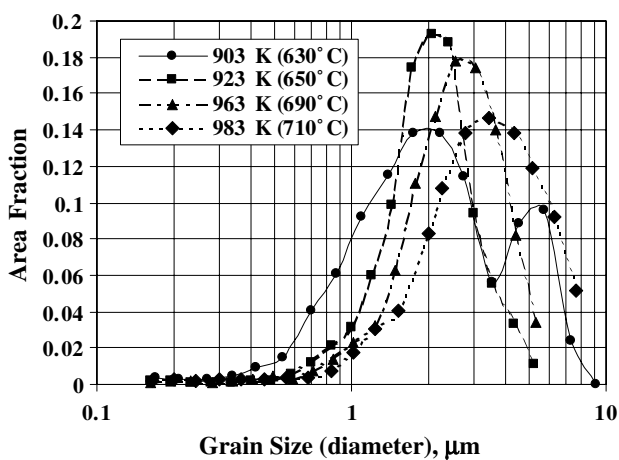


Fig. 6. Area fraction of ferrite grain size after the various deformation/coiling temperatures.

further local maximum near 6  $\mu\text{m}$  can be attributed to the large deformed ferrite grains still without substructure. After the deformation/coiling at 923 K, the curve exhibits a fairly sharp maximum for grain sizes around 2.2  $\mu\text{m}$ . The further increase of the temperature leads to a shift of the maximum area fraction to larger grain sizes up to 3.5  $\mu\text{m}$  for 983 K.

Thus, the results of the study suggest that the ferrite softening during the deformation with the subsequent coiling can be attributed to recovery processes (i.e., polygonization), called also continuous recrystallization or recrystallization *in situ*. In this case the subgrains form within the deformed matrix and grow, so that the dislocation density decreases due to the reduction of subgrain boundaries area and, finally, formation of high angle grain boundaries.

The reasons that only recovery and not primary recrystallization takes place here may be described as follows. Due to the lamellae spheroidization, a fine dispersion of cementite particles are present in the

microstructure. These particles lead to a high dragging force for the migration of high angle grain boundaries due to Zener pinning of the boundaries that increases the recrystallization temperature. On the other hand, it is known that due to high stacking fault energy the recovery in ferrite can proceed very quickly. In this case the dislocation-rearrangement to form energetically more favorable configurations starts everywhere, but the subsequent migration of high angle grain boundaries may be stopped very soon by the particles.

The recovery process decreases both the stored energy and the local stored energy gradient, which slows down the successful nucleation or growth. Moreover, an increased amount of solute carbon in ferrite during the HWD and the redistribution of cementite due to the spheroidization process can retard both the formation and migration of high angle boundaries.

At higher temperatures, the homogeneously distributed relatively fine cementite particles produce a stabilizing effect on the fine grained ferrite matrix. But the coarsening of the cementite particles leads to a reduction of the Zener drag effect, so that primary recrystallization and grain growth can occur.

Because the recovery processes involve a short-range interaction between dislocations and subgrain boundaries, or between adjacent boundaries, they may lead to a sharpening of deformation texture and a higher intensity of deformation texture components, which can be seen in Fig. 4(b).

The start of the formation of low angle subgrain boundaries due to dislocation rearrangement in a deformed grain is shown in Fig. 7(a) (EBSD image and misorientation profile). The initial deformed grain with the main orientation component near {111}, with a length of more than 10  $\mu\text{m}$  and a width in normal direction of 1–1.5  $\mu\text{m}$  contained initially (after the deformation) a high density of excess dislocations, which resulted in a fairly high long-distance misorientation gradient  $\sim 0.5\text{--}1^\circ/\mu\text{m}$  along the rolling direction. The climb and cross slip of dislocations lead to their rearrangement as low angle boundaries. The misorientation profiles allow observation the beginning of subgrain formation. The plateaus at the “point-to-origin” profile evidently can be attributed to new subgrains with low angle boundaries near  $1^\circ$ , as shown in the “point-to-point” profile.

The formation of low angle subboundaries in progress is shown in Fig. 7(b). In the initial deformed grain with an orientation component near {112}, the low angle boundaries between new subgrains already have higher misorientation angles up to  $9^\circ$ , with a subgrain size of about 1–3  $\mu\text{m}$ .

An increase in temperature leads to the continuous decrease of the fraction of low angle boundaries along with a simultaneous increase of high angle ones (cf. Fig. 5). As a result, the amount of high angle boundaries

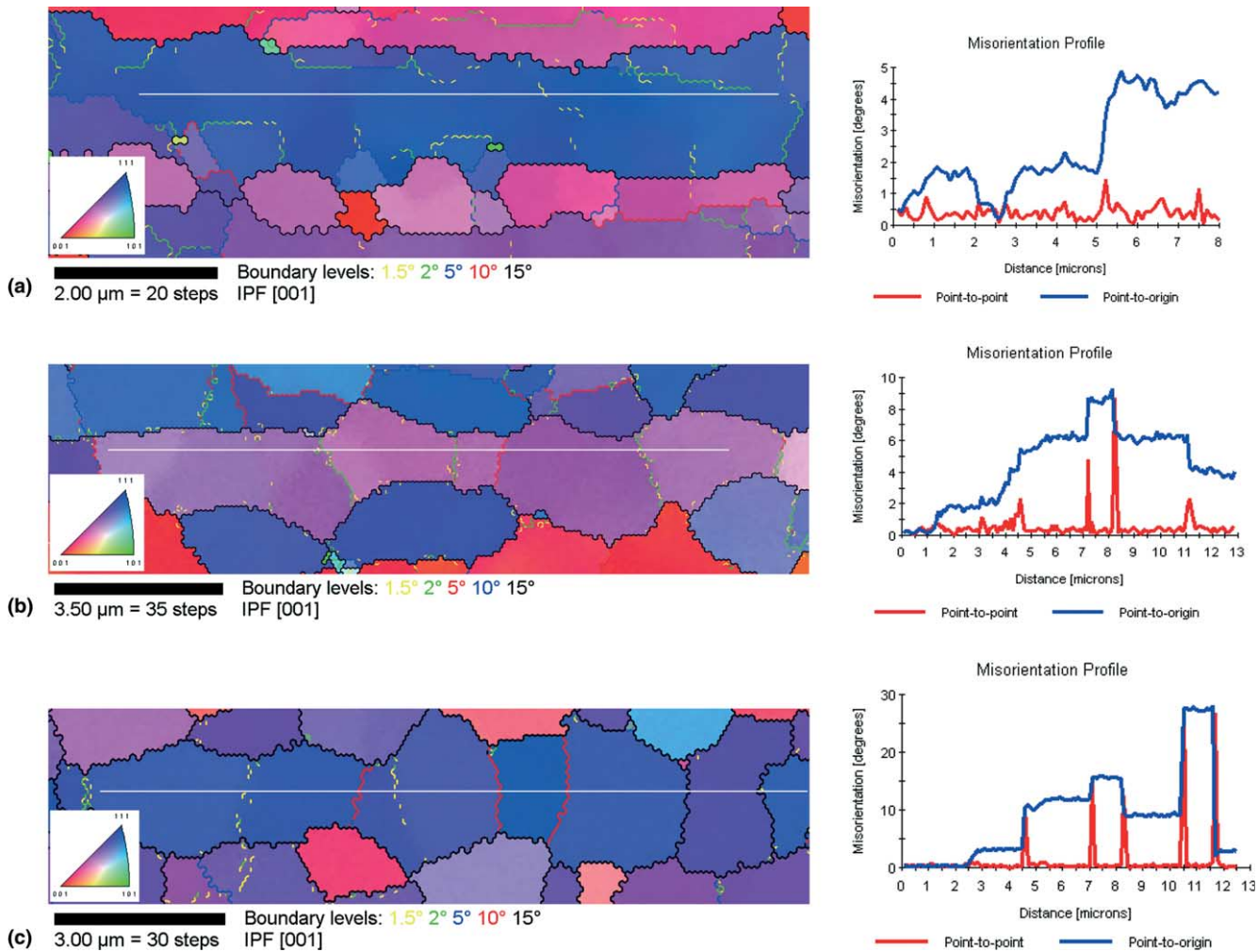


Fig. 7. Formation of (sub)grain boundaries during continuous recrystallization: (a) start of low angle subgrain boundaries formation; (b) formation of low angle subgrain boundaries in progress and (c) formation of high angle grain boundaries due to dislocation accumulation on low angle boundaries.

increases up to  $\sim 70\%$ . As shown in literature, the continuous recrystallization clearly contributes to the formation of new high angle boundaries. The possible mechanisms are the accumulation of dislocations at the subgrain boundaries [13], the increase of misorientation angle by the merging of lower angle boundaries during subgrain coalescence [14,15] and the subgrain growth with migration of low angle boundaries via dislocation motion [16]. In the postmortem analysis carried out in this work it is not possible to prove exactly, which mechanism is really active or relevant for the microstructure development. Nevertheless, some of the interesting features found in the microstructures will be discussed to illustrate the possible mechanisms of continuous recrystallization in studied steel.

The increase of boundary misorientation that can be attributed to the accumulation of dislocations into subboundaries is shown in Fig. 7(c). A strained grain is separated into several subgrains of similar orientation

around  $\{111\}$ . One of these (sub)grains already exhibits misorientations of up to  $25^\circ$  to the neighboring (sub)grain.

Subgrain coalescence is often reported to be a very slow process. Nevertheless, the microstructure in Fig. 8(a) might be contributed by the coalescence of two subgrains with orientation near  $\{111\}$  and misorientation  $\leq 1^\circ$  (see misorientation profile, Fig. 8(b)). As reported in [17], the coalescence can be favorable in case of joining subgrains surrounded by high angle boundaries. This condition is completely fulfilled for subgrains A1 and A2, which are surrounded by high angle boundaries ranging from  $20^\circ$  up to  $47^\circ$ . Preferential subgrain coalescence may occur since the driving force for subgrain merging comes from the difference between the higher energy of dislocations in the low angle boundary and the lower energy of the dislocations in the high angle boundaries. Since the high angle boundaries around two subgrains with low misorientation do not occur often, the coalescence of subgrains is observed

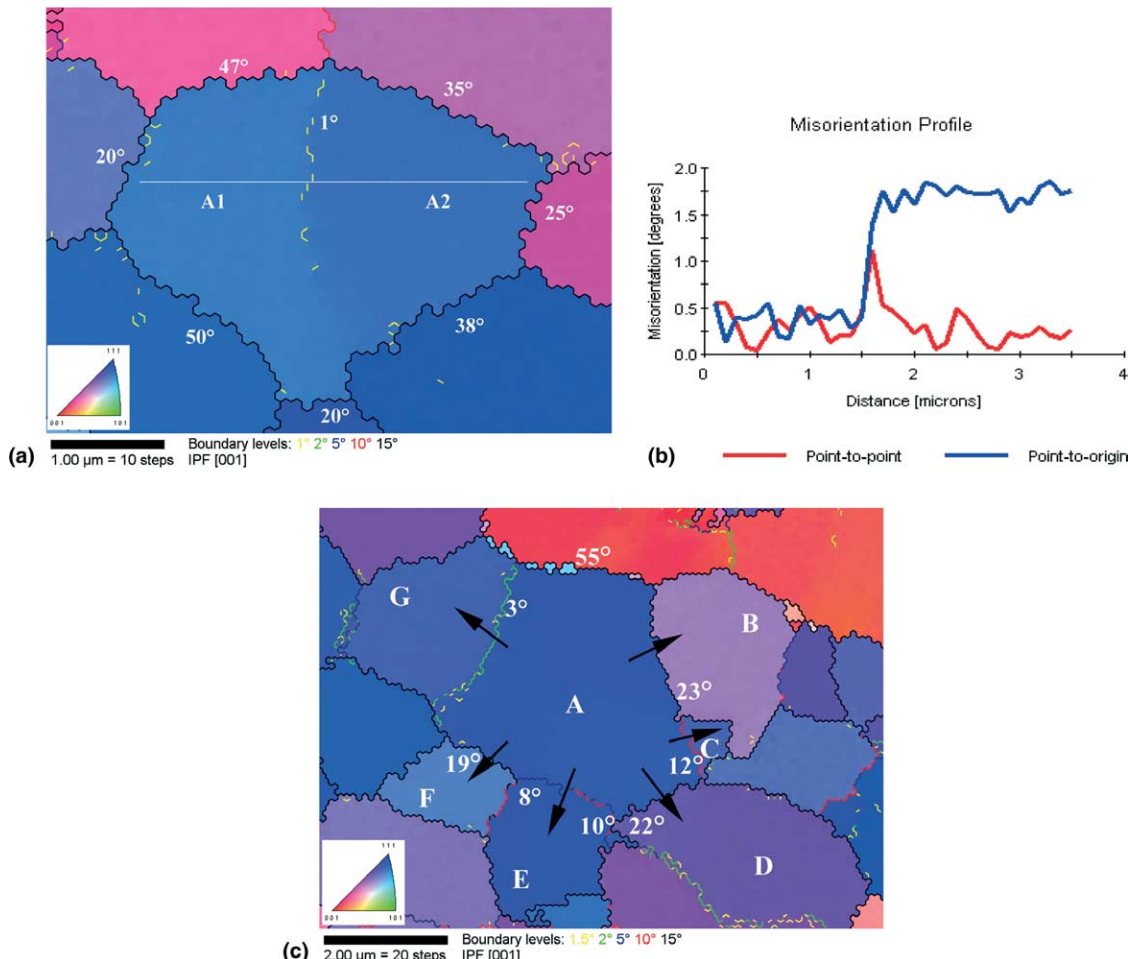


Fig. 8. The processes of two subgrains coalescence: (a) EBSD image, (b) misorientation profile and (c) subgrain growth (EBSD image); the misorientation angles between grains are shown.

only rarely, compared to other mechanisms of continuous recrystallization.

The possible subgrain growth is shown in Fig. 8(c). The curvature of the boundaries indicates the growth of the subgrain A with orientation near {111} at the expense of the adjacent (sub)grains (see arrows). Apart from the high angle boundaries migration (between grain A and the each of grains B, D and F, the boundaries have misorientations of about 20°), the migration of low angle boundaries can be observed (AC 12°, AE near 9° and the boundary between A and G has a misorientation angle only about 3°).

As reported in [18], low angle boundaries in general have a low mobility. The reason is the different structure of high and low angle boundaries. For high angle boundaries, migration can occur easily by single atom jumps across the rather open grain boundary structure. Low angle boundaries composed of dislocation arrays migrate by the motion of dislocations, i.e., a coordinated movement of atoms. While the motion of an individual dislocation by glide is easy, the motion of an array might

be more difficult, since motion of the arrays causes a change in shape of the two subgrains, which is resisted by surrounding subgrains. As reported in [18], the limitative process of the array motion is the climb of edge dislocations and the activation energy of the process has the order of magnitude of the activation energy for self-diffusion. On the other hand, as shown in [19], even a rather low deformation leads to a decrease of the self-diffusion activation energy.

The activation energy of the (sub)grain growth with the increase of the deformation/coiling temperature was estimated using the (sub)grain size with the maximum area fraction (cf. Fig. 6).

The estimation was carried out based on the following considerations. As shown in [18], for isothermal annealing a time law of the form

$$d = (at)^n \quad (1)$$

is frequently found, where  $d$  is grain size,  $t$  is time, and  $n$  and  $a$  are constants. As reported in [20,21],  $n \leq 0.5$ , in [19]  $n = 0.5$ .

As shown in [19,21] the increase in temperature leads to the exponential increase of constant  $a$  that has the nature of a diffusion coefficient [19]

$$a = a_0 \exp(-Q/RT), \quad (2)$$

where  $Q$  is the activation energy of grain growth,  $T$  is the absolute temperature and  $a_0$  is constant. For isochronous conditions

$$d = d_0^n \exp(-nQ/RT), \quad (3)$$

and a plot of  $\ln d$  versus  $1/T$  allows for determining the activation energy  $Q$  of grain growth from the gradient  $(-nQ/RT)$ .

The plot of  $\ln d$  versus  $1/T$  is shown in Fig. 9. It can be seen that for temperatures 903–963 K (630–690 °C), the process has a lower activation energy compared to the grain growth in a range 963–983 K (690–710 °C). Here, it should be mentioned that the point for 903 K (630 °C), where the process of subgrain formation only starts, apparently can be assigned to the line 923–963 K (650–690 °C), where the process is in progress. Assuming that  $n = 0.5$ , the activation energies at lower and higher temperature ranges can be calculated as 71 and 205 kJ/mol, respectively. According to Kristal [19], the lower  $Q$  can be attributed to the activation energy of interstitial elements diffusion (carbon or nitrogen), the higher  $Q$  has the order of magnitude of the self-diffusion activation energy of deformed ferrite. This might mean that the limiting factor of ferrite softening at the temperatures up to 963 K (690 °C) is carbon diffusion during the spheroidization and distribution of cementite.

### 3.5. Effect of cementite on ferrite softening

Just after the spheroidization (cf. Fig. 3) the size of cementite particles can be about 0.1 μm. The presence of these fine cementite particles retards the softening of ferrite in the areas of the former pearlite colonies. The microstructure of steel with fine cementite is shown in

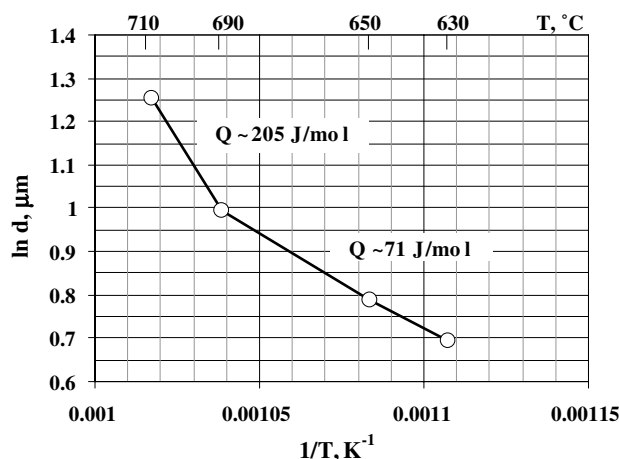


Fig. 9. Different stages of ferrite grain growth.

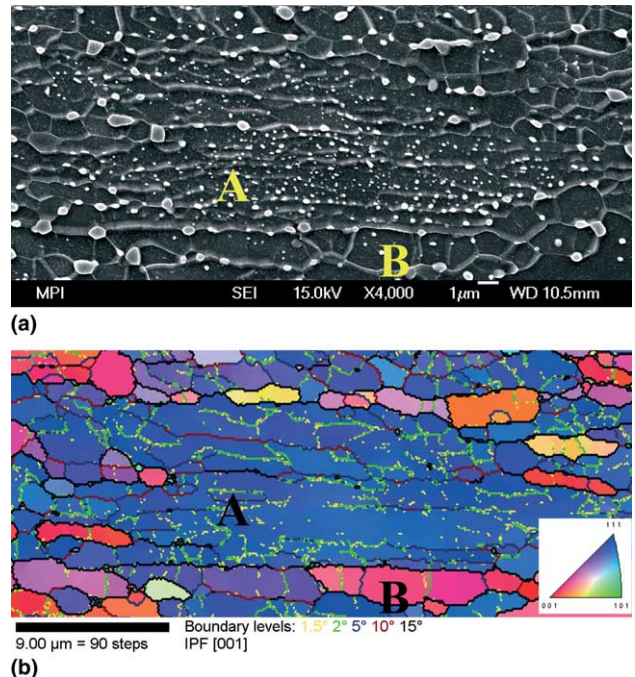


Fig. 10. Effect of cementite on ferrite softening process: (a) SEM and (b) EBSD image.

SEM and EBSD images of the same location in Fig. 10. It can be seen that in the area of fine cementite the formation of subgrains is not complete (cf. Fig. 10, area A). On the contrary, in the area of proeutectoid ferrite, the rearrangement of dislocations with the formation of low angle subgrain boundaries is in progress (cf. Fig. 10, area B).

This confirms that the limitation factor of ferrite softening can be the diffusion of carbon atoms. As shown in [15], for two-phase alloys the decomposition before recrystallization is controlled by the lower activation energy for diffusion of interstitial atoms (carbon) as compared to that which controls primary recrystallization (self-diffusion of iron atoms). The processes of spheroidization and distribution of cementite might be assumed to be decomposition, since they can be attributed to a local change of chemical composition, i.e., the change of carbon content in solid solution during lamellae dissolution, cementite re-precipitation, as well as dissolution of the fine particles with a coarsening of larger ones. Obviously, the formation and growth of ferrite subgrains are controlled by solute carbon and cementite particles, which grow by diffusion of carbon. The particle spacing determines the size of subgrains.

### 3.6. Effect of initial microstructure on cementite distribution and ferrite softening

As shown in Fig. 1, various cooling rates allow for obtaining various initial microstructures before the HWD. The effect of the cooling rate, i.e., the initial microstructure on the microstructure after HWD was studied.

The microstructures after HWD of steels with two different cooling rates and deformation/coiling temperatures 10 K/s, 943 K (670 °C) and 20 K/s, 973 K (700 °C) are shown in Fig. 11. In the case of low cooling rate (10 K/s), the microstructure after transformation is composed of proeutectoid ferrite and pearlite. With this initial microstructure, the HWD and subsequent simulated coiling (cf. Fig. 11(a)) results in a homogeneous distribution of cementite particles in a fine grained ferrite matrix, according to processes, shown and discussed earlier. According to the EBSD measurement, the ferrite contains about 65% high angle grain boundaries indicating advanced progress of continuous recrystallization. The increase of the cooling rate up to 20 K/s leads to a microstructure with proeutectoid ferrite, a finer pearlite and bainite, which results in areas with accentual finer cementite particles after HWD even at higher deformation/coiling temperature of 973 K (700 °C). These very fine cementite particles retard a subgrain formation in these areas (cf. Fig. 10). As a result the final microstructure is inhomogeneous and contains only 45% high angle ferrite grain boundaries (cf. Fig. 11(b)).

### 3.7. Coarsening of ferrite

The microstructure with fine ferrite (sub)grains that is stabilized due to homogeneously distributed cementite particles is fairly stable even after the deformation/coiling at high temperatures of ferritic range. But by some unfavorable circumstances some enlarged subgrains can abnormally grow.

Such a situation can occur in an inhomogeneous initial microstructure after a higher cooling rate near 20 K/s (cf. Fig. 11(b)). In this case, a local stored energy gradient may facilitate the preferential growth of one or several grains with high angle boundaries, as shown in Fig. 12. The grains in the areas of the former proeutectoid ferrite (cf. Fig. 10, area B), with coarser cementite particles, can be such potential fast growing grains. This abnormal grain growth is enhanced if the growing grain is surrounded by areas with essential higher stored energy, i.e., subgrains with low angle boundaries and partly deformed grains. The energy lowering due to the consumption of these areas by the growing coarse grain provides the driving force for this process.

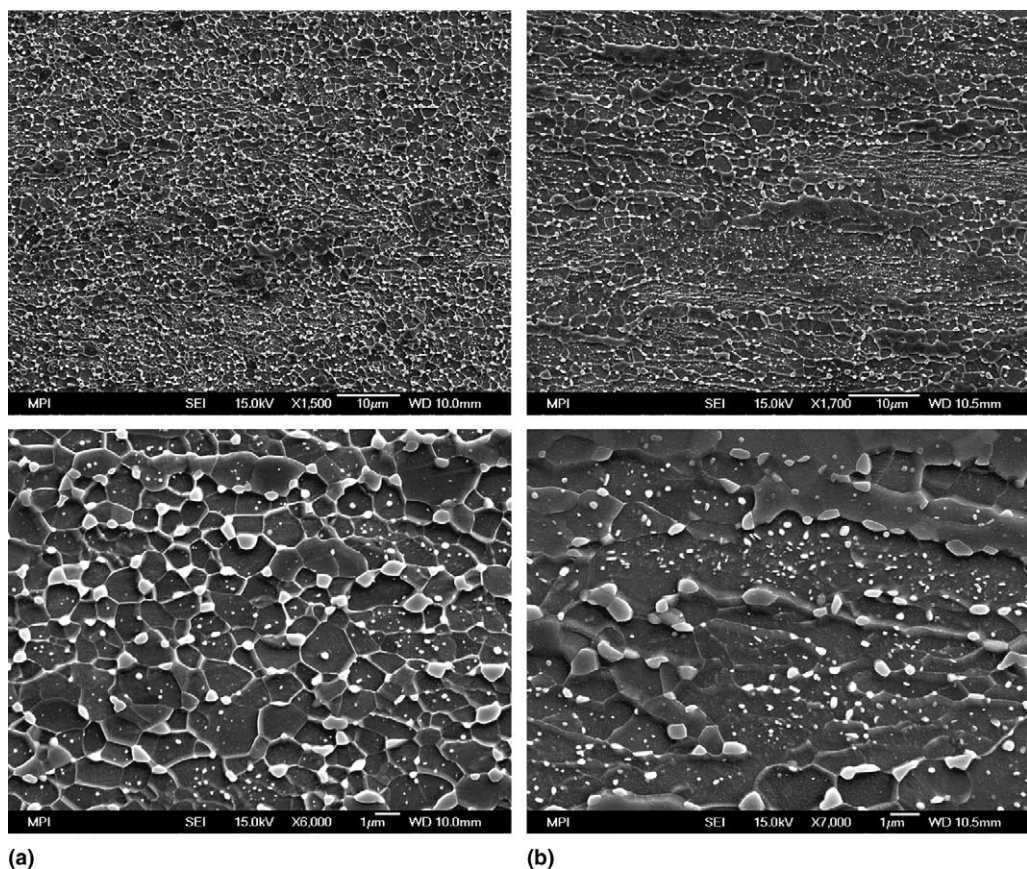


Fig. 11. Microstructure after the various cooling rates and deformation/coiling temperatures: (a) 10 K/s, 943 K (670 °C) and (b) 20 K/s, 973 K (700 °C).

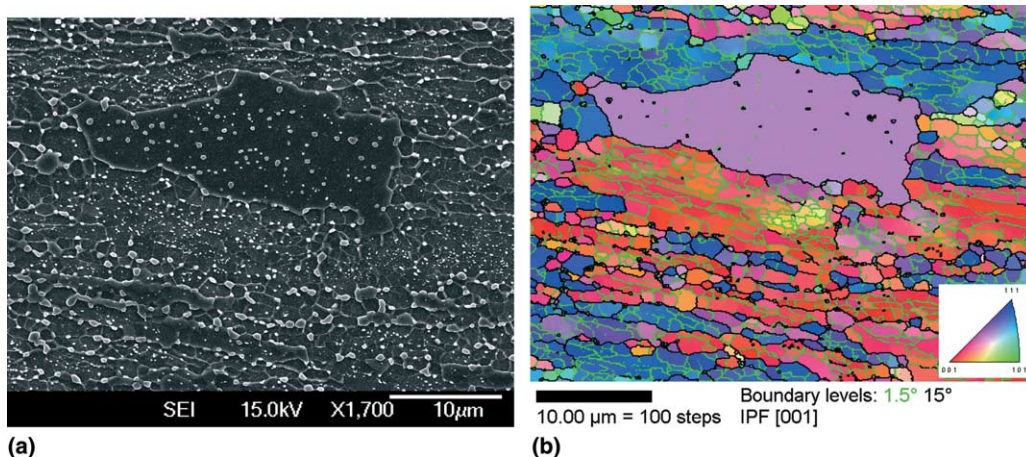


Fig. 12. Coarsening of ferrite: (a) SEM and (b) EBSD image.

#### 4. Conclusions

1. Spheroidization of pearlite during the HWD is accelerated by the formation of cementite lamellae kinks, fracture of lamellae and cementite subboundaries. Higher equilibrium carbon concentration in ferrite (higher carbon solubility) near these lamellae defects provokes a quick local dissolution of the lamella that leads to its division with a subsequent or simultaneous spheroidization.
2. A rather homogeneous distribution of cementite in an initially ferritic-pearlitic microstructure can be observed due to increase of deformation/coiling temperatures to 943–973 K (670–700 °C). This process is assumed to proceed by the local partial dissolution of former pearlite colonies due to a local increase of carbon solubility in ferrite. Simultaneously, the solute carbon may diffuse into the cementite-free proeutectoid ferrite areas with lower equilibrium carbon concentration and re-precipitate. Both of these processes are supported by a high density of lattice defects due to HWD.
3. Ferrite softening during the HWD can be attributed to a continuous or in situ recrystallization. Primary recrystallization is hardly probable because of the relatively low stored energy at rather high deformation temperatures as well as an increased amount of solute carbon in ferrite during the cementite spheroidization and fine cementite particles produced by spheroidization.
4. Continuous recrystallization contributes to high angle boundaries development due to accumulation of dislocations at the subgrain boundaries, by the subgrain growth with migration of low angle boundaries and by the merging of lower angle boundaries during subgrain coalescence.
5. According to the determination of activation energy of (sub)grain growth, the controlling factor of ferrite softening in the temperature range 903–963 K (630–

690 °C) is carbon diffusion during the spheroidization and redistribution of cementite.

6. The HWD of steel with initial ferrite-pearlite microstructure (after cooling rate 10 K/s) results in a homogeneous distribution of cementite in a fine grained ferrite matrix with about 65–70% high angle grain boundaries. On the contrary, the HWD of steel with initial ferrite-pearlite-bainite microstructure (after cooling rate 20 K/s) brings about an inhomogeneous cementite distribution with the areas of fine cementite particles and only 45% high angle ferrite grain boundaries.
7. In case of inhomogeneous microstructure (cooling rate 20 K/s), a high local gradient in the size of cementite particles tends to facilitate the preferential growth of some grains with mobile high angle boundaries, which leads to microstructure coarsening.

#### Acknowledgements

The authors express their gratitude to the financial support of the European Coal and Steel Community (ECSC).

#### References

- [1] Kaspar R, Kapellner W, Lang C. *Steel Res* 1988;59(11):492.
- [2] Robbins J, Shepard O, Sherby O. *J Iron Steel Inst* 1964;202(Oct.):804.
- [3] Pawelski O, Kaspar R. *Materialprüfung* 1988;30(11–12):357.
- [4] Chattopadhyay S, Sellars S. *Acta Met* 1982;30(1):157.
- [5] Watanabe T, Karashima S. *Physica Status Solidi* 1970;42:749.
- [6] Chalmers B. *Physical metallurgy*. New York: Wiley; 1959.
- [7] Novikov I. *Theory of heat treatment of metals*. Moscow: Metallurgia; 1986. p. 479.
- [8] Paqueton H, Pineau A. *JISI* 1971;209(12):991.
- [9] Babich V, Nesterenko A, Storojeva L. *Met Sci Heat Treat (USSR)* 1989;31(9–10):692.
- [10] Shin D, Park K, Kim Y. *Scripta Mater* 2003;48(5):469.

- [11] Hutchinson B, Bate P. In: Proceedings of the International Conference on Properties and Application of IF Steels. Tokyo: ISIJ; 2003. p. 337.
- [12] Quadir M, Duggan B. In: Proceedings of the International Conference on Properties and Application of IF Steels. Tokyo: ISIJ; 2003. p. 357.
- [13] Hales S, McNelley T, McQueen H. Metall Mater Trans A 1991;22A:1037.
- [14] Hornbogen E, Köster U. In: Haessner F, editor. Recrystallization of metallic materials. Berlin: Dr. Riederer Verlag; 1978. p. 159.
- [15] Hornbogen E. Metall Mater Trans A 1979;10A:947.
- [16] Nes E. In: Baudelet B, Surey M, editors. Superplasticité. Paris: Centre National de la Recherche Scientifique; 1985. p. 7.1.
- [17] Doherty R, Cahn R. J Less-Common Metals 1972;28:279.
- [18] Haessner F, editor. Recrystallization of metallic materials. Stuttgart: Dr. Riederer Verlag; 1978. p. 293.
- [19] Kristal M. Diffusion processes in iron alloys. Moscow; 1963. p. 278.
- [20] Holmes E, Winegard W. Acta Met 1959;7:411.
- [21] Drolet J, Galibois A. Acta Met 1968;16:1387.

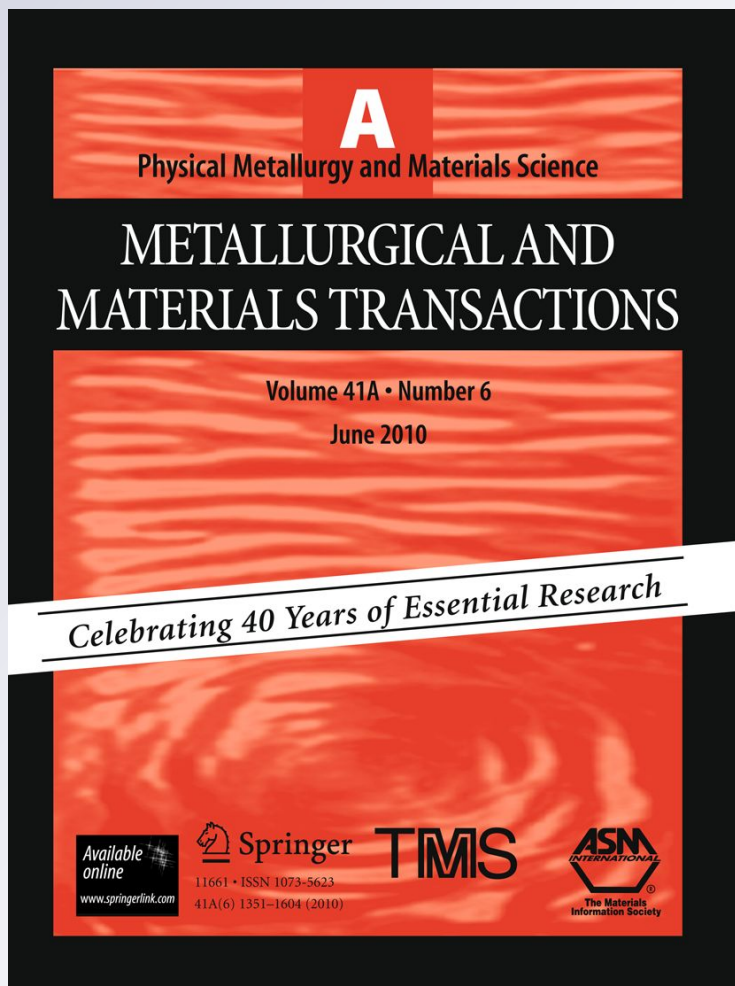
# *On the Effect of Manganese on Grain Size Stability and Hardenability in Ultrafine-Grained Ferrite/Martensite Dual-Phase Steels*

**Marion Calcagnotto, Dirk Ponge & Dierk Raabe**

**Metallurgical and Materials Transactions A**

ISSN 1073-5623  
Volume 43  
Number 1

Metall and Mat Trans A (2012) 43:37-46  
DOI 10.1007/s11661-011-0828-3



 Springer

**Your article is protected by copyright and all rights are held exclusively by The Minerals, Metals & Materials Society and ASM International. This e-offprint is for personal use only and shall not be self-archived in electronic repositories. If you wish to self-archive your work, please use the accepted author's version for posting to your own website or your institution's repository. You may further deposit the accepted author's version on a funder's repository at a funder's request, provided it is not made publicly available until 12 months after publication.**

# On the Effect of Manganese on Grain Size Stability and Hardenability in Ultrafine-Grained Ferrite/Martensite Dual-Phase Steels

MARION CALCAGNOTTO, DIRK PONGE, and DIERK RAABE

Two plain carbon steels with varying manganese content (0.87 wt pct and 1.63 wt pct) were refined to approximately 1  $\mu\text{m}$  by large strain warm deformation and subsequently subjected to intercritical annealing to produce an ultrafine grained ferrite/martensite dual-phase steel. The influence of the Mn content on microstructure evolution is studied by scanning electron microscopy (SEM). The Mn distribution in ferrite and martensite is analyzed by high-resolution electron backscatter diffraction (EBSD) combined with energy dispersive X-ray spectroscopy (EDX). The experimental findings are supported by the calculated phase diagrams, equilibrium phase compositions, and the estimated diffusion distances using Thermo-Calc (Thermo-Calc Software, McMurray, PA) and Dictra (Thermo-Calc Software). Mn substantially enhances the grain size stability during intercritical annealing and the ability of austenite to undergo martensitic phase transformation. The first observation is explained in terms of the alteration of the phase transformation temperatures and the grain boundary mobility, while the second is a result of the Mn enrichment in cementite during large strain warm deformation, which is inherited by the newly formed austenite and increases its hardenability. The latter is the main reason why the ultrafine-grained material exhibits a hardenability that is comparable with the hardenability of the coarse-grained reference material.

DOI: 10.1007/s11661-011-0828-3

© The Minerals, Metals & Materials Society and ASM International 2011

## I. INTRODUCTION

**FERRITE/martensite** dual-phase (DP) steels are used for automotive applications as they combine high strength with good formability and weldability.<sup>[1]</sup> To meet the demands of improved crush resistance and reduced fuel consumption, further strengthening of DP steels is necessary. Grain refinement of DP steels offers a promising strengthening method as, unlike in other metallic materials, the increase in yield strength and tensile strength is not accompanied by a loss in strain hardenability or uniform elongation.<sup>[2–6]</sup> A variety of processing routes exists to achieve grain sizes of 1  $\mu\text{m}$  and below.<sup>[7]</sup> Most studies focus on the production of ultrafine-grained (UFG) ferritic steels with finely dispersed cementite particles, whereas the number of studies on UFG DP steels is limited. Hence, a lack of systematic studies on the decisive parameters that control the microstructure evolution during the fabrication of UFG DP steels still exists. In particular, the effect of alloying elements on microstructure evolution has received little attention. Mukherjee *et al.*<sup>[8]</sup> studied

the effect of molybdenum and niobium additions on the grain refinement process during deformation-induced ferrite transformation. Son *et al.*<sup>[3]</sup> investigated the effect of microalloying with vanadium on the mechanical properties of UFG DP steels fabricated by equal channel angular pressing (ECAP) and intercritical annealing. In a previous paper,<sup>[9]</sup> we demonstrated that a certain manganese content is crucial to obtain an UFG ferrite/martensite microstructure. This was explained with the lower transformation temperatures in case of the high-Mn steel and with the Mn enrichment in cementite that is inherited by austenite and enhances its hardenability. However, a detailed analysis of the phenomena involved, including thermodynamic simulations, has not been given so far and is the subject of the current article.

Austenite formation from conventional ferrite/pearlite starting microstructures and the Mn partitioning involved during intercritical annealing were studied in the past.<sup>[10–16]</sup> Reaustenitization basically takes place in three stages<sup>[10]</sup>: (1) rapid dissolution of pearlite; (2) slower growth of austenite into ferrite, the growth rate being controlled by carbon diffusion in austenite at high temperatures [ $\sim 1123$  K ( $\sim 850$  °C)] and by manganese diffusion in ferrite at low temperatures [ $\sim 1023$  K ( $\sim 750$  °C)]; and (3) slow final equilibration of ferrite and austenite at a rate that is controlled by manganese diffusion in austenite. Important factors that influence the phase transformation kinetics are the cementite morphology,<sup>[11,13]</sup> the grain size,<sup>[14]</sup> the heating rate,<sup>[15]</sup>

---

MARION CALCAGNOTTO, Researcher, formerly with Max-Planck-Institut für Eisenforschung GmbH, 40237 Düsseldorf, Germany, is now with Salzgitter Mannesmann Forschung GmbH, 38239 Salzgitter, Germany. DIRK PONGE, Group Leader, and DIERK RAABE, Director, are with Max-Planck-Institut für Eisenforschung GmbH. Contact e-mail: d.ponge@mpie.de

Manuscript submitted September 27, 2010.

Article published online August 12, 2011

and the preceding thermomechanical treatment of the material.<sup>[11,15,17]</sup> However, the main part of the studies was performed on relatively coarse-grained (CG) materials that were produced by conventional hot and/or cold deformation, exhibiting a ferrite/lamellar pearlite starting microstructure.

The hardenability defines the material's ability to suppress reconstructive transformation at a given cooling rate. A high hardenability is generally desired to reduce the sensitivity to industrial processing conditions. Furthermore, it was shown repeatedly that intermediate cooling rates yield better combinations of strength and ductility compared with rapidly quenched DP steels,<sup>[18–20]</sup> mainly because of the reduction of the interstitial carbon content in ferrite.<sup>[18]</sup> However, a systematic investigation on the hardenability of an UFG DP steel has not been performed so far.

In this study, two plain carbon steels with different Mn content are subjected to hot deformation, large strain warm deformation, and subsequent intercritical annealing to examine the influence of Mn on the grain refinement process and on the microstructure evolution during intercritical annealing. Mn as an alloying element is of special interest because it was shown to be highly beneficial for grain refinement.<sup>[21]</sup> Furthermore, it increases the hardenability and decreases the Ar<sub>3</sub> temperature (nonequilibrium ferrite formation start temperature during cooling). However, too high Mn contents promote segregation and undesired banded microstructures. The effect of the nominal Mn concentration on Mn partitioning is investigated by using high-resolution electron backscatter diffraction (EBSD) analysis combined with energy-dispersive X-ray spectroscopy (EDX), as well as thermodynamic equilibrium calculations using Thermo-Calc (Thermo-Calc Software, McMurray, PA)<sup>[22]</sup> and Dicta (Thermo-Calc Software).<sup>[23]</sup> The hardenability of the steel with higher Mn content is assessed by determining the critical cooling rate that allows full austenite-to-martensite phase transformation and compared with the hardenability of a CG reference material.

## II. EXPERIMENTAL PROCEDURES

Two plain carbon manganese steels varying only in the Mn content (Table I) were produced by vacuum induction melting at the Max-Planck-Institut für Eisenforschung.

In this study, two different Mn contents were chosen to study the effect on microstructure evolution. For easy identification, the steel with lower Mn content will be called “15C steel” in the following, and the steel with higher Mn content “15CMn steel.”

Samples (50 mm × 40 mm × 60 mm) were taken directly from the cast ingot. Thermomechanical processing was realized by use of a 2.5 MN hot deformation simulator.<sup>[24,25]</sup> This computer-controlled servohydraulic press allows simulating industrial rolling schedules by user-defined heating, deformation, and cooling setups. The UFG ferrite/cementite starting microstructure was produced by the consecutive steps of austenitization and hot deformation, large strain warm deformation in a four-pass flat compression test series (total strain: 1.6), and warm annealing. Grain refinement to a ferrite grain size of approximately 1 μm is achieved during large strain warm deformation because of grain subdivision and pronounced recovery of ferrite, as well as continuous fragmentation and spheroidization of cementite.<sup>[26]</sup> The final ferrite/martensite dual-phase steel is produced by intercritical annealing slightly above the Ac<sub>1</sub> temperature (nonequilibrium austenite formation start temperature during heating) to form the desired amount of austenite, followed by quenching to transform the austenite into martensite. Intercritical annealing was performed in a Bähr Dil805 A/D (Bähr-Thermoanalyse GmbH, Hüllhorst, Germany) quenching and deformation dilatometer using cylindrical samples with a diameter of 4 mm and a gauge length of 10 mm. The center of these specimens corresponds to the position in the warm-deformed sample where the local strain equals the nominal strain.<sup>[27]</sup> A CG reference material from the same laboratory melt was produced by the same austenitization and hot deformation treatment, yet this was followed by air cooling to room temperature. This CG ferrite/pearlite microstructure was subjected to identical intercritical annealing conditions that were established for the UFG materials. In this way, similar martensite volume fractions and martensite carbon contents are achieved.<sup>[5,6]</sup>

Samples for scanning electron microscopy (SEM) and EBSD investigations were prepared by standard mechanical grinding and polishing procedures, finishing with 3 min polishing with colloidal silica. The phase fractions were determined based on three SEM micrographs taken at a 3000 times magnification in case of the UFG material and at a 500 times magnification in case of the CG material. The point counting method was applied to assess the volume fraction of the phases. Here, a grid of 150 points was superimposed on each micrograph. The number of points covering martensite or bainite divided by the total number of points defines the respective phase fraction.

EBSD experiments were conducted using a JEOL JSM 6500F (JEOL Ltd, Tokyo, Japan) high-resolution, high-intensity SEM equipped with field-emission gun. The small beam diameter and its high brightness yield high-contrast Kikuchi patterns with a high signal to

**Table I. Chemical Composition of the Steels Used, in wt pct**

Steel	C	Mn	Si	Al	N	S	P	Fe
15C	0.16	0.87	0.27	0.037	0.0024	0.0034	0.0021	balance
15CMn	0.17	1.63	0.28	0.036	0.0025	0.0038	0.0021	balance

noise ratio, therefore allowing high spatial and angular resolution. A high-speed DigiView charge-coupled device (CCD) camera of EDAX-TSL (EDAX/TSL, Draper, UT) was used for pattern acquisition. The step size was 50 nm, which is close to the resolution limit of the system. The data were recorded and analyzed using the EDAX-TSL OIM Analysis (EDAX Inc., Mahwah, NJ) software package. Martensite was indexed as a body-centred-cubic phase and is distinguished from ferrite by its lower image quality (IQ) and confidence index, which is a result of the higher crystal lattice imperfection. The Mn distribution in ferrite and martensite was investigated semiquantitatively by the use of EDX attached to the SEM.

### III. RESULTS

#### A. Determination of the Intercritical Annealing Temperatures

As it is known that Mn lowers the  $\alpha \rightarrow \gamma$  (ferrite to austenite) transformation start temperature, the intercritical annealing temperature for the 15C and the 15CMn alloys (Table II) must be different to obtain the same martensite fraction.

To define a suitable intercritical annealing temperature for both chemical compositions and to gain insight into the influence of the Mn content on phase transformation in the current materials, the phase diagrams were

calculated to determine the equilibrium temperatures, and dilatometer tests were performed to identify the phase transformation start and finish temperatures under experimental conditions.

The equilibrium phase diagrams and the respective phase transformation start and finish temperatures were calculated using Thermo-Calc,<sup>[21]</sup> version TCCR, database TCFE5 (Figure 1). Comparing the phase diagrams of the 15C steel (Figure 1(a)) and the 15CMn (Figure 1(b)), it is evident that Mn (as an austenite stabilizing alloying element) reduces the equilibrium austenite formation start ( $Ae_1$ ) and finish ( $Ae_3$ ) temperatures. The respective values are given in Table II.

The  $\alpha + \gamma + \text{cem}$  (ferrite + austenite + cementite) three-phase field is broadened with increasing Mn content. Therefore, cementite is replaced completely by austenite at 985 K (712 °C) in the 15C steel and at 969 K (696 °C) in the 15CMn steel. The equilibrium temperature at which the microstructure consists of 30 vol pct austenite and 70 vol pct ferrite is 1017 K (744 °C) in the 15C steel and 986 K (713 °C) in the 15CMn steel. As Mn reduces the carbon solubility in ferrite, the cementite fraction at room temperature is slightly higher in the 15CMn steel than in the 15C steel (2.37 pct compared with 2.5 pct). It has to be noted that the stoichiometric cementite phase ( $Fe_3C$ ) is replaced because of the addition of Mn by Fe-Mn carbides of various stoichiometries, e.g.,  $(Fe,Mn)_7C_3$ . Therefore, the general term “carbide” would be more appropriate to describe the current microstructure. However, the term

**Table II. Comparison of the Equilibrium and Experimental Phase Transformation Start and Finish Temperatures Obtained from the Phase Diagrams ( $Ae_1$  and  $Ae_3$ ) and the Dilatometer Tests ( $Ac_1$  and  $Ac_3$ )**

Steel	Equilibrium			Experimental	
	$Ae_1$ [K (°C)]	$Ae_3$ [K (°C)]	T [K (°C)] at 30 vol pct $\gamma$	$Ac_1$ [K (°C)]	$Ac_3$ [K (°C)]
15C	977 (704)	1109 (836)	1017 (744)	1006 (733)	1118 (845)
15CMn	952 (679)	1083 (810)	986 (713)	994 (721)	1108 (835)

$\gamma$ : Austenite.

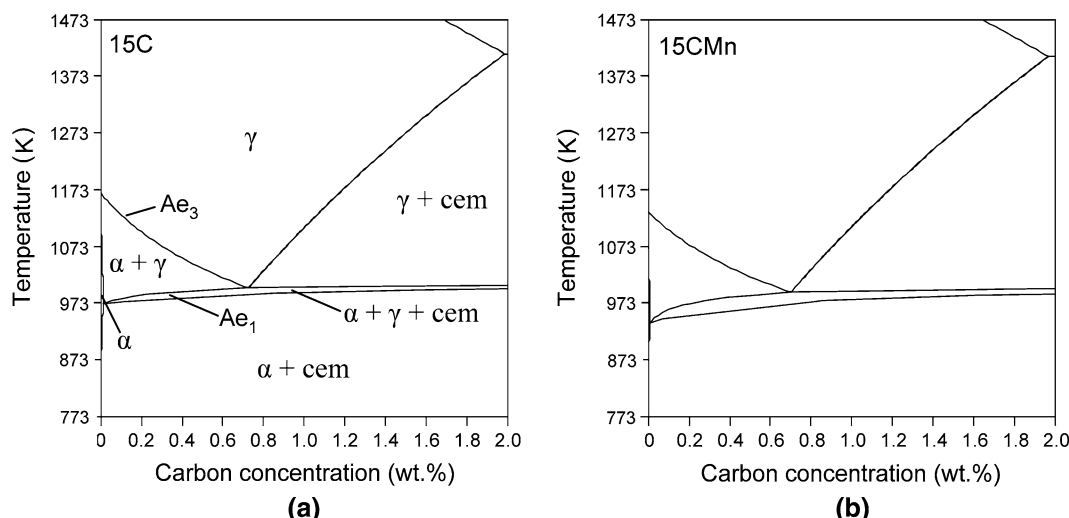


Fig. 1—Equilibrium phase diagrams for the 15C (a) and the 15CMn (b) steel. As an austenite stabilizing element, Mn lowers the phase transformation start ( $Ae_1$ ) and finish ( $Ae_3$ ) temperatures. Moreover, it broadens the ferrite + austenite + cementite ( $\alpha + \gamma + \text{cem}$ ) three-phase field.

"cementite" is used conventionally in the literature because the different carbides cannot be distinguished in micrographs. Therefore, the term "cementite" is used in this study. The equilibrium calculations using Thermo-Calc and Dictra<sup>[22]</sup> were performed using cementite as the only carbide phase to obtain results that can be compared directly with the microstructure.

To determine the intercritical annealing range under experimental conditions, several samples of both materials were heated at a rate of 1 K/s to 1173 K (900 °C), held for 2 minutes, and then cooled to room temperature. The  $Ac_1$  and  $Ac_3$  temperatures (nonequilibrium austenite formation start and finish temperatures during heating) were determined from the change in length vs temperature curves (Figure 2(a)). In the first stage, the sample length increases linearly with temperature as a result of thermal expansion. As the  $\alpha + \text{cem} \rightarrow \gamma$  phase transformation is accompanied by a volume decrease because of the closer packed face-centered cubic crystal lattice of austenite, the onset of phase transformation ( $Ac_1$ ) can be read from the curves as the first deviation from linearity. The transformation finish temperature ( $Ac_3$ ) is read from the point where linearity is reestablished. It is well known that the austenite formation takes place in two steps: (1) rapid dissolution of cementite in the  $\alpha + \gamma + \text{cem}$  three-phase field and (2) slower growth of austenite at the expense of ferrite in the  $\alpha + \gamma$  two-phase field. The transition from step (1) to step (2) is reflected in the curves by the change in slope between the  $Ac_1$  and  $Ac_3$  temperatures.

The results of several dilatometer tests are shown in Figure 2(b). For a comparison, the equilibrium  $Ae_1$  and  $Ae_3$  temperatures were calculated for a range of Mn contents using Thermo-Calc. It can be observed that the equilibrium and experimental values are in good agreement and that they show the same decreasing tendency with increasing Mn content. However, the mismatch between calculated and measured values is higher in the case of the 15CMn steel. A possible explanation for this discrepancy is that Mn decreases the carbon activity. As

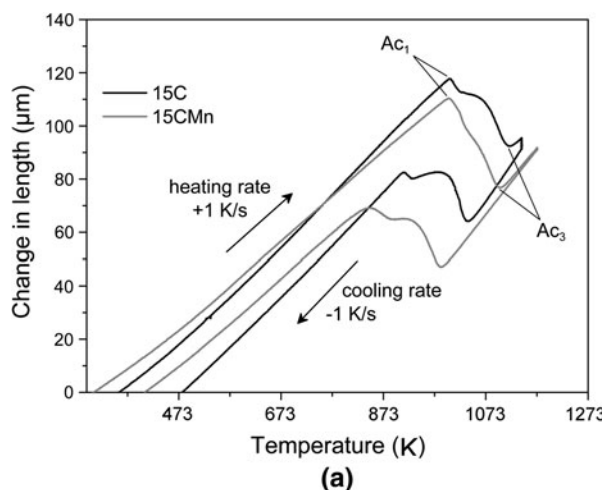
the phase transformation is controlled mainly by carbon diffusion, the reduced carbon activity retards the phase transformation. The mismatch is also higher for the  $Ac_1$  than for the  $Ac_3$  temperatures in both materials. The reason for the delay of the phase transformation onset is possibly that a certain overheating is necessary under nonequilibrium conditions to initiate austenite nucleation.

Based on these findings, the intercritical annealing temperature was set at 1023 K (750 °C) for the 15C steel and to 1003 K (730 °C) for the 15CMn steel. At these temperatures, a cementite-free microstructure containing 25–30 vol pct of austenite is expected.

### B. Microstructures Before and After Intercritical Annealing

Both steels were heated at a rate of 20 K/s to the intercritical annealing temperature [1023 K (750 °C) for the 15C and 1003 K (730 °C) for the 15CMn steel, respectively], held for 3 minutes, and quenched with hydrogen gas to room temperature at a cooling rate of –140 K/s. It was shown previously,<sup>[9]</sup> that the heating rate does not exert a considerable effect on microstructure evolution. Therefore, the faster heating applied in this party of the study is considered to be insignificant. Figure 3 shows the microstructures before and after intercritical annealing. In the left column, the UFG ferrite/cementite (F/C) steels fabricated by large strain warm deformation and annealing are presented, and the same samples after subsequent intercritical annealing are given in the right column.

The UFG-F/C microstructure is similar in both materials, yet in the 15C steel, the ferrite grain size is slightly larger and the cementite particles are somewhat larger and thus less numerous. It is obvious that during intercritical annealing, phase transformation has happened in both materials. However, the austenite in the 15C steel transformed into martensite only partially. The remaining austenite has undergone phase transfor-



(a)

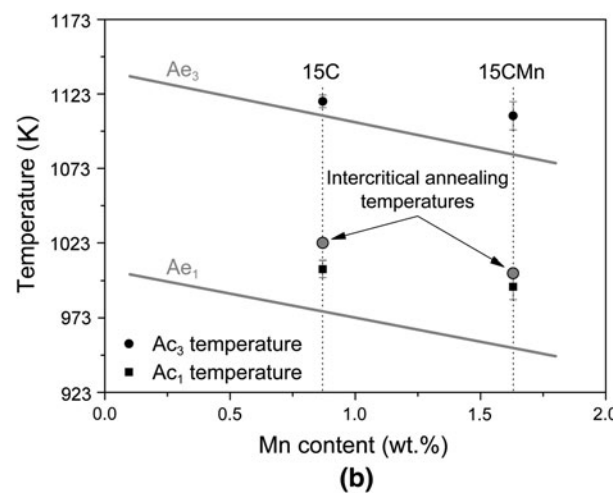


Fig. 2—Results of the dilatometer tests. (a) The phase transformation start ( $Ac_1$ ) and finish ( $Ac_3$ ) temperatures are read from the change in length versus temperature curves. (b) The results of several dilatometer tests are compared with the equilibrium temperatures ( $Ae_1$  and  $Ae_3$ ), and a suitable intercritical annealing temperature is defined.

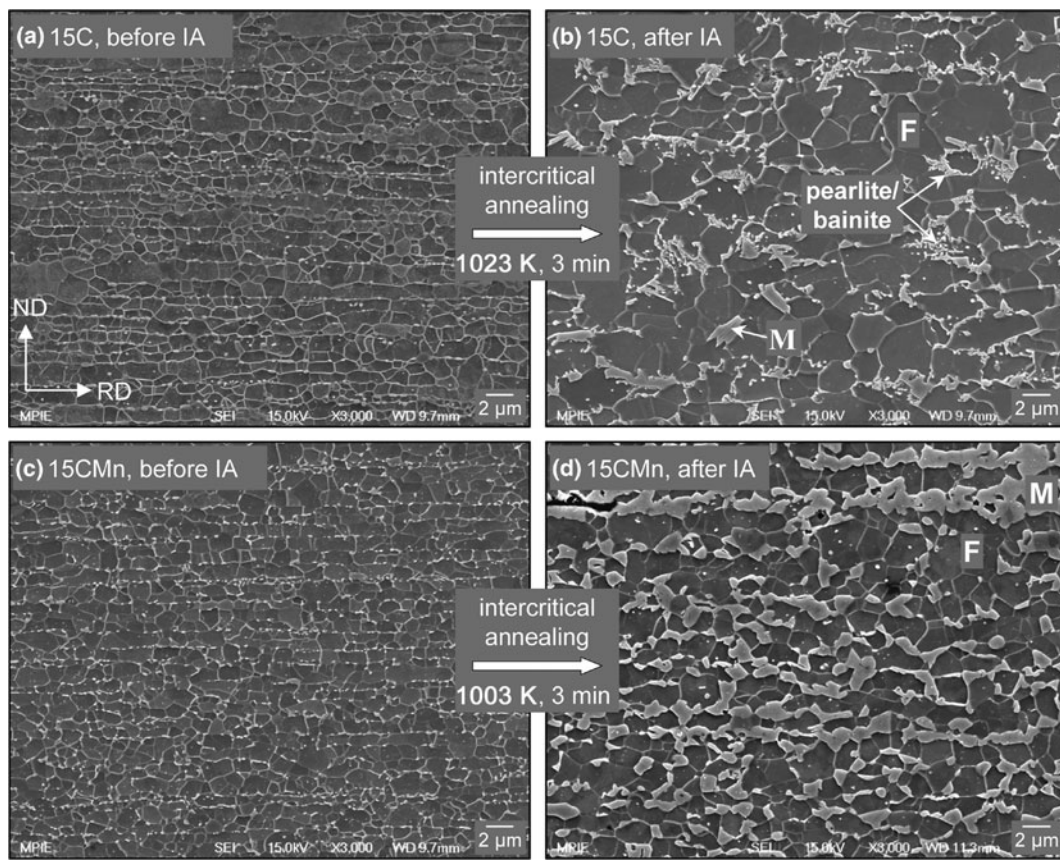


Fig. 3—Effects of chemical composition on microstructure evolution during intercritical annealing (IA) performed in a dilatometer. The ultra-fine-grained ferrite/cementite microstructure of the 15C steel (a) transforms into a fine-grained ferrite (F) matrix with martensite (M) and pearlitic/bainitic areas (b), whereas the 15CMn steel (c) exhibits the desired UFG ferrite/martensite dual-phase structure after intercritical annealing (d). Indication of rolling direction (RD) and normal direction (ND) counts for all images.

mation into bainite and/or pearlite. Furthermore, considerable grain growth has happened in the 15C steel.

In the 15CMn steel, the whole austenite has undergone displacive transformation into martensite, except minor amounts of retained austenite that are not detectable in the SEM images. The ferrite grain size (mean linear intercept length) was  $1.2 \mu\text{m}$  and the martensite volume fraction 24.3 pct. For more detailed quantification of the microstructure characteristics, the reader is referred to a paper recently submitted by our group.<sup>[28]</sup> Hence, the desired microstructure is only obtainable when a certain Mn content is added. As the only difference between the materials is the Mn content, the reason for the unlike microstructure evolution must be found in the Mn distribution.

### C. Mn Distribution Studied by EDX

The Mn partitioning between the phases can be visualized by high-resolution EBSD maps combined with EDX analysis. Figure 4 shows the grayscale IQ maps and the respective EDX maps of Mn of the 15C steel (Figure 4(a), micrograph in Figure 3(b)), and the 15CMn steel (Figure 4(b), micrograph in Figure 3(d)). Martensite is characterized by a lower IQ value because of the larger lattice distortions, thus appearing dark gray

in the IQ map. Retained austenite is marked in white on the IQ maps. One can observe that the martensite islands are subdivided into blocks. Retained austenite is isolated partly in the ferrite matrix and occurs partly within the martensite islands.

The EDX maps show the Mn distribution in a semiquantitative way. The scaling is normalized to 15 to 90 pct of the maximum Mn X-ray counts. For a more convenient comparison with the respective IQ map, the grain boundaries are superimposed. In the 15C steel, a slight enrichment in Mn is observed in some bainitic/martensitic areas (encircled). However, the overall distribution of Mn is homogeneous. In contrast, Mn segregation in the 15CMn steel (Figure 4(b)) parallel to the rolling direction is obvious. Martensite is situated mostly in the areas of high Mn concentration. In contrast, the ferrite matrix is depleted in Mn.

It is well known that the nucleation of austenite from ferrite/cementite structures starts at the interface between both phases.<sup>[10,29]</sup> Therefore, the Mn-enrichment in cementite is of particular importance for the intercritical annealing applied in this study. As one can observe from Figure 4(b), both martensite and retained austenite are enriched in Mn in comparison with the ferrite matrix. In particular, small martensite islands that are located along the rolling direction inherit the

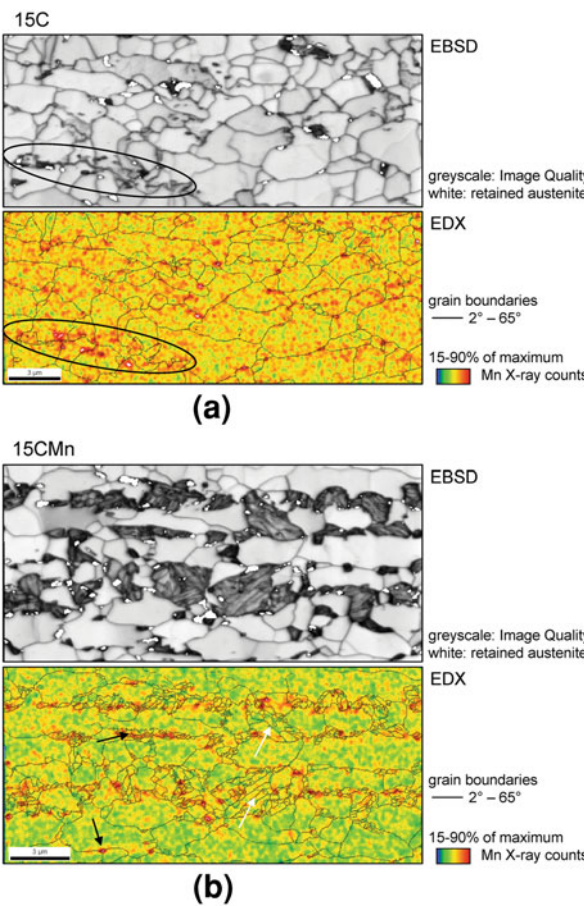


Fig. 4—High-resolution electron backscatter diffraction (EBSD) scans combined with energy dispersive X-ray spectroscopy (EDX) analysis of the 15C (a) and the 15CMn steel (b). The grayscale images show the Image Quality maps. The position of retained austenite is superimposed in white. The EDX maps are normalized for 15–19 pct of the maximum EDX counts for better visualization of the Mn distribution. Rolling direction is horizontal, and normal direction is vertical.

high Mn content from the cementite and the segregation pattern (black arrows). Some larger martensite islands do not show considerable Mn enrichment (white arrows).

#### D. Hardenability of the 15CMn Steel and its Coarse-Grained Counterpart

The hardenability of the 15CMn steel was assessed by applying different cooling rates after intercritical annealing and observation of the obtained microstructure to determine the minimum cooling rate that allows complete austenite-to-martensite phase transformation. As the 15C steel does not show full martensitic phase transformation even at the highest possible cooling rate, this part of the study was only performed with the 15CMn material. The samples were heated to 1003 K (730 °C), held for 1 minute, and then cooled at rates between –140 K/s and –10 K/s. After slow cooling, phase equilibrium is shifted to lower temperatures and consequently to lower austenite fractions with a higher carbon content. We found that slower cooling provides enough time for ferrite to grow into austenite after

cooling. Thus, the lower the cooling rate (*i.e.*, the longer the cooling time between intercritical annealing temperature and room temperature), the lower the martensite fraction and the larger the ferrite grain size. Slower cooling impedes martensite banding because of the epitaxial growth of ferrite. At a cooling rate of –20 K/s, minor parts of the UFG microstructure consist of bainite instead of martensite, so that this cooling rate is considered to be the critical cooling rate.

The same intercritical annealing conditions were applied to the CG counterpart having the same chemical composition and martensite volume fraction<sup>[5,6]</sup> in order to address the question to what extent the grain refinement process affects the hardenability of the steel. The bainite fraction was determined in order to assess the decreasing ability of the material to undergo reconstructive transformation with decreasing cooling rate. Bainite was determined manually on the basis of SEM micrographs. No differentiation was made between bainite and pearlite because of the similar morphology. Two micrographs of the materials cooled at –10 K/s are shown in Figure 5. Note the different magnifications of the images. One can observe that the main part of the UFG DP steel (Figure 5(a)) consists of martensite, whereas some austenite grains obviously decomposed into bainite (arrows). In contrast, the main fraction of the austenite for the CG material (Figure 5(b)) has undergone phase transformation into bainite and/or pearlite. Only small areas consist of martensite (arrows).

The bainite fraction as a function of grain size and cooling rate is shown in Figure 6. Additionally, the bainite fraction divided by the total second phase fraction (bainite + martensite) is illustrated. On the x axis, the cooling time between the intercritical annealing temperature and 773 K (500 °C) is shown, as this is the decisive parameter for displacive transformation. At the shortest cooling time (cooling rate –140 K/s), all austenite is transformed into martensite. Bainite formation is detectable in both materials at a cooling rate of –50 K/s, yet the volume fraction is low (~1 vol pct). Further decreasing the cooling rate leads to a substantial increase in bainite fraction in both materials. However, the rate of increase is much higher in the CG material than in the UFG material. For example, at a cooling rate of –15 K/s, the UFG material consists of 8.2 vol pct bainite, whereas the CG material contains 19.3 vol pct bainite. At this point, bainite makes up 42 pct of the total second phase fraction in the UFG DP steel, and even 77 pct in the CG counterpart. At even lower cooling rates, the bainite fraction in the UFG steel tends to stabilize, whereas it is increased to 24 vol pct in the CG material.

## IV. DISCUSSION

### A. Effect of Mn on Grain Size Stability

When comparing the microstructure after intercritical annealing of the 15C steel (0.87 wt pct Mn) with the 15CMn steel (1.63 wt pct Mn) in Figure 3, the importance of a critical amount of Mn to suppress grain

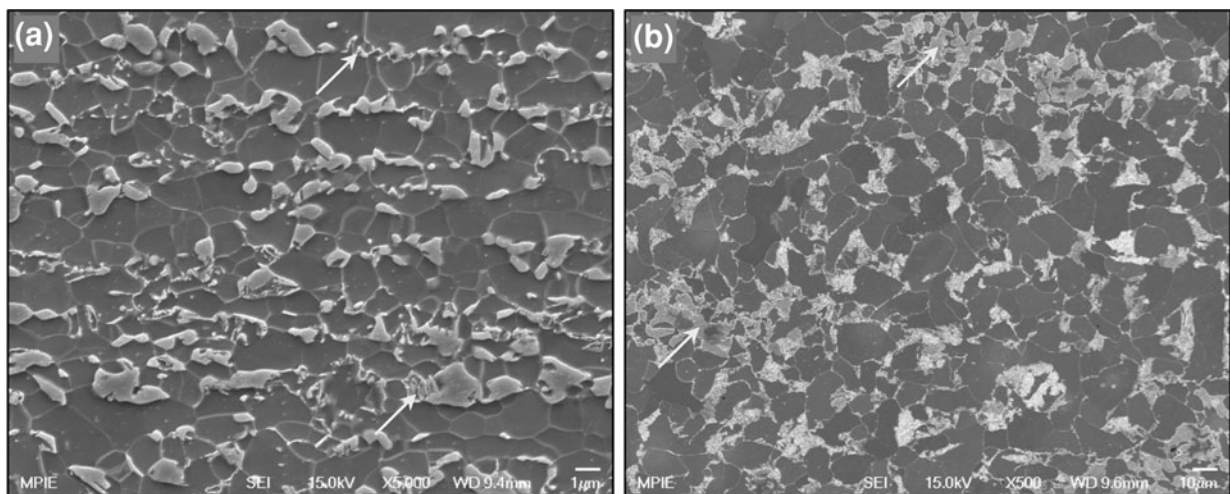


Fig. 5—Typical micrographs of the ultrafine-grained (*a*) and the coarse-grained (*b*) dual-phase steels (composition 15CMn), which were subjected to intercritical annealing at 1003 K (730 °C) for 1 min, followed by cooling at a rate of -10 K/s. Note the different magnification in the two images. Rolling direction is horizontal, and the normal direction is vertical.

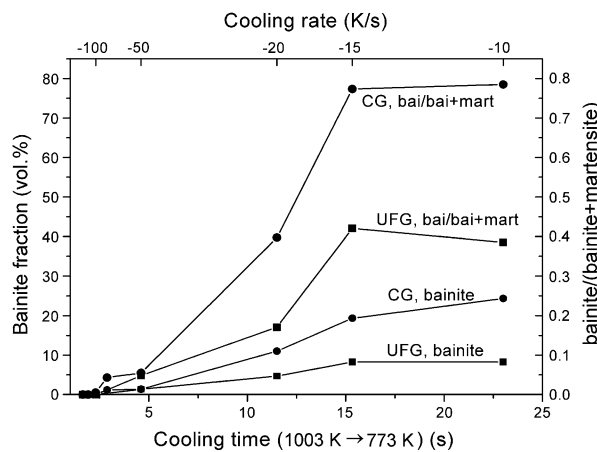


Fig. 6—Influence of cooling rate on bainite (and/or pearlite) fraction showing the higher hardenability of the ultrafine-grained (UFG) material compared with the coarse-grained (CG) counterpart.

growth is obvious. Mn contributes to the grain size stability of the UFG material in several ways.

The most beneficial effect of Mn is that it decreases the  $A_{c1}$  temperature. Therefore, it is possible to achieve the same amount of austenite at lower temperatures. For example, the equilibrium intercritical annealing temperature to achieve 30 vol pct austenite is 1017 K (744 °C) in the 15C steel (Figure 7) but only 986 K (713 °C) in the 15CMn steel. In the experiment, the intercritical annealing temperature in the 15C steel was 1023 K (750 °C), whereas it was 1003 K (730 °C) in the 15CMn steel. Annealing at lower temperatures means slower kinetics of grain growth.

The second effect of Mn is that it broadens the  $\alpha + \gamma + \text{cem}$  three-phase field (Figure 1). Therefore, most of the phase transformation in the 15CMn steel occurs within the three-phase field. This can be best visualized by plotting the equilibrium phase fractions as a function of temperature (Figure 7). To achieve an austenite volume fraction of 30 pct, a greater temperature

increase after complete dissolution of cementite is necessary in the 15C steel than in the 15CMn steel. It is known that grain growth is inhibited strongly in the three-phase field because of the coexistence of cementite and austenite. Therefore, grain growth is suppressed longer in the 15CMn steel than in the 15C steel. Although equilibrium conditions are not achieved under the current experimental conditions, it is likely that the longer intercritical annealing above the three-phase field contributes to grain growth in the 15C steel.

Third, the addition of Mn leads to a finer distribution of cementite in the initial microstructure (Figure 3). Song *et al.*<sup>[21]</sup> explain this effect by the enrichment of Mn in cementite that occurs during large strain warm deformation and warm annealing because of the introduction of dislocations, vacancies, and high-angle grain boundaries during dynamic and static recovery. Cementite is then replaced by Mn-Fe carbides that are characterized by a higher stability.<sup>[30]</sup> The higher stability of the Fe-Mn carbides makes them more resistant to Ostwald ripening and therefore leads to a finer distribution of these particles. Hence, the greater number of cementite particles in the 15CMn steel exerts a more effective pinning effect on the grain boundaries, therefore suppressing grain growth. The efficiency of boundary pinning during intercritical annealing by spheroidized cementite has been demonstrated by Garcia and DeArdo<sup>[11]</sup> on the basis of a low alloy steel containing different carbon contents. The authors studied the austenite formation from spheroidized cementite in a ferrite matrix and found that extensive grain growth during intercritical annealing occurs only in case of the lowest carbon content.

Furthermore, Mn in solid solution exerts a solute drag effect and thus reduces the grain boundary mobility.<sup>[31]</sup>

### B. Effect of Mn on Hardenability

Primarily, hardenability is a function of the carbon content in austenite. However, Mn was found to also

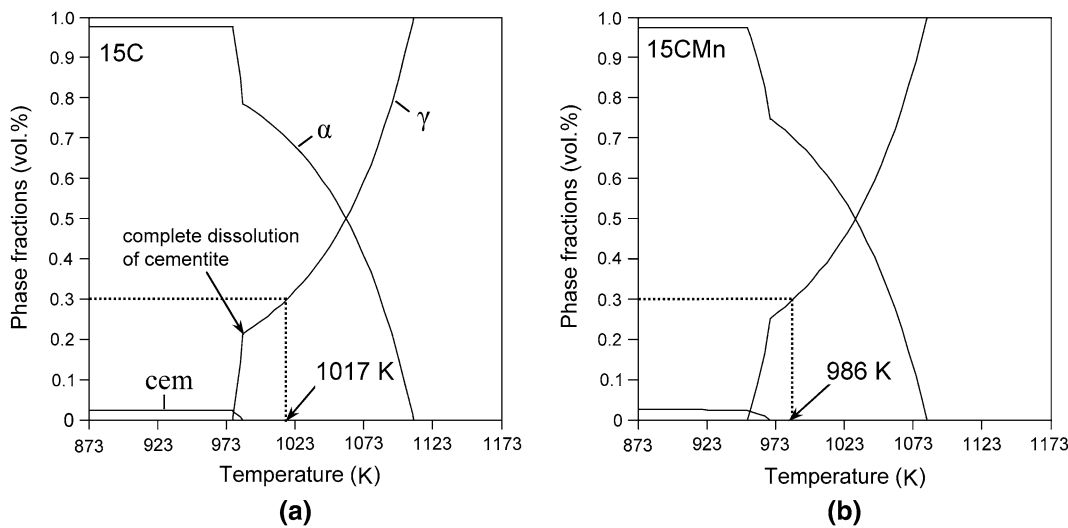


Fig. 7—Equilibrium phase volume fractions as a function of temperature in the 15C (a) and in the 15CMn steel (b):  $\alpha$ : ferrite,  $\gamma$ : austenite, cem: cementite.

increase hardenability substantially.<sup>[32]</sup> Being an austenite-stabilizing element, Mn partitions preferentially to austenite and increases its hardenability, *i.e.*, it retards proeutectoid ferrite, pearlite, and bainite formation. Moreover, Mn increases the carbon solubility in austenite, which enhances its hardenability. Hence, Mn lowers the critical cooling rate for martensite formation. For this reason, the low hardenability of the 15C is surprising. Even the fastest quench at  $-140\text{ K/s}$  was not enough to transform all austenite into martensite, although the Mn content (0.87 wt pct) is not marginal. Hence, it is anticipated that not only the nominal Mn content of the material is decisive to allow a good hardenability but also the processing route. It was shown that the Mn enrichment in cementite, which takes place during large-strain warm deformation and warm annealing,<sup>[21]</sup> is inherited by the newly formed austenite during intercritical annealing and in the following by the martensite (Figure 4). This is enabled by the low diffusion coefficient of Mn in austenite. The diffusion coefficient  $D$  of Mn in austenite at 1003 K ( $730^\circ\text{C}$ ) was estimated using Dictra, applying the mobility database v.2.<sup>[22]</sup> It is  $4.2 \times 10^{-19}\text{ m}^2\text{s}^{-1}$ , which is close to the values reported by Atkinson *et al.*<sup>[12]</sup> and by Speich *et al.*<sup>[10]</sup>, who studied similar temperatures and compositions. The diffusion distance  $l$  can be estimated from conventional random walk kinetics as

$$l = 2 \cdot \sqrt{D \cdot t_{IA}} \quad [1]$$

Hence, within the intercritical annealing time  $t_{IA}$  of 1 minute, the diffusion distance of Mn in austenite is  $0.01\text{ }\mu\text{m}$ . This explains the observation in Figure 4, that large martensite islands are not fully enriched in Mn. Mn is preserved in the location of the former cementite particle and austenite growth is controlled by the diffusion of carbon which is commonly expected at 1003 K ( $730^\circ\text{C}$ ).<sup>[29]</sup> It is followed that the Mn enrichment in the austenite islands controls the hardenability

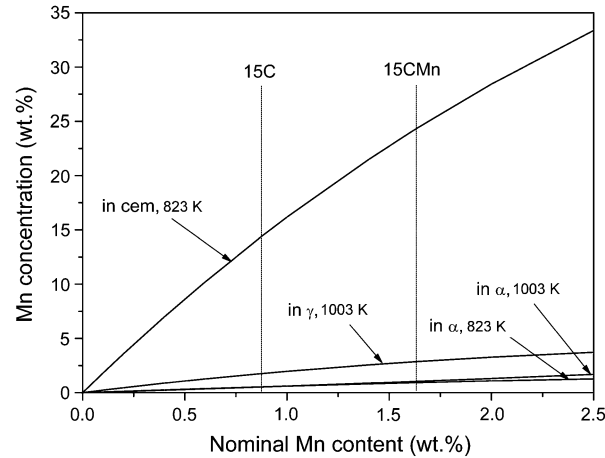


Fig. 8—Equilibrium Mn enrichment in cementite (cem), austenite ( $\gamma$ ), and ferrite ( $\alpha$ ) as a function of nominal Mn content revealing the drastic increase in Mn enrichment in cementite by increasing the Mn content from 0.87 to 1.63 wt pct.

of the material. In both the 15C and the 15CMn steel, Mn enrichment takes place during large strain warm deformation. Yet, Mn enrichment is more pronounced in the 15CMn steel as is revealed by the combined EBSD and EDX maps. Hence, the lower nominal Mn content in the 15C does not yield enough Mn enrichment in cementite so as to increase the hardenability of the newly formed austenite successively.

Examining the equilibrium values of Mn in cementite helps to clarify this observation. In Figure 8, the Mn content in cementite, ferrite, and austenite is plotted as a function of the nominal Mn concentration in the material. Increasing the Mn content from 0.87 wt pct (15C) to 1.63 wt pct (15CMn) increases the equilibrium Mn concentration in cementite from 14 pct to 24 pct at the deformation temperature [823 K ( $550^\circ\text{C}$ )]. In contrast, the Mn concentration in ferrite is much lower and

does not change remarkably with increasing nominal Mn concentration. Although full equilibrium is not reached during processing, the remarkable increase of Mn content in cementite as a result of a higher nominal Mn concentration was shown experimentally.<sup>[21]</sup> At the intercritical annealing temperature of 1003 K (730 °C), the equilibrium values in austenite are naturally much lower than in cementite. As the austenite fraction at 1003 K (730 °C) is much higher than the cementite fraction at 823 K (550 °C), Mn is diluted. However, the dilution is not accomplished within the short intercritical annealing time given due to the low diffusion coefficient of Mn (see preceding text). Therefore, one can conclude that the higher hardenability of the 15CMn steel is a consequence of the Mn enrichment in cementite during large-strain warm deformation. The lower nominal Mn content in the 15C steel does not result in Mn partitioning that is high enough to ensure a Mn content of the reversed austenite that allows full martensitic transformation.

### C. Effect of Grain Refinement on Hardenability

The hardenability of the 15CMn steel is considerable not only with respect to the absence of additional alloying elements like Mo or Cr but also with respect to its small grain size. In general, a CG microstructure exhibits a higher hardenability than a fine-grained microstructure. This is because austenite decomposition starts at grain boundaries. Therefore, the lower grain boundary fraction in coarser microstructures delays austenite decomposition because of the reduction of potential pearlite or bainite nucleation sites. However, the critical cooling rate of the CG (ferrite grain size 12.4  $\mu\text{m}$ ) and the UFG steel (ferrite grain size 1.2  $\mu\text{m}$ ) were found to be nearly identical (between -50 K/s and -20 K/s, Figure 6). As the nominal Mn content is the same in the materials, it must be the processing route that determines the hardenability. The CG material has undergone a one-pass hot rolling step, which is performed above the  $\text{Ar}_3$  temperature and thus does not lead to Mn enrichment in pearlite. In contrast, warm deformation to produce the UFG microstructure is applied below  $\text{Ac}_1$  temperature and leads to considerable Mn enrichment in cementite. Therefore, it is concluded that the detrimental effect of the high-grain-boundary density is balanced by the beneficial effect of a higher Mn content in cementite that is inherited by austenite, giving rise to a comparable critical cooling rate in the CG and the UFG material.

It was found that with decreasing cooling rate the bainite fraction increases at a much higher rate in the CG material than in the UFG material. That means, the ability to undergo martensitic transformation is maintained more successfully in the UFG material at slower cooling. At slow cooling, ferrite grows at the expense of austenite, thereby rejecting carbon into austenite. This process is facilitated when diffusion distances are short. Therefore, carbon enrichment in the austenite during slow cooling is much more effective in the UFG steel, thus leading to a higher hardenability of the remaining

austenite. This explains that even at the lowest tested cooling rate of -10 K/s only approximately 40 pct of the total second phase fraction is made up of bainite in the UFG material, whereas bainite constitutes around 78 pct of the second phase fraction in the CG steel.

## V. CONCLUSIONS

Two UFG plain C-Mn steels varying only in the Mn content (15C: 0.87 wt pct Mn, 15CMn: 1.63 wt pct Mn) were subjected to intercritical annealing to study the differences in the microstructure evolution. The hardenability of the 15CMn steel was determined and compared to its CG counterpart. The main conclusions are as follows:

1. A certain Mn content is necessary to avoid grain growth during intercritical annealing and to ensure sufficient hardenability to transform all austenite into martensite upon cooling.
2. Mn enhances the grain size stability by (1) lowering the  $\text{Ac}_1$  temperature and thus, the intercritical annealing temperature; (2) broadening the  $\alpha + \gamma + \text{cem}$  three-phase field in which grain growth is inhibited; (3) refining cementite, which causes a more efficient pinning effect; and (4) reducing the grain boundary mobility by solute drag.
3. The hardenability is controlled by Mn partitioning between ferrite and cementite, which is established during large strain warm deformation. The high Mn concentration in cementite is preserved in austenite and increases its hardenability.
4. The hardenability of the UFG DP steel (15CMn) is comparable to its CG counterpart in terms of the critical cooling rate (-20 K/s to -50 K/s). The detrimental effect of a high grain boundary fraction is compensated for by the higher Mn concentration in austenite in the UFG steel.
5. The ability to accomplish the martensitic phase transformation at decreasing cooling rates is higher in the UFG material than in the CG material because of the more effective carbon enrichment in austenite during cooling.

## REFERENCES

1. K.P. Imlau and T. Heller: *Steel Res. Int.*, 2007, vol. 78, pp. 180–84.
2. Z.H. Jiang, Z.Z. Guan, and J.S. Lian: *Mater. Sci. Eng. A*, 1995, vol. 190, pp. 55–64.
3. Y.I. Son, Y.K. Lee, K.T. Park, C.S. Lee, and D.H. Shin: *Acta Mater.*, 2005, vol. 53, pp. 3125–34.
4. M. Delincé, Y. Brechet, J.D. Embury, M.G.D. Geers, P.J. Jacques, and T. Pardoen: *Acta Mater.*, 2007, vol. 55, pp. 2337–50.
5. M. Calcagnotto, D. Ponge, and D. Raabe: *Mater. Sci. Eng. A*, 2010, vol. 527, pp. 7832–40.
6. M. Calcagnotto, Y. Adachi, D. Ponge, and D. Raabe: *Acta Mater.*, 2010, vol. 59, pp. 2738–46.
7. R. Song, D. Ponge, D. Raabe, J.G. Speer, and D.K. Matlock: *Mater. Sci. Eng. A*, 2006, vol. 441, pp. 1–17.
8. K. Mukherjee, S.S. Hazra, and M. Militzer: *Metall. Mater. Trans. A*, 2009, vol. 40A, pp. 2145–59.
9. M. Calcagnotto, D. Ponge, and D. Raabe: *ISIJ Int.*, 2008, vol. 48, pp. 1096–1101.

10. G.R. Speich, V.A. Demarest, and R.L. Miller: *Metall. Trans. A*, 1981, vol. 12A, pp. 1419–28.
11. C.I. Garcia and A.J. DeArdo: *Metall. Trans. A*, 1981, vol. 12A, pp. 521–30.
12. C. Atkinson, T. Akbay, and R.C. Reed: *Acta Metall. Mater.*, 1995, vol. 43, pp. 2013–31.
13. D.V. Shtansky, K. Nakai, and Y. Ohmori: *Z. Metallkd.*, 1999, vol. 90, pp. 25–37.
14. S.J. Sun and M. Pugh: *Mater. Sci. Eng. A*, 2000, vol. 276, pp. 167–74.
15. J. Huang, W.J. Poole, and M. Militzer: *Metall. Mater. Trans. A*, 2004, vol. 35A, pp. 3363–75.
16. N. Maruyama, T. Ogawa, and M. Takahashi: *Mater. Sci. Forum*, 2007, vols. 558–9, pp. 247–52.
17. Y.I. Son, Y.K. Lee, and K.T. Park: *Metall. Mater. Trans. A*, 2006, vol. 37A, pp. 3161–64.
18. S. Hayami, T. Furukawa, H. Gondoh, and H. Takechi: *Formable HSLA and Dual-Phase Steels*, Ed. A.D. Davenport, TMS, New York, NY, 1979, pp. 167–80.
19. D.K. Matlock, G. Krauss, L.F. Ramos, and G.S. Luppi: *Structure and Properties of Dual-Phase Steels*, Eds. R.A. Kot and J.W. Morris, TMS, New York, NY, 1979, pp. 62–90.
20. S.S. Hansen and R.R. Pradhan: *Fundamentals of Dual-Phase Steels*, Eds. R.A. Kot and B.L. Bramfitt, TMS, New York, NY, 1981, pp. 113–44.
21. R. Song, D. Ponge, and D. Raabe: *ISIJ Int.*, 2005, vol. 45, pp. 1721–26.
22. B. Jansson, M. Schalin, M. Selleby, and B. Sundman: *Computer Software in Chemical and Extractive Metallurgy*, Eds. C.W. Bale and G.A. Irons, The Metallurgical Society of CIM, Quebec, Canada, 1993, pp. 57–71.
23. A. Borgenstam, A. Engstrom, L. Hoglund, and J. Agren: *J. Phase Equil.*, 2000, vol. 21, pp. 269–80.
24. O. Pawelski and R. Kaspar: *Materialprüfung*, 1988, vol. 30, pp. 357–60.
25. R. Kaspar and O. Pawelski: *Materialprüfung*, 1989, vol. 31, pp. 14–16.
26. R. Song, D. Ponge, D. Raabe, and R. Kaspar: *Acta Mater.*, 2005, vol. 53, pp. 845–58.
27. J.S. Distl, A. Streißelberger, R. Kaspar, and U. Zeislmaier: *Materialprüfung*, 1985, vol. 27, pp. 131–35.
28. M. Calcagnotto, D. Ponge, and D. Raabe: *ISIJ Int.*, 2011, In press.
29. M. Hillert, K. Nilsson, and L.E. Torndahl: *J. Iron Steel Inst.*, 1971, vol. 209, pp. 49–66.
30. Y.C. Zhang and D.M. Schleich: *J. Solid State Chem.*, 1994, vol. 110, pp. 270–73.
31. D.A. Porter, K.E. Easterling, and M.Y. Sherif: *Phase Transformations in Metals and Alloys*, CRC Press, Boca Raton, FL, 2009.
32. R.A. Grange: *Metall. Trans.*, 1973, vol. 4, pp. 2231–44.